NMR studies of formulation stability and liquid-liquid phase separation in biopharmaceuticals

A Thesis submitted to The University of Manchester for the
degree of Doctor of Philosophy
in the Faculty of Science and Engineering

2021

Jack E. Bramham

Department of Chemistry
School of Natural Sciences

Table of Contents

1 General Introduction 18

1.1 Antibody biopharmaceuticals 18

1.1.1 Small molecule pharmaceuticals versus biopharmaceuticals 18

1.1.2 Antibody structure and function 19

1.1.3 Monoclonal antibody biopharmaceuticals 21

1.1.4 Production and administration of antibody biopharmaceuticals 23

1.2 Antibody biopharmaceutical stability 25

1.2.1 Chemical stability 26

1.2.2 Physical instability 27

1.2.3 Aggregation 27

1.2.4 Fragmentation 28

1.3 Self-association and liquid-liquid phase separation 29

1.3.1 Reversible self-association and viscosity 29

1.3.2 The phenomenon of liquid-liquid phase separation 31

1.3.3 Opalescence 32

1.3.4 LLPS in antibody biopharmaceuticals 33

1.3.5 Extended phase behaviour of proteins 34

1.3.6 LLPS in biology 35

1.3.7 Current approaches to study self-association and protein phase separation… 36

1.4 Nuclear magnetic resonance spectroscopy 36

1.4.1 Introduction to protein NMR spectroscopy 37

1.4.2 Application of NMR spectroscopy to biopharmaceuticals 38

1.4.3 Application of NMR spectroscopy to study protein phase separation 40

1.5 NMR techniques used in this Thesis 41

1.5.1 Longitudinal and transverse relaxation 41

1.5.2 Dark-state Exchange Saturation Transfer (DEST) 42
1.5.3 Translational diffusion 44
1.5.4 Spatially-selective NMR 45
1.6 Introduction to the Thesis 47
1.6.1 Aims and structure of this Thesis 47
2 Comprehensive assessment of protein and excipient stability in biopharmaceutical formulations using ^{1}H NMR spectroscopy 49
2.1 Abstract 50
2.2 Introduction 50
2.3 Materials and Methods 52
2.3.1 Sample preparation 52
2.3.2 NMR spectroscopy 53
2.3.3 High Performance Size Exclusion Chromatography 54
2.4 Results 54
2.4.1 Initial NMR characterisation of formulation content 54
2.4.2 Changes in Ab 1D ^{1}H NMR spectra upon accelerated stability storage 56
2.4.3 Changes in protein apparent relaxation rates during accelerated stability storage… 58
2.4.4 Protein degradation detected by high-performance size exclusion chromatography analysis 60
2.4.5 Small molecule degradation detected by T_2 filtered ^{1}H NMR 61
2.5 Discussion 63
2.6 Conclusion 65
2.7 Acknowledgments 65
2.8 Supplementary Information 66
3 Stability of a high-concentration monoclonal antibody solution produced by liquid-liquid phase separation 69
3.1 Abstract 70

3.2 Introduction ... 70
3.3 Materials and Methods ... 72
3.3.1 Sample preparation ... 72
3.3.2 NMR spectroscopy ... 73
3.3.3 High-performance size exclusion chromatography ... 74
3.3.4 Viscosity measurements ... 74
3.4 Results ... 75
3.4.1 Using LLPS to concentrate mAb solutions ... 75
3.4.2 Production of model high-concentration formulations from the dense fraction ... 76
3.4.3 Arg·Glu improves the stability of model formulations derived from the dense fraction ... 77
3.5 Discussion ... 80
3.6 Acknowledgments ... 82
4 ^{19}F Dark-state Exchange Saturation Transfer NMR reveals reversible formation of protein-specific large clusters in high-concentration protein mixtures ... 83
4.1 Abstract ... 84
4.2 Introduction ... 84
4.3 Materials and Methods ... 86
4.3.1 ^{19}F Labelling ... 86
4.3.2 NMR experimental details ... 87
4.3.3 DEST data fitting and protein cluster size analysis ... 87
4.4 Results ... 89
4.4.1 Characterisation of dark states in ^{19}F-tagged mAb mixtures ... 89
4.4.2 Effects of temperature and concentration on apparent radius of mAbs ... 92
4.4.3 Effects of additives – excipients, salt and denaturant ... 94
4.5 Discussion ... 96

4.6 Conclusions 97

4.7 Acknowledgments 97

4.8 Supporting Information 99

5 Temporal and spatial characterisation of protein liquid-liquid phase separation using NMR spectroscopy 104

5.1 Abstract 105

5.2 Introduction 105

5.3 Materials and Methods 107

5.3.1 Sample preparation 107

5.3.2 NMR spectroscopy 107

5.3.3 Spatially-selective NMR 108

5.3.4 ^{19}F Dark-state Exchange Saturation Transfer (DEST) 109

5.3.5 Relaxation 109

5.3.6 Translational diffusion 110

5.4 Results 110

5.4.1 TFE signal is sensitive to local protein concentration 110

5.4.2 TFE behaviour in isolated dense and lean fractions 112

5.4.3 Tracking fast kinetics of LLPS through bulk-detection NMR 114

5.4.4 Tracking slower kinetics of layer separation by bulk-detection and spatially-selective NMR 119

5.5 Discussion 121

5.6 Conclusion 124

5.7 Acknowledgements 124

5.8 Supporting Information 126

6 Characterisation of liquid-liquid phase separation in an antibody biopharmaceutical by ^{19}F NMR spectroscopy 130

6.1 Abstract 131

6.2 Introduction 131

6.3 Materials and Methods 132
6.3.1 Sample preparation 132
6.3.2 NMR spectroscopy 133
6.3.3 Relaxation and diffusion 134
6.4 Results 134
6.4.1 TFE is sensitive to local mAb concentration 134
6.4.2 TFE behaviour in isolated lean and dense fractions 135
6.4.3 Kinetics of COE-13 LLPS 137
6.5 Discussion 141
6.6 Conclusion 142
6.7 Acknowledgements 142
6.8 Supporting Information 143
7 General conclusions and future outlook 144
8 References 148

WORD COUNT: 47519

List of Figures

Figure 1-1. Structure of antibody monomers, chains and fragments 19
Figure 1-2. Examples of innovative engineered antibodies and related proteins 22
Figure 1-3. Schematic of the process of liquid-liquid phase separation 31
Figure 1-4. Model phase diagrams for phase separating protein solutions. 32
Figure 1-5. Illustration of the relationship between molecular size, and T_1 and T_2 relaxation 42
Figure 1-6. Detection of NMR invisible dark states by DEST 43
Figure 1-7. Spatially-selective NMR. 46
Figure 2-1. Initial NMR spectra and apparent relaxation rates of the three Abs recorded at 40°C 55
Figure 2-2. Changes in ^{1}H NMR spectra during accelerated stability storage at 40°C over time 57
Figure 2-3. Changes in ^{1}H R_2 during accelerated stability storage 59
Figure 2-4. Changes in ^{1}H R_1 during accelerated stability storage 60
Figure 2-5. Assessment of monomer, aggregate and fragment content by HPSEC 61
Figure 2-6. Degradation of sucrose detected by ^{1}H NMR spectroscopy. 62
Figure 2-7. Arginine degradation and solution pH changes detected by ^{1}H NMR spectroscopy 63
Figure 3-1. LLPS of COE-13 triggered by incubation at 4°C 75
Figure 3-2. NMR comparison of mAb structure and colloidal behaviour before and after LLPS 76
Figure 3-3. Phase behaviour of the model formulations after 24 hours incubation at 4 or 40°C 78
Figure 3-4. Monomer loss, aggregation and fragmentation of model formulations following storage at 4 or 40°C 78
Figure 3-5. Viscosity of the model high-concentration formulations across a range of temperatures after 28 days storage at either 4 or 40°C 80
Figure 4-1. Example of DEST profiles for mAb2-TFBPD in an equimolar mixture with COE-19-TFCS (total concentration 160 mg/mL) 90
Figure 4-2. Temperature dependence of observed effective transverse relaxation rate (R_2^{obs}) 91

Figure 4-3. DEST data for all four mAb-tag combinations for temperatures from 277K to 313K........92
Figure 4-4. The temperature dependence of effective mAb radii........93
Figure 4-5. The calculated effective concentrations of dark state clusters........94
Figure 5-1. Effect of protein concentration on TFE probe and TFT reference NMR signal parameters........112
Figure 5-2. Analysis of the bulk-detected NMR spectra of isolated lean and dense fractions as a function of temperature........113
Figure 5-3. Detection and quantification of TFE in an NMR dark-state at 20°C........114
Figure 5-4. Examples of bulk-detected ^{19}F NMR spectra of TFE in BSA undergoing microscopic LLPS at different temperatures following a temperature jump.........116
Figure 5-5. Fast kinetics of BSA LLPS at different temperatures as characterised by bulk-detected NMR.........118
Figure 5-6. Kinetics of LLPS and layer separation of BSA at 40°C characterised by bulk-detection NMR........120
Figure 5-7. Slow kinetics of BSA LLPS at 40°C as characterised by spatially-selective NMR........120
Figure 5-8. Schematic of types of BSA phase separation observed at different temperatures by bulk-detection and spatially-selective NMR........123
Figure 6-1. Effect of increasing mAb concentration on TFE ^{19}F NMR signal........135
Figure 6-2. Behaviour of the isolated dense and lean fractions as a function of temperature........136
Figure 6-3. Behaviour of the TFT external reference following temperature jumps.........137
Figure 6-4. Examples of bulk-detected ^{19}F NMR spectra of TFE in COE-13 during the initial process of phase separation........139
Figure 6-5. Kinetics of COE-13 phase separation as determined by bulk-detection NMR........140

List of Supplementary Figures

Figure S2-1. T_2-filtered NMR spectra of the three Ab formulations at T=0, highlighting the presence of the small molecule components 66
Figure S2-2. Modelling of the effects of aggregation and fragmentation, in isolation and together, on 1D ^{1}H NMR signal intensity 67
Figure S2-3. HPSEC chromatograms of the three Abs over 12 weeks accelerated stability storage 68
Figure S4-1. Examples of intensity decay curves from a combined pair of R_2 relaxation experiments. 99
Figure S4-2. Bloch-McConnell matrix used for modelling the DEST effect for exchange between NMR-visible species A and the dark state B 100
Figure S4-3. Further examples of DEST models fitted to observed data 101
Figure S4-4. Rate constant data for two mAbs at different temperatures 101
Figure S4-5. Overlays of the 1D ^{19}F NMR spectra for the four mAb-Tag combinations at 277K (in blue) and 313K (in red). 102
Figure S4-6. Raw diffusion coefficients (D_L) for both mAbs tagged with TFCS 103
Figure S4-7. DEST model, with fixed P^{vis} = 0.99999 (i.e. no dark state population) simulated for experimental data of an equimolar sample of mAb2-TFCS and COE-19-TFBPD completely denatured with 6 M GdnHCl 103
Figure S5-1. Schematic of NMR tube and NMR detection volumes 126
Figure S5-2. Effect of slice centre position on spatially-selective NMR signal integrals… 126
Figure S5-3. Appearance of phase-separated BSA solutions after incubation at 40°C and 50°C. 127
Figure S5-4. Examples of spectral deconvolution of the TFE ^{19}F NMR signal following LLPS at 45°C. 127
Figure S5-5. Time dependence of deconvoluted TFE signal parameters from BSA LLPS at different temperatures 128
Figure S5-6. Determination of boundary position and sedimentation rate by spatially-selective NMR 129
Figure S6-1. Calibration curve for temperature determination from TFT external reference chemical shift 143

List of Tables

Table 3-1. Volumes and protein concentrations of the various solutions obtained during LLPS experiments....73
Table 3-2. Rates of degradation (± standard errors) for the model formulations stored at 40°C....79
Table 4-1. The effects of additives on dark state clusters of COE-19 and mAb2 observed at 277K....95

Abbreviations

Abs	Antibodies
LLPS	Liquid-liquid phase separation
ADC	Antibody drug conjugate
ADCC	Antibody-dependent cellular cytotoxicity
AFM	Atomic force microscopy
Arg·Glu	Arginine·Glutamate
AUC	Analytical ultracentrifugation
B_{22}	Osmotic second virial coefficient
BBSRC	Biotechnology and Biological Sciences Research Council
BSA	Bovine serum albumin
BsAb	Bispecific antibody
CASE	Collaborative awards in science and engineering
CDC	Complement-dependent cytotoxicity
CDR	Complementarity determining region
CGE	Capillary gel electrophoresis
CPMG	Carr-Purcell-Meiboom-Gill
CW	Continuous wave
DEST	Dark-state exchange saturation transfer
D_L	Translational diffusion coefficient
DLS	Dynamic light scattering
DOSY	Diffusion ordered spectroscopy
DTP	Doctoral Training Partnership
E. coli	*Escherichia coli*
EM	Exponential multiplication
Fab	Fragment antigen-binding
Fc	Fragment crystallisable
FRAP	Fluorescence recovery after photobleaching
HPSEC	High-performance size exclusion chromatography
HSA	Human serum albumin
HSQC	Heteronuclear single quantum coherence
IDP	Intrinsically disordered proteins
Ig	Immunoglobulin

IV	Intravenous
k_D	Diffusion interaction parameter
LCST	Lower critical solution temperature
LMWO	Lower molecular weight oligomer
mAb	Monoclonal antibody
MRI	Magnetic resonance imaging
MWCO	Molecular weight cut-off
nD	n-dimensional
NMR	Nuclear magnetic resonance
NOE	Nuclear Overhauser effect
PEG	Polyethylene glycol
pI	Isoelectric point
ppm	Parts per million
R_1	Longitudinal relaxation rate
R_2	Transverse relaxation rate
Rh	Hydrodynamic radius
RNP	Ribonucleoprotein
scFV	Single chain variable fragment
SLS	Static light scattering
STD	Saturation transfer difference
T_1	Longitudinal relaxation time
T_2	Transverse relaxation time
τ_c	Rotational correlation time
TFBPD	1-(4-(trifluoromethyl)benzyl)-1H-pyrrole-2,5-dione
TFCS	ε-trifluoroacetylcaproyloxy)succinimide ester
TFE	Trifluoroethanol
TFT	Trifluorotoluene
UCST	Upper critical solution temperature
Water-LOGSY	Water-ligand observed via gradient spectroscopy

Abstract

Biopharmaceuticals, including antibodies (Abs), are the fastest growing segment of the pharmaceutical industry, and offer unique treatment possibilities for a range of diseases, including neurodegenerative and immune diseases, and cancers. Abs are currently typically administered by expensive and time consuming intravenous injection in a clinical setting, and there is growing interest in faster administration by subcutaneous injection, potentially by the patient themselves at home. However, subcutaneous injection volumes are typically limited to < 2 mL, requiring the development of high-concentration protein formulations (> 100 mg/mL). Such high concentrations promote physical instabilities, such as reversible self-association, irreversible aggregation, and liquid-liquid phase separation (LLPS). Characterising these instabilities by conventional biophysical techniques is challenging, particularly *in situ* at high concentration.

In this Thesis, we demonstrate the use of NMR spectroscopy to study the stability and phase separation of Abs and other model proteins. In the first half of the Thesis, we show that ^{1}H NMR spectroscopy can detect the degradation of both the protein and small molecule components of Ab formulations *in situ* without sample manipulation. Additionally, we employ a typical formulation approach, namely the addition of an excipient (Arg·Glu) to the phase separated dense fraction, to show that LLPS is suitable as an alternative method to concentrate Ab solutions. In the second half of the Thesis, we detail the development of two new ^{19}F NMR approaches to study protein self-association and LLPS. We show that ^{19}F Dark-state Exchange Saturation Transfer (DEST) NMR can be used to detect the self-association and clustering of ^{19}F tagged Abs in otherwise NMR invisible dark states. Finally, we demonstrate a novel experimental approach, with a fluorinated probe molecule combined with spatially-selective and conventional bulk-detection NMR, to study the kinetics of phase separation. We first develop this approach in a model system (bovine serum albumin), before applying it to a biopharmaceutical Ab. In conclusion, we have developed a number of NMR approaches to study Abs and phase separation. These approaches may encourage the use of NMR spectroscopy in the biopharmaceutical industry.

Declaration

No portion of the work referred to in the Thesis has been submitted in support of an application for another degree or qualification of this or any other university or other institute of learning.

Copyright statement

i. The author of this Thesis (including any appendices and/or schedules to this Thesis) owns certain copyright or related rights in it (the “Copyright”) and she has given The University of Manchester certain rights to use such Copyright, including for administrative purposes.

ii. Copies of this Thesis, either in full or in extracts and whether in hard or electronic copy, may be made only in accordance with the Copyright, Designs and Patents Act 1988 (as amended) and regulations issued under it or, where appropriate, in accordance with licensing agreements which the University has from time to time. This page must form part of any such copies made.

iii. The ownership of certain Copyright, patents, designs, trademarks and other intellectual property (the “Intellectual Property”) and any reproductions of copyright works in the Thesis, for example graphs and tables (“Reproductions”), which may be described in this Thesis, may not be owned by the author and may be owned by third parties. Such Intellectual Property and Reproductions cannot and must not be made available for use without the prior written permission of the owner(s) of the relevant Intellectual Property and/or Reproductions.

iv. Further information on the conditions under which disclosure, publication and commercialisation of this Thesis, the Copyright and any Intellectual Property and/or Reproductions described in it may take place is available in the University IP Policy (see http://documents.manchester.ac.uk/DocuInfo.aspx?DocID=24420), in any relevant Thesis restriction declarations deposited in the University Library, The University Library’s regulations (see http://www.library.manchester.ac.uk/about/regulations/) and in The University’s policy on Presentation of Theses.

Acknowledgements

Completing a PhD is a meandering journey of highs and lows, and I would like to take this opportunity to thank the people who have helped me navigate through, and allowed me to look back on the time with fondness.

Firstly, I am extremely grateful to my supervisor Alexander ‘Sasha’ Golovanov, particularly for his balanced approach of quiet enthusiasm and support for my unconventional ideas, contrasted with “Devil’s advocate” questioning to keep my work on track. I’d also like to thank the other members of the Golovanov group; John Edwards, Richard Tunnicliffe and Matja Zalar for assistance and valuable scientific discussions.

Next, I’d like to thank my industrial supervisors Adrian Podmore and Stephanie Davies for their support and guidance from an industrial perspective. Thanks also to the entire Formulation team at AstraZeneca Granta Park for making me welcome during my placement visits.

At the Manchester Institute of Biotechnology, thanks go to Matthew Cliff for managing the NMR facility and for answering my obscure NMR questions. Thanks also to the building’s technical staff, particularly Rehana Sung. I’m also grateful to the protein aggregation groups of Jim Warwicker, Robin Curtis and Richard Henchman for opportunities to present my work and for useful questions. A massive thanks also to our lunch group, particularly Aisling Roche, Jas Kalayan, Nicole Sibanda, and Nikita Vekeria, for always providing a welcome break from science and a crossword to look forward to.

Finally, I’d like to thank my family, particularly my mum, without whom even starting a PhD would not have been possible. Lastly, a massive thanks to Matja for her unwavering support and love, and for making me smile every day, even when all my coaxial inserts have glued themselves inside my NMR tubes.

Alternative format for submission and authorship details

This Thesis in presented in a journal format, with individual chapters presented in the form of separate research papers. The contributions of individual authors to each chapter is detailed below.

Authors in alphabetical order

S.M.B. – Steven M. Bishop, J.E.B. – Jack E. Bramham, S.A.D. – Stephanie A. Davies, J.M.E. – John M. Edwards, A.P.G. – Alexander P. Golovanov, A.P. – Adrian Podmore, and C.v.d.W. – Christopher van der Walle,

Chapter 2: Comprehensive assessment of protein and excipient stability in biopharmaceutical formulations using ^{1}H NMR spectroscopy

J.E.B. performed experiments, analysed the data, and drafted the manuscript. A.P. and S.A.D. supplied Abs and provided guidance and supervision from an industrial perspective. A.P.G. conceived and supervised the project and provided input regarding data analysis.

Chapter 3: Stability of a high-concentration monoclonal antibody formulation produced by liquid-liquid phase separation

J.E.B. performed experiments, analysed the data, and drafted the manuscript. A.P. and S.A.D. supplied Abs and provided guidance and supervision from an industrial perspective. A.P.G. conceived and supervised the project and provided input regarding data analysis.

Chapter 4: ^{19}F Dark-state Exchange Saturation Transfer NMR reveals reversible formation of protein-specific large clusters in high-concentration protein mixtures

J.M.E. and J.E.B. contributed equally. J.M.E. prepared samples, performed experiments, analysed the data, and drafted the manuscript. J.E.B. performed experimental set-up, created data analysis scripts, analysed the data, and drafted the manuscript. A.P., S.M.B. and C.v.d.W. supplied Abs and provided guidance and supervision from an industrial perspective. A.P.G. conceived and supervised the project and provided input regarding data analysis.

Chapter 5: Temporal and spatial characterisation of protein liquid-liquid phase separation using NMR spectroscopy

J.E.B. performed experiments, analysed the data, and drafted the manuscript. A.P.G. conceived and supervised the project and provided input regarding data analysis. The manuscript was written through contributions of all authors.

Chapter 6: Characterisation of phase and layer separation in antibody biopharmaceuticals by ^{19}F NMR spectroscopy

J.E.B. performed experiments, analysed the data, and drafted the manuscript. A.P. and S.A.D. supplied Abs and provided guidance and supervision from an industrial perspective. A.P.G. conceived and supervised the project and provided input regarding data analysis.

Additional publications arising from PhD studies

Priscilla Kheddo, Jack E. Bramham, Rebecca J. Dearman, Shahid Uddin, Christopher F. van der Walle, & Alexander P. Golovanov. Investigating liquid-liquid phase separation of a monoclonal antibody using solution-state NMR spectroscopy: Effect of Arg·Glu and Arg·HCl. *Mol. Pharmaceutics* **2017** 14(8):2852-2860.

Jack E. Bramham & Alexander P. Golovanov. How can NMR spectroscopy help protein biopharmaceutical development? *European Pharmaceutical Review* **2020** 1.

1 General Introduction

1.1 Antibody biopharmaceuticals

Pharmaceutical drugs have helped to revolutionise human health, enabling people to live longer and healthier lives. Historically, most pharmaceuticals have been small molecule drugs, but over the last four decades, biopharmaceuticals, a new class of drugs, have risen in prominence.

1.1.1 Small molecule pharmaceuticals versus biopharmaceuticals

Small molecule drugs are pharmaceutical products with low molecular weight, typically less than 1 kDa, produced by chemical synthesis reactions or purified from a natural source [1]. Conversely, biopharmaceuticals are typically of higher molecular weight, and are produced in, or extracted from biological or biotechnological sources [2]. Following the first biopharmaceutical, humanised insulin expressed in *Escherichia Coli* (*E. coli*) [3], around 285 distinct biopharmaceuticals have been approved [4], with biopharmaceutical sales as a percentage of total pharmaceutical sales continuing to grow [5]. Biopharmaceuticals include; protein products, such as small peptides (< 10 kDa or < 100 amino acids), globular proteins, engineered protein scaffolds, hormones, and antibodies and antibody-related proteins; nucleic acid or gene-based products; and whole cell products [4].

The emergence of biopharmaceuticals can be ascribed to a number of perceived advantages over small molecule drugs [6, 7]. Firstly, biopharmaceuticals typically have higher affinity and efficacy for their target than small molecules, meaning they are associated with fewer unwanted off-target effects. Secondly, antibody biopharmaceuticals, in particular, are significantly more stable than small molecules, with longer serum half-lives enabling less frequent dosing strategies. Additionally, when biopharmaceuticals are degraded, they are recycled into common biological compounds, such as amino acids, sugars, and nucleic acids, or excreted; whereas small molecules may have toxic degradation products or be inherently toxic (e.g. some chemotherapies) [8]. Despite these advantages, small molecules still have potential advantages in a number of areas, including possibility of oral administration [9], ease of manufacturing, and the ability to cross membrane barriers, particularly the blood-brain barrier [10].

This Thesis will focus on antibodies and antibody-related biopharmaceuticals as they are the largest class of biopharmaceuticals and currently represent over 65% of all biopharmaceutical sales [4].

1.1.2 Antibody structure and function

Antibodies, also known as immunoglobulins (Igs), are large glycoproteins (typically 150-200 kDa), which play an important role in the vertebrate immune system [11]. In mammals, Igs in membrane-bound or secreted forms are produced by B cells, a type of white blood cell also known as B lymphocytes. Antibodies bind specific target molecules (antigens) in order to neutralise targets displaying these antigens. This can occur through action of the antibody itself (neutralisation) [12], through recruitment of phagocytic cells to destroy targets by phagocytosis (agglutination or precipitation), through recruitment of natural killer cells to destroy target cells by lysis (antibody-dependent cellular cytotoxicity (ADCC)), or through activation of the immune complement system (complement-dependent cytotoxicity (CDC)) [13].

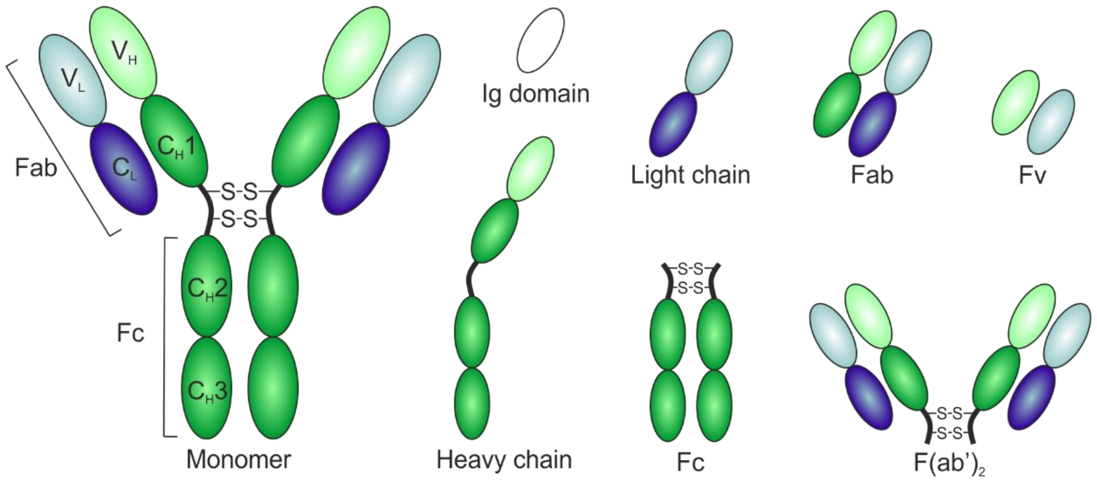

Figure 1-1. Structure of antibody monomers, chains and fragments. Light and heavy chains are coloured blue and green, respectively. Constant domains are darker colours, while variable domains are lighter colours.

Ig monomers consist of two identical heavy chains and two identical light chains, arranged in a Y-shaped quaternary structure (Figure 1-1). The heavy chain contains three constant domains (C_H1, C_H2, and C_H3), a variable domain (V_H), and a hinge region, which renders some flexibility to the Ig Y-shape. Conversely, the light chain consists of a single constant (C_L) and a single variable (V_L) domain. The constant domains are identical in all antibodies of a given type, while the variable domains differ between antibodies of the same type. All domains have the same immunoglobulin fold of the Ig superfamily, with two layers of β-sheets, containing β-strands arranged in an antiparallel manner. These chains and regions are linked by a series of disulphide bonds, which are increasingly recognised to occur in classical and non-classical manners, and vary between antibody isotypes [14].

The Y-shaped antibody structure can also be classified into a number of regions. The 'arms' of the Y-shape form the two fragment antigen-binding (Fab) regions, each consisting of constant domains C_H1 and C_L, and variable domains V_H and V_L. Within the Fab, the variable domains V_H and V_L, also known as the fragment variable (Fv), and specifically, three loops, the complementarity determining regions (CDRs), on each domain are responsible for binding to antigens. The individual specificity and multiplicity of these CDRs are responsible for the antibody paratope, and overall ability of an antibody to target a specific region (epitope) on a specific antigen [15]. The 'body' of the Y-shape forms the fragment crystallisable (Fc) region, typically consisting of two sets of C_H2 and C_H3 domains. This region also contains conserved amino acid residues to which glycans are attached during glycosylation. The Fc region and glycans are responsible for binding and modulating the activity of immune system effectors through Fcγ receptors [16]. Additionally, a $F(ab')_2$ fragment, consisting of the two Fab regions joined by the heavy chain hinge region, can be produced following degradation or protease action [17].

In mammals, five types of Ig exist - IgA, IgD, IgE, IgG, and IgM [18]. These isotypes share the same basic monomeric structure described above, but differ in their constant domains, and thus their Fc and ability to recruit individual aspects of the immune system. Additionally, IgA can exist in a secreted dimeric form, whilst IgM can exist in a secreted pentameric form. The IgG isotype, to which the vast majority of biopharmaceutical mAbs belong [4], is the most common Ig in blood and extracellular fluid. Four different types of IgG exist (IgG1-4) [19], with time-dependent roles in the immune response due to different levels of complement activation and effector cell binding by the Fc regions [20]. IgG molecules are generally inherently stable, with biological half-lives ranging from 7-21 days. As the smallest Ig isotype at ~150 kDa, IgGs are the only antibodies able to perfuse tissue and cross the placenta. Detailed description of the function of the remaining Ig isotypes is outside the scope of this Thesis, and is covered elsewhere [11, 21].

1.1.3 Monoclonal antibody biopharmaceuticals

The high specificity and stability of antibodies, coupled with their ability to recruit the native immune system, makes them an excellent system for a pharmaceutical drug [22]. Antibody biopharmaceuticals are almost exclusively monoclonal antibodies (mAbs), with the same paratope produced from clones of a single B cell, rather than polyclonal antibodies, a mixture of antibodies with different paratopes produced from multiple B cell clones. Experimental production of mAbs *in vivo* began in 1970 following specific selection and propagation of a B cell clone in mice [23]. This was extended in 1975 to enable mAb production *in vitro,* with a hybridoma approach involving fusion of rabbit B cells with an immortal myeloma cell line [24]. Subsequently, the first mAb biopharmaceutical, ORT/OK3, a murine mAb produced in hybridomas and developed to treat transplant rejection, was approved in 1986. This mAb was later withdrawn due to issues of heightened immunosuppression and the immune systems innate response to the foreign murine mAb [25].

The issue of anti-treatment immune responses was partially circumvented in 1986 by the development of humanised antibodies, non-human antibodies whose protein sequences have been modified to more closely resemble human antibodies [26]. The use of humanised hybridomas, development of new production strategies, such as transgenic animals [27] and phage display technologies [28], and an increased interest in the mAb therapy approach has resulted in the recent rapid growth of the mAb biopharmaceutical industry [29].

Recent years have also seen the development of new types of antibody biopharmaceuticals, designed to optimise the particular properties of a treatment (Figure 1-2). Firstly, classical mAbs may have their structure altered in order to achieve optimum function. For example, the Fc region may be engineered to enhance effector function through optimised Fcγ binding [30] or to increase protein half-life through recycling by the neonatal Fc receptor [31]. Alternatively, the Fv region itself may be altered to increase half-life [32]. Glycosylation patterns may also be modified through glycoengineering, including removal of the conserved glycation site to prevent an immune response [33], or incorporation of specific glycans to trigger specific immune cell activation [34].

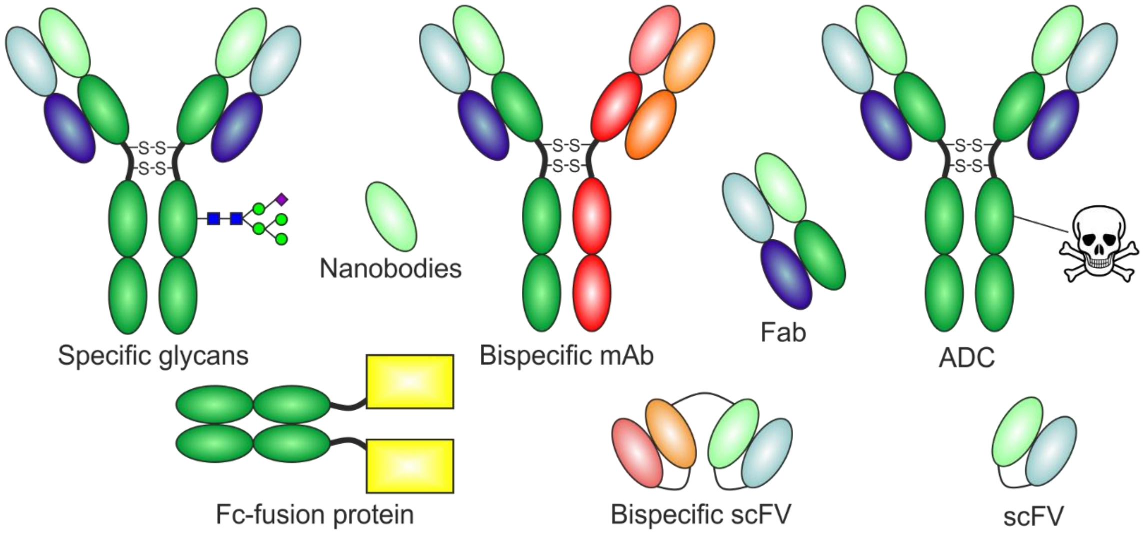

Figure 1-2. Examples of innovative engineered antibodies and related proteins. Constant chains in darker colours, light chains in lighter colours.

Smaller fragments of mAbs may also be used as drug products to exploit the modular nature of antibody molecules [35]. For example, antigen-binding biopharmaceuticals based on the Fab region [36] or the Fv region expressed as a single-chain (scFv) [37] retain the specific binding ability of mAbs, yet may offer greater tumour penetration or more rapid clearance due to their smaller size. Nanobodies, based on fragments of heavy-chain only antibodies found in *Camelidae* mammals, extend this approach further still [38]. Alternatively, the Fc region may be covalently linked to another protein of interest to form an Fc-fusion protein [39] in order to introduce novel immune functions or increase half-life.

Another engineered class of particular interest are bispecific antibodies (BsAbs), which contain two different antigen binding sites as result of different Fv regions [40]. Bispecifics may be generated through replacement of one Fv or Fab region, addition of an additional Fv to an Ig structure, or fusion of two mAb fragments. BsAbs in their various forms are able to interact with two different targets simultaneously alongside their Fc effector functions, which often leads to a beneficial synergistic effect. An example of this approach incorporates a paratope binding tumour cells and another binding T lymphocytes, in order to trigger T lymphocyte mediated tumour destruction [41]. This approach may be extrapolated even further in the creation of trispecific antibodies [42]. Antibodies of all forms may also be covalently linked to small drug molecules to form antibody drug conjugates (ADCs) [43]. This strategy may be used to target cytotoxic drugs to specific cells and reduce systemic off-target effects.

Antibody and related biopharmaceuticals are indicated in the treatment of a wide range of diseases. For cancers of the blood, such as leukaemia, lymphoma and myeloma, or cancers with solid tumours, mAb therapies are one of the most successful treatment strategies [44]. Given that many cancer cells overexpress certain antigens or display unique mutated antigens [45], mAbs generated against these antigens enable specific targeting of these cancers. Targeted destruction of cancer cells is then achieved by activation of the immune system against cancer cells which had previously suppressed immune responses [46], or the action of a cytotoxic payload in ADC therapies [43]. Antibody therapies are also used in the treatment of autoimmune diseases, such as rheumatoid arthritis, inflammatory bowel diseases and psoriasis, triggered by overreaction of the immune system [47, 48]. In these cases, mAb therapies act to supress the aberrant immune system through specific blockage of cytokines or destruction of lymphocytes [49]. Other conditions with antibody therapies include migraines, skeletal diseases and blood clotting disorders [50, 51].

1.1.4 Production and administration of antibody biopharmaceuticals

We will now briefly consider current approaches to mAb production and administration, in order to provide a background for the challenges the biopharmaceutical industry faces in the development and manufacturing of mAb products. Here, we will focus on production processes following successful identification of a biological target and development of a lead mAb.

Biopharmaceutical mAbs are typically produced in mammalian cell lines. These cell lines are capable of producing the post-translational modifications, protein folds and quaternary structures required in antibody molecules [52]. Following transfection of an appropriate cell line, typically Chinese hamster ovary (CHO) or murine myeloma cells

(NS0) [53], cells successfully expressing the product are isolated. These cells are then cultured in bioreactors until they are harvested upon reaching an appropriate density. These processes are collectively referred to as upstream processing [54].

Downstream processing, on the other hand, refers to purification of mAbs from the harvested cell mass, and subsequent preparation of the final drug product [55]. First, the cell mass is collected by centrifugation, with cells disrupted to release the mAb. Next, the protein must be purified to yield a high purity product, free from process contaminants, such as host cell proteins, nucleic acids and viruses. This is typically achieved by chromatography techniques, such as protein A chromatography to first selectively purify the mAb as a result of protein A specific binding to mAb Fc regions [56] coupled with further chromatography techniques, including ion-exchange or size-exclusion, to remove residual impurities [57]. Viruses may be inactivated by incubation at low pH [58]. These extremes of pH or ionic strength during bioprocessing can lead to protein degradation into fragments and aggregates, which themselves must be removed [59, 60].

Following purification, the final drug product must be formulated to prevent chemical and physical instabilities, and therefore ensure protein stability and activity over a product’s shelf-life [61]. This is achieved by formulation optimisation, including selection of an appropriate buffer with optimum pH, and the addition of a range of small molecule excipients, such as salts, amino acids, and surfactants [62, 63]. Additionally, the protein must be sufficiently concentrated to provide an efficacious dose in a given volume. This concentrating step is typically conducted by ultra- or diafilitration steps involving membranes [55, 64]. Biopharmaceuticals can be formulated in liquid or solid form. As mAbs are produced in solution, liquid formulations are easier to produce and administer, but may have a shorter shelf-life due to greater protein degradation in solution [65]. Conversely, mAb solid formulations, while potentially more stable, are more difficult to manufacture and handle, requiring lyophilisation (freeze-drying) during production and reconstitution before administration [66].

Finally, the purified and formulated mAb product can be administered to the patient. At present, biopharmaceuticals are most commonly administered by intravenous (IV) infusion, whereby a large volume is slowly injected into a vein. This typically requires a lengthy hours-long process in a specialised clinical setting with trained medical personnel [67], which leads to higher treatment costs [68]. In light of these requirements, there has been a move towards easier and lower cost administration strategies. Oral administration, whilst the simplest administration approach, is generally unfeasible for biopharmaceutical proteins due to poor membrane permeability and protein degradation in the gastrointestinal tract [69]. However, novel delivery systems [70] and strategies to reduced gastrointestinal degradation [71] are active research areas.

An alternative approach to IV infusion is subcutaneous administration, where the drug is injected into the subcutaneous tissue beneath the skin. Subcutaneous injection is significantly faster and simpler than IV infusion, and results in reduced administration costs and improved patient quality of life [72]. The subcutaneous approach may also allow patients to self-administer biopharmaceutical mAbs, in a manner similar to an insulin pen [73]. Given these benefits, a number of subcutaneous mAb therapies have been recently developed, including for cancer and arthritis treatment [74]. However, subcutaneous injections volumes are limited to ~2 mL by the extracellular matrix, with larger volumes not well tolerated due to painful increases in pressure [75]. This means that mAb therapies for subcutaneous injection must be formulated in solution at high protein concentrations (>100 mg/mL) in order to provide an efficacious dosage within the restricted volume.

1.2 Antibody biopharmaceutical stability

Given the potential benefits of subcutaneous administration of mAbs, there is currently significant interest in the production of high concentration liquid antibody formulations [76]. However, high protein concentrations are associated with a number of physical instabilities, including reversible self-association, irreversible aggregation and liquid-liquid phase separation (LLPS). These instabilities result from reduced inter-protein separation and increased protein-protein interactions at high concentration, and may adversely affect mAb production processes, product quality and treatment safety. Additionally, these instabilities may only present during extended storage of mAbs at refrigerated temperatures, or after thawing following freezing [77]. Overall mAb stability is dependent upon a complex combination of physical and chemical stability. Therefore, in order to develop strategies to maximise protein stability and prevent instability it is important to first gain an understanding of the processes underlying these phenomena.

This Thesis focuses on the physical stability of mAb biopharmaceuticals, in particular self-association, phase separation and aggregation at high protein concentrations. Therefore, mAb chemical stability, which is largely outside of the scope of this work, will only be briefly discussed.

1.2.1 Chemical stability

Chemical instabilities arise from chemical modification of proteins, and result in chemically distinct entities from the base mAb primary structure [78]. Therefore, chemical stability is defined as the ability of a protein to withstand changes to its chemical composition. Given the range of amino acid functional groups, proteins exhibit a wide range of chemical modifications. Reactive oxygen species can oxidise cysteine, histidine, methionine, tryptophan, and tyrosine [79]. Aspartate isomerisation [80] and asparagine deamidation [81] both result in the production of isoaspartate. Disulphide bonds formed by cysteine residues may also undergo a number of alterations, including breakage, shuffling and trisulphide formation [82], which can lead to protein fragmentation. These chemical instabilities can reduce Ig domain stability [83], hinder antigen binding [81], reduce colloidal stability [84], or increase aggregation propensity [85].

The carbohydrate content of mAbs can also be a source of chemical instability. Antibodies may undergo glycation and gain additional covalently attached sugars [86, 87]. This can occur during storage in formulations containing sugars, such as sucrose, which can undergo hydrolysis to form reducing sugars. Glycation can hinder antigen binding [88].

Protein chemical stability is generally well understood, with numerous strategies available to minimise the formation of chemical instabilities. Antibody formulations can be optimised to reduce chemical degradation, for example, through the addition of antioxidants to prevent oxidation [89], or selection of pH and buffer components [90]. Additionally, refrigerated storage and prevention of exposure to high temperature can reduce chemical instabilities by reducing the rates of chemical reactions such as oxidation [91] and glycation [92]. Finally, antibody structure can be engineered to reduced susceptibility to chemical degradation [93].

1.2.2 Physical instability

Physical instabilities, on the other hand, incorporate changes in the conformational or colloidal behaviour of a protein, which can in turn affect solution behaviour. Conformational stability is a protein’s capacity to retain its folded active secondary, tertiary and quaternary structure, and resist unfolding into an inactive conformation [94]. Conversely, colloidal stability refers to a protein’s ability to remain monomeric in solution, without significant attractive protein-protein interactions resulting in the formation of protein assemblies of two or more monomeric units [95]. Additionally, conformational and colloidal instabilities can be intertwined, for example, in unfolding (conformational instability) resulting in aggregation (colloidal instability). Finally, physical instabilities can include reversible processes, such as self-association and phase separation, and irreversible processes, such as aggregation, precipitation and surface adsorption.

1.2.3 Aggregation

Monoclonal antibodies may undergo irreversible aggregation and form stable complexes of two or more monomeric subunits. In solution, proteins exist in a dynamic equilibrium between the folded native state and partially unfolded intermediate states. A wide range of partially unfolded states may exist for a single protein, some of which may be largely stable. However, unfolding may also lead to unstable states due to surface exposure of sticky aggregation-prone regions, which would otherwise be buried within the protein core. Such aggregation-prone regions or ‘hot spots’ are typically highly hydrophobic with low charge density [96]. Interaction of these regions on different protein molecules can result in strong non-covalent interactions, which result in the protein molecules being essentially irreversibly linked. Such oligomers may grow into larger aggregates through addition of sequential unfolded monomer subunits in a polymerisation style reaction [97], or through combination with other oligomers or aggregates [98]. High protein concentrations increase the likelihood of aggregation as a result of reduced spatial separation of proteins and increased likelihood of protein-protein interactions.

Antibodies may also undergo irreversible aggregation as a result of covalent reactions between native or partially unfolded species. Reduction of normal intra-protein disulphide bonds and subsequent unfolding can result in cross-linking of monomer subunits by inter-protein disulphide bonds [99, 100].

Aggregation in biopharmaceutical proteins can be problematic for a number of reasons. Aggregates are typically therapeutically inactive, and therefore reduce the dosage and efficacy of the active pharmaceutical ingredient. Irreversible aggregates are also linked to issues of immunogenicity, in which a patient develops an adverse immune response to the biopharmaceutical product [101]. This immune response results in production of antidrug antibodies, and neutralisation of the biopharmaceutical molecule. While such immunogenicity may occur against monomeric biopharmaceuticals alone, for example, through reactions to specific glycosylation patterns [102], aggregates may increase the risk of an aberrant immune response [103]. Immunogenic responses to biopharmaceuticals can result in reduced treatment efficacy, or potentially serious safety issues, such as anaphylaxis [104].

Protein aggregation can be minimised in mAbs by a number of strategies. Optimisation of formulation conditions, particularly the addition of excipients, such as amino acids, salts, sugars, and surfactants, and selection of buffer components and pH [105-107], can reduce attractive protein-protein interactions and prevent aggregation. Amino acid hot spots responsible for protein aggregation can also be mutated or masked with glycosylation sites to prevent aggregation [108].

1.2.4 Fragmentation

Biopharmaceutical mAbs can undergo fragmentation by non-enzymatic cleavage of the protein backbone or breakage of disulphide bonds linking the light and heavy chains [109]. This results in the formation of smaller fragments of the intact mAb structure, such as a $F(ab')_2$ and a Fc, existing in solution. Fragmentation can be considered both a chemical and physical instability, as it results in significant changes to both the primary amino acid sequence of the mAb and the larger structural conformation.

While peptide bonds in the backbone of proteins are inherently very stable, specific amino acid sidechains, including asparagine and aspartate, can contribute to a hydrolysis reaction and result in the breakage of a peptide bond, particularly in the solvent exposed hinge region [110]. Hydrolysis can also occur due to the action of free radicals, such as hydroxyl radicals [111, 112] or metal ions [113]. Alternatively, reduction of the inter-chain disulphide bonds that maintain mAb quaternary structure can result in fragmentation [82]. This can result from the action of reducing enzymes from mammalian cell lines during expression and purification [114], during processing steps involving low pH [115], or spontaneously during storage.

The effect of fragmentation on the activity and efficacy of a biopharmaceutical mAb are largely dependent on the specific fragmentation site [109]. For example, fragmentation at the hinge region will result in Fabs with intact binding capacities, but without Fc-mediated effector functions. Conversely, fragmentation in the Fv region may prevent antigen binding. Fragmentation is also linked to aggregation, particularly in the case of fragments containing free thiol groups after disulphide reduction [116]. Generally, fragmentation can be seen as a negative process which reduces the concentration of the active monomeric mAb unit and reduces overall product quality. Fragmentation can be reduced through removal of free radicals during production, or formulation near neutral pH [110].

1.3 Self-association and liquid-liquid phase separation

While aggregation and fragmentation are essentially universal protein phenomenon and have been widely studied in mAbs, liquid-liquid phase separation (LLPS) is rarer, and therefore less well characterised. However, the development of high-concentration formulations has increased the occurrence of reversible self-association and LLPS in mAbs, and they are increasingly of interest in the biopharmaceutical industry.

1.3.1 Reversible self-association and viscosity

Protein self-association involves assemblies of two or more protein monomers in their native conformations held together by weak non-covalent interactions. These interactions in mAbs are predominantly electrostatic interactions [117, 118], but also include hydrophobic, van der Waals and dipole-dipole interactions [119]. Due to the retention of native structure and weak interactions, self-association is reversible through dissociation of the supramolecular assembly, leading to the term ‘reversible self-association’. The reversible nature of self-association means that it is an equilibrium process, and so the equilibrium position and degree of self-association can be altered by changing solution conditions, such as protein concentration, temperature, ionic strength, and pH.

In mAb solutions, self-association is primarily observed as increased solution viscosity [120, 121]. At low concentration, solution viscosity is highly dependent upon the electroviscous effect [121], with long range electrostatics resulting from protein net charge dominating. Therefore, at low concentration, increasing viscosity is observed as pH moves away from a mAbs isoelectric point (pI) and net charge increases [122]. Conversely, as protein concentration increases, reduced intermolecular separation means that long range interactions become less important, and short range interactions (e.g. van der Waals and hydrophobic interactions) begin to dominate overall protein-protein interactions.

The attractive or repulsive nature of protein-protein interactions, and the contributions of long and short range interactions are highly dependent upon protein primary sequence [123]. In proteins with attractive short range interactions, high concentrations result in self-association and increased solution viscosity [120, 124]. Conversely, proteins with repulsive interactions may not exhibit self-association. At high concentration, solution pH close to protein pI [120, 125] or ionic screening of long range interactions can result in self-association and high viscosity [126]. Lower temperatures, such as those experienced during refrigerated storage, can also result in increased viscosity due to reduced flow and increased strength of hydrophobic interactions [127, 128], alongside increased viscosity resulting from the surrounding water medium itself.

Reversible self-association and particularly resulting high viscosity can pose a problem throughout the steps of biopharmaceutical manufacturing and administration. During protein concentration by tangential-flow filtration, high viscosity with increasing concentration can result in significant pump back pressure, membrane fouling and reduced filtration [129]. Viscous high-concentration formulations may also be ‘un-syringable’ or ‘un-injectable’ due to the high forces required [127, 130].

1.3.2 The phenomenon of liquid-liquid phase separation

Phase separations are the dissociation of a single phase system into a multi-phase system. They are widespread phenomena throughout science, occurring in simple mixtures of oil and water, in polymer research [131, 132], and in materials [133].

During liquid-liquid phase separation (LLPS), a homogenous medium concentration solution separates into two distinct liquid phases: a low concentration lean phase and a high concentration dense phase (Figure 1-3). This can manifest as microscopic LLPS, with small dense phase droplets interspersed throughout the lean phase. LLPS may be metastable in this suspended droplet state, or progress to macroscopic LLPS by layer separation, with the droplets coalescing and sinking to produce a distinct dense layer with a lean layer above. While the entire process is essentially reversible upon changes in solution conditions or mixing, macroscopic LLPS in protein solutions tends to be significantly harder to reverse than microscopic LLPS.

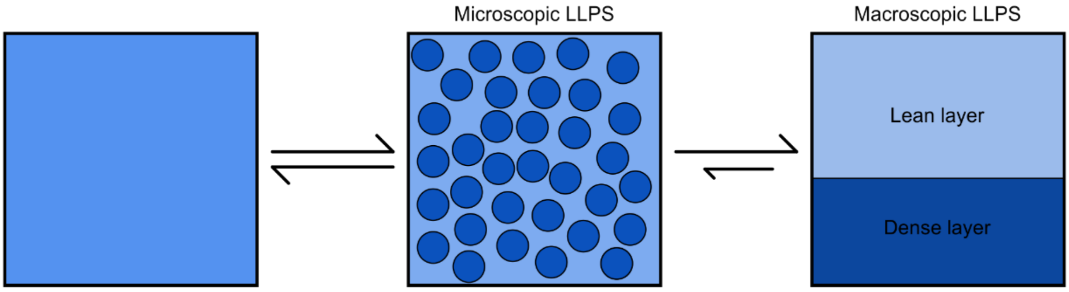

Figure 1-3. Schematic of the process of liquid-liquid phase separation. Colour shading representative of protein concentration, with dark shades indicating higher concentration. Size of dense droplets exaggerated.

The phase behaviour of a system can be defined as a phase diagram (Figure 1-4), with the phase concentrations typically plotted against an experimental condition, such as temperature or salt concentration. These phase diagrams are characterised by binodal and spinodal curves. The binodal or coexistence curve (solid blue lines, Figure 1-4) marks the boundary between phase systems. Outside the binodal curve, the system exists as a single homogenous phase, while inside the curve, the system exists a metastable or unstable mixture of two phases, with concentrations defined by the intercepts of temperature with the curve. The spinodal curve (dashed red lines, Figure 1-4) marks the boundary between the metastable and unstable regions. Outside the binodal curve, the system is stable as a single homogeneous phase. Inside the binodal but outside the spinodal curve, the system is metastable as single phase, but may undergo phase separation by nucleation and growth if large enough fluctuations occur [134]. Conversely, inside the spinodal curve, the system is unstable and prone to phase separation by spinodal decomposition, with infinitesimally small local fluctuations in concentration propagating until two distinct phases are formed [135]. For mAbs, a single mixed coexistence curve is typically observed (Figure 1-4C) [136].

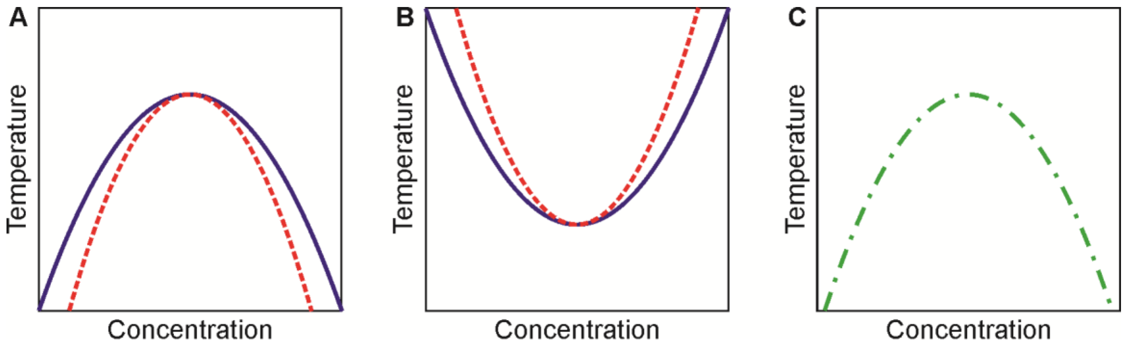

Figure 1-4. Model phase diagrams for phase separating protein solutions. (**A**) Solution with an upper critical solution temperature (UCST). (**B**) Solution with a lower critical solution temperature (LCST). (**C**) Typical phase diagram for a mAb solution with an UCST. Solid blue curves are binodal curves, dashed red curves are spinodal curves, and green dotted-dashed curve is a typical mixed curve for mAb solution.

LLPS can be further classified depending on the onset of LLPS with temperature. In systems with an upper critical solution temperature (UCST) (Figure 1-4A), LLPS only occurs once the solution temperature is beneath the critical temperature (T_C). Conversely in systems with a lower critical solution temperature (LCST), LLPS occurs above T_C (Figure 1-4B).

1.3.3 Opalescence

LLPS is also linked to the phenomenon of opalescence, where a solution appears iridescent milky white or pale blue due to light scattering. Phase separation may cause opalescence by a number of mechanisms. Large self-associated clusters of proteins may scatter light, with larger particles scattering light to a greater extent [136]. Dense droplets in the solution may also scatter light, with concentration and density fluctuations, such as those occurring when the two phases are present simultaneously in microscopic LLPS, also leading to opalescence. Light scattering reaches a maximum near the critical point of the phase diagram, leading to ‘critical opalescence’ [137]. Alternatively, opalescence can arise from mechanisms other than LLPS, such as the presence of suspended precipitates in mAb solutions [138, 139].

1.3.4 LLPS in antibody biopharmaceuticals

In protein solutions, self-association at high concentration may result in LLPS under certain conditions. Therefore, the recent interest in the development of high-concentration formulations has led to observations of LLPS in mAb solutions [140-146].

Monoclonal antibodies typically exhibit LLPS when stored at refrigerated temperatures (UCST-type LLPS) [142]. Solution pH, pI, ionic strength, and interplay between these factors are also major factors in mAb phase separation. The attractive forces responsible for LLPS are generally short-range, and so strongest when long-range forces, such as charge electrostatics, are minimised. Therefore, mAb LLPS is typically seen when formulation pH is close (within one pH unit) to pI [140, 141, 143]. LLPS may occur away from pI if ionic strength or specific additives, such as polyvalent ions, act to neutralise net protein charge [142, 143, 147]. Molecular crowding agents, such as polyethylene glycol (PEG), may also induce LLPS by exaggerating crowding at high-concentration and promoting attractive protein-protein interactions [144, 148].

LLPS is typically undesirable in biopharmaceuticals formulations. If macroscopic LLPS occurs in the final formulated product, then the resulting layers will have markedly different protein concentrations, and dosage may be severely altered. The higher protein concentration in the dense phase may also promote formation of further physical instabilities, such as aggregates or precipitates, and increased solution viscosity. Additionally, cosolutes may partition differently between the two phases as a result of differences in chemical potential due to the Gibbs-Donnan effect at the boundary [149]. This may alter the pH or ionic strength of individual phases, thereby triggering changes in protein stability [142].

Given the potential problem of LLPS in mAb formulations, a number of approaches have been developed to prevent it. As LLPS is driven by attractive protein-protein interactions and self-association, these approaches are shared with methods to reduce solution viscosity. Firstly, conventional high-throughput formulation screens [150] may select conditions, such as pH significantly away from protein pI, where attractive interactions are minimised. Secondly, specific excipients, such as amino acids and salts, may be added to mAb formulations to prevent LLPS [151]. Arginine and the related equimolar mixture of arginine and glutamate (Arg·Glu) [152] have been shown to reduce viscosity and prevent LLPS [153-155]. Inclusion of other proteins, such as human serum albumin (HSA) [156], in formulations may also stabilise mAbs and prevent LLPS. Finally, LLPS of mAbs may be prevented through mutagenesis of protein sequence [157-159]. Such protein engineering approaches aim to reduce sequence-specific attractive hotspots.

1.3.5 Extended phase behaviour of proteins

Phase separation has been previously studied in a number of model protein systems, including serum albumins [160-162], crystallins [163-165] and lysozyme [166, 167]. Alongside studies of LLPS in polymers and other systems, these studies provide a theoretical framework to understand the phase behaviour of mAbs [168]. These proteins may also act as useful model systems to use to develop new experimental methods to study LLPS.

Protein solutions may also undergo extended phase behaviours beyond just LLPS. If attractive interactions between proteins are sufficiently strong, precipitation or liquid-solid phase separation may occur [169]. Upon deep temperature jumps into the spinodal region, phase separation may become arrested, resulting in a glassy protein network [119, 170] or gel formation [171]. Protein crystallisation may also occur, particularly around the critical point of phase separation and in the dense fraction [172, 173].

In the presence of polyvalent ions or salts, proteins may exhibit a variety of behaviours. If LLPS occurs, the properties, such as concentration and volume, of the dense phase may differ depending on salt composition [162, 174]. Reentrant condensation may occur, with a stable homogenous solution existing at low and high salt concentration, but a phase separated liquid or solid state existing at medium salt concentration [160, 175]. This happens due to protein surface charge inversion and electrostatic repulsion effects as salt concentration increases, and is similar to complex coacervation (liquid-solid phase separation) in the presence of large polyelectrolytes, such as poly-amino acids [176-178].

The extended phase behaviours observed above may have a number of potential applications in mAb solutions. Controlled crystallisation may be useful as a method of bioprocessing to produce solid crystalline mAb formulations, or as means to produce samples for structural characterisation by X-ray crystallography [179, 180]. LLPS [136] and liquid-solid phase separation [177, 178] may be useful as novel methods to concentrate mAb solutions and generate high concentration formulations for subcutaneous administration. Therefore, a detailed understanding of protein and mAb phase behaviour may have a number of beneficial applications, alongside developing an understanding of how to prevent LLPS in mAb formulations.

1.3.6 LLPS in biology

Another area where phase separation is increasingly recognised is cell biology, where it has been linked to both normal cellular processes and to disease [181-183]. Cells are typically thought to compartmentalise distinct functions in membrane-bound organelles, such as lysosomes and mitochondria. However, there is growing appreciation of the importance of membraneless structures formed by phase separation. These structures are typically formed of a mixture of ribonucleotides and proteins, leading to the term ribonucleoprotein (RNP) bodies or granules, and include nucleoli [184], Cajal bodies [185] and germline P granules [186]. The proteins in such bodies are typically intrinsically disordered proteins (IDPs) without a fixed stable tertiary structure [187].

Aberrant processes arising from RNP bodies have been linked to a number of neurodegenerative diseases [188, 189]. Phase-separated bodies result in localised high protein concentration, which can promote aggregation and fibrillisation, particularly for proteins with specific disease-associated mutations [190, 191]. Phase separation of biological proteins can also occur outside membraneless organelles. For example, crystallin phase separation and resulting opalescence is linked to eye lens opacity and cataracts [192]. LLPS of antibodies has also been linked to disease, with the formation of antibody containing condensates in cryoglobulinemia [193].

1.3.7 Current approaches to study self-association and protein phase separation

Protein self-association and phase separation can be studied by a variety of biophysical methods. Viscosity measurements or other rheology experiments can be used to infer the occurrence of self-association in protein solutions [124, 154], while sedimentation velocity analysis during analytical ultracentrifugation (AUC) can be used to characterise protein clustering [194].

Optical techniques can also be used to study self-association. Light scattering techniques, such as static (SLS) and dynamic light scattering (DLS), can be used to characterise protein self-association based on a number of parameters, including the diffusion interaction parameter (k_D) and related osmotic second virial coefficient (B_{22}) used to measure the nature of protein-protein interactions, and hydrodynamic radius (Rh) used to measure clustering [195-197]. Additionally, turbidity measurements based on light scattering can be used to study opalescence arising from LLPS [126].

Macroscopic LLPS behaviour under various conditions can be assessed by measuring protein concentration in the resulting layers, and the creation of a phase diagram [146]. Dense droplets present during microscopic LLPS may be detected and characterised by various microscopy techniques. The properties of these droplets may then be examined by a number of methods, including fluorescence recovery after photobleaching (FRAP) to assess mobility inside droplets [186], or atomic force microscopy (AFM) to study droplet stiffness and rigidity [190].

Despite the range of potential biophysical techniques, characterising LLPS remains challenging. For example, opalescence may hinder optical techniques, while layer separation adds a confounding spatial element to analyse. Additionally, microscopy may focus on one small area of the sample at a time, which may not be representative of the entire sample. Therefore, new orthogonal approaches, such as nuclear magnetic resonance spectroscopy, are required to characterise LLPS and other phase behaviour in protein solutions.

1.4 Nuclear magnetic resonance spectroscopy

Nuclear magnetic resonance (NMR) spectroscopy is a powerful analytical technique, which is extensively used in chemistry and biophysics. The range of possible NMR experiments enables detailed study of a wide range of phenomena, from chemical structure [198], to protein dynamics [199], and the behaviour of fluids [200]. NMR is also widely used in medicine in the form of magnetic resonance imaging (MRI) [201]. However, NMR is not widely used in the biopharmaceutical industry, and this Thesis will detail some novel applications of NMR spectroscopy to study mAb biopharmaceutical stability, self-association and LLPS.

1.4.1 Introduction to protein NMR spectroscopy

In NMR spectroscopy, the spectrometer magnetic field results in an alignment of the spins of nuclei inside an NMR sample. Application of a radio-frequency pulse (a weak oscillating magnetic field) results in perturbations of the alignment of these spins, with these perturbations detected and transformed into signals in NMR spectra. The properties of these signals, such as chemical shift, linewidth and intensity, are dependent upon a wide range of factors. These can include factors directly arising from chemical structure, such as specific chemical moieties or the presence of electron withdrawing groups, to factors arising from larger molecular properties, such as diffusion, flexibility and intermolecular interactions.

Proteins are large macromolecules, containing a large number of nuclei, most of which (proton, carbon and nitrogen nuclei) have isotopes which can act as NMR probes to study protein structure and interactions. However, this large number of nuclei results in crowded and overlapping one-dimensional (1D) NMR spectra. Therefore, multidimensional (nD) experiments, such as heteronuclear single quantum coherence (HSQC) spectra used to examine amide protons in the protein backbone, are typically recorded for proteins. As the carbon and nitrogen isotopes (^{13}C and ^{15}N) with spin ½ are found in low natural abundance (1.1% and 0.4%, respectively), proteins are typically specifically labelled with these isotopes to enable timely acquisition of multidimensional NMR experiments [202]. Peaks in the resulting NMR spectra are assigned to specific amino acid residues, with changes in peak parameters used to determine protein structure [203], quantify enzyme kinetics [204], characterise protein oligomerisation [205], and a range of other dynamic processes [206].

Conventional multidimensional protein NMR techniques are however not easily applicable to mAbs. Uniform labelling with ^{13}C or ^{15}N is not easily implemented in the mammalian expression systems used for glycosylated mAb production [207], although some progress has been made recently in expressing glycosylated mAbs in non-mammalian systems [208]. Additionally, mAbs routinely produced in the biopharmaceutical industry are unlabelled. The size of mAbs is also problematic for conventional protein NMR approaches. As molecular size increases, the sheer number of nuclei, coupled with unfavourable broadening of signals as a result of larger molecular size and slower tumbling, mean that even multidimensional spectra become crowded and overlapping. Therefore, high-resolution multidimensional NMR is typically considered to be limited to proteins smaller than 25-30 kDa [209], i.e. much smaller than a 150 kDa mAb. While novel approaches, such as isotopic labelling of methyl sidechains coupled with relaxation optimised NMR experiments [210], have been developed, these are again unfeasible in mAbs produced in the biopharmaceutical industry. Therefore, alternative approaches aside from conventional protein NMR are needed if it is to be used to study large biopharmaceutical proteins such as mAbs.

1.4.2 Application of NMR spectroscopy to biopharmaceuticals

A number of applications of NMR spectroscopy to study biopharmaceuticals have recently been demonstrated.

NMR is well suited to studying the small molecule content throughout the biopharmaceutical pipeline. During manufacturing, NMR can be used to assess excipient quality, such as heterogeneity of polysorbates [211]. Application of a transverse relaxation (T_2) filter to highlight small molecule signals has also been employed alongside 1D ^{1}H NMR to detect the presence of leachables or process impurities [212-214]. Additionally, NMR may be employed to characterise the formulation of biopharmaceuticals. Approaches, such as Saturation Transfer Difference (STD) and Water-Ligand Observed via Gradient SpectroscopY (Water-LOGSY), typically used in fragment-based drug discovery, have been employed to study protein-excipient interactions [107, 215, 216]. Additionally, solid-state relaxation times have been used to study miscibility of sugar excipients in lyophilised formulations [217].

The area where NMR spectroscopy has seen the most interest is in the assessment of biopharmaceutical higher order structure, particularly the creation of characteristic spectral fingerprints for mAbs. These fingerprints are unique to a given mAb sequence, structure and formulation, and so are well suited to compare mAbs from different sources, such as different batches or biosimilars (generic biopharmaceuticals produced following patent expiries). Given the difficulty of isotopically labelling mAbs, two main approaches have developed to fingerprint unlabelled mAbs. 1D mAb fingerprints, known as PROtein FIngerprint by Line shape Enhancement (PROFILE), have been generated by application of the Diffusion Ordered Spectroscopy (DOSY) technique to remove signals from fast diffusing small molecules [218-220]. Alternatively, 2D fingerprints may be generated for unlabelled mAb fragments (Fab and Fc) by both natural abundance ^{15}N and ^{13}C-Heteronuclear Single Quantum Coherence (HSQC) experiments [221, 222]. Such fingerprints have been used to show that polysorbates affect a mAbs stability primarily through interaction with the Fab [223]. Where high-resolution NMR experiments are possible, such as with a small unlabelled peptide [224] or a labelled Fab [225], NMR has been used to more comprehensively characterise biopharmaceutical structure by conventional protein NMR approaches.

Elsewhere, NMR has been used to identify chemical modifications in mAbs, including the presence of pyroglutamate [226], amino acid oxidation [227] and deamidation [228], and galactosylation [229]. Such approaches typically rely on fragmentation of mAbs to more amenable sizes, or the presence of highly specific characteristic NMR signals, such as those arising from pyroglutamate.

There has also been increased interest in studying the solution behaviour of intact biopharmaceutical proteins by ^{1}H NMR spectroscopy. Determination of protein translational diffusion coefficients (D_L) by DOSY NMR has been used in insulins [230, 231] and mAbs [232] to study self-association of different protein variants. 1D ^{1}H signal intensity has also been used to characterise mAb self-association in the presence of excipients [233].

An alternative approach to studying signals directly from the protein is to study signals from a fluorinated tag covalently attached to the protein. This is particularly applicable to studying mixtures of mAbs [234] and other proteins [235]. The flexible linker on such tags means that while the NMR behaviour of the tag reflects that of the linked protein, its NMR signal properties, such as intensity and line width, are more amenable.

Benchtop NMR spectroscopy at low magnetic field strength (typically <1 T compared to >11 T for a high-resolution spectrometer) has also been used to study mAbs. While such spectrometers are unable to record high-resolution spectra, high intensity signals, such as from water, can be used a proxy to detect changes in a sample. For example, the transverse relaxation rate of water has been used to assess mAb concentration and aggregation [236], or to characterise water content in lyophilised mAb formulations [237]. Such benchtop spectrometers may potentially be incorporated ‘in-line’ with bioprocessing steps to enable wider use of NMR without the requirement of significantly more expensive high field strengths.

1.4.3 Application of NMR spectroscopy to study protein phase separation

NMR has also recently been applied to study protein LLPS, particularly in proteins relevant to membraneless organelles and cellular condensates. High-resolution NMR has been used to characterise molecular interactions preceding protein phase separation by a number of methods, including chemical shift perturbation mapping, detection of Nuclear Overhauser Effects (NOEs) and changes in relaxation rates [238-241]. Similar approaches have been applied to study protein structure and dynamics in isolated lean and dense fractions [242-244]. Solid-state NMR has also been used to study protein behaviour in isolated dense fractions [245, 246], with these extremely viscous or gelatinous fractions more closely resembling a solid than a liquid. Finally, in heterogeneous samples with dense droplets present, diffusion and relaxation filtering have been used to selectively observe signals from a single phase [247], although such experiments are non-trivial [248].

The general properties of phase separating systems make them challenging to study by NMR spectroscopy, and particularly high-resolution multidimensional NMR spectroscopy. Firstly, sample heterogeneity, such as the presence of multiple phases, may result in magnetic field inhomogeneity and distorted or broadened NMR signals [249]. Secondly, high viscosity and reduced molecular mobility in the dense phase may result in poor NMR signal properties, such as extreme broadening and low signal intensity [243, 250]. Finally, the transient and rapid nature of phase separation may not be well suited to time consuming multidimensional experiments. Furthermore, most NMR studies thus far have examined only small isotopically labelled intrinsically disordered proteins (IDPs) or domains, instead of larger intact or unlabelled proteins.

Therefore, there is a need to develop new NMR approaches to study LLPS under particularly challenging conditions, such as during macroscopic LLPS, or in challenging experimental systems, such as large unlabelled mAbs.

1.5 NMR techniques used in this Thesis

The remainder of this introduction will introduce NMR techniques used in this Thesis to study antibody biopharmaceutical formulation stability, self-association and phase separation.

1.5.1 Longitudinal and transverse relaxation

In NMR, after excitation by a 90° pulse, the non-equilibrium imbalance of ground and excited states, which gives rise to NMR signals, returns to the original Boltzmann distribution equilibrium state. This occurs as a decay of both the longitudinal (M_z) and transverse (M_{xy}) components of an NMR signals, giving rise to measurable longitudinal (T_1) and transverse (T_2) relaxation times, respectively. T_1 is the time required for M_z to reach 1-(1/e) (~63%) of its maximum value, while longitudinal relaxation rate (R_1) is the rate of this increase ($R_1 = 1/T_1$). Conversely, T_2 is the time required for M_{xy} to decrease to 1/e (~37%) of the initial signal, while the transverse relaxation rate (R_2) is the rate of this decay ($R_2 = 1/T_2$).

Both longitudinal and transverse relaxation occur through mechanisms which are linked to molecular size (Figure 1-5). T_1 relaxation is the exchange of energy from excited to ground states, which results in the reestablishment of spin state equilibrium. This happens due to the interaction of oscillating magnetic fields. These fields are caused by molecular motion and interactions with neighbouring spin systems in molecules or the environment, with T_1 relaxation being most efficient if these fields oscillate at the particular nuclear Larmor frequency. Therefore, in small molecules in liquids, longitudinal relaxation is slow (long T_1, slow R_1) as only a small amount of molecular motions occur at the optimum frequency range. As molecular size or solution viscosity increases, molecular motions approach the Larmor frequency so longitudinal relaxation increases (shorter T_1, faster R_1). However, in very viscous solutions or solids, or for very large molecules, molecular motions are generally slower than the Larmor frequency, leading to slower longitudinal relaxation (longer T_1, slower R_1). However, the exact molecular size/viscosity at which this change in T_1 behaviour occurs is poorly defined.

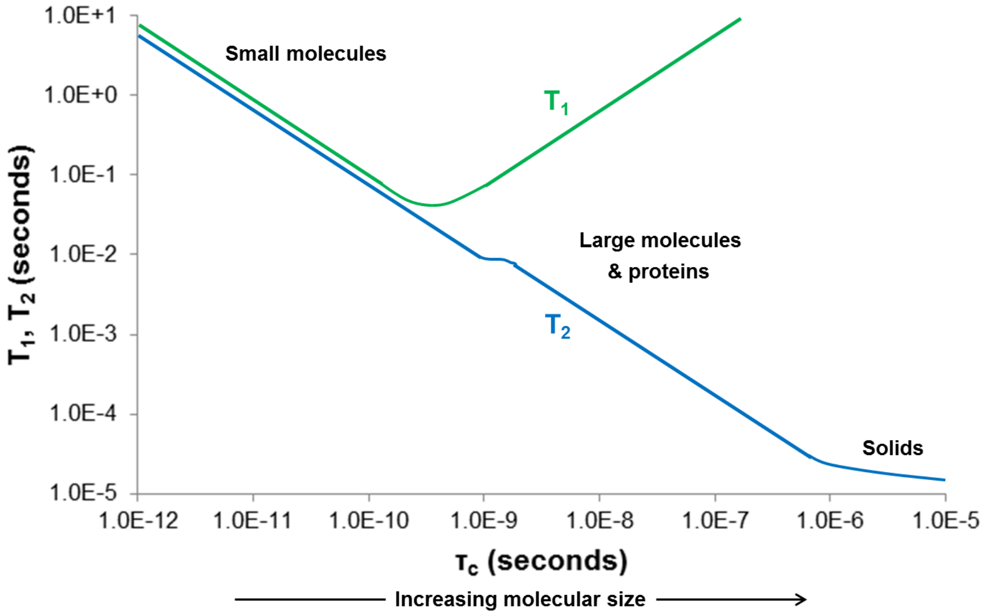

Figure 1-5. Illustration of the relationship between molecular size, and T_1 and T_2 relaxation. Molecular size influences the rotational correlation time (τ_c), the average time for a molecule to rotate through one radian. As rotational correlation time increase, T_2 decreases, while T_1 exhibits more complex behaviour. Positioning of 'large molecules and proteins' label is inexact.

Transverse relaxation is the loss of coherence (i.e. the loss of overall phase alignment between spins) in the xy-plane that results in return to the equilibrium state. Like T_1 relaxation, oscillations of local magnetic fields at Larmor frequency contribute to T_2 relaxation ('T_1 contribution to T_2'), but transverse relaxation also occurs by non-oscillating fields. These local fields lead to spins precessing at different frequencies, and therefore a loss of coherence. Measurements of NMR relaxation rates by inversion recovery or Carr-Purcell-Meiboom-Gill (CPMG) experiments may be used to investigate changes in protein-protein interactions and changes in apparent molecular size.

1.5.2 Dark-state Exchange Saturation Transfer (DEST)

Transverse relaxation contributes to the width of NMR signals, with half-width approximately equal to $\frac{1}{\pi T_2}$ (with an additional contribution from magnetic field inhomogeneity). Therefore, if transverse relaxation is extremely rapid (short T_2 or high R_2), NMR signals may be sufficiently broadened to the point that they are essentially undetectable by standard NMR techniques, and are said to exist in an NMR-invisible ‘dark state’. For proteins, this can occur in sufficiently large assemblies of proteins, such as those resulting from reversible self-association, aggregation or precipitation, particularly if the proteins themselves are large (e.g. mAbs).

One NMR method for studying these dark states is Dark-state Exchange Saturation Transfer (DEST) [251, 252]. In NMR, application of continuous-wave (CW) radio waves or repeated pulses can be used to saturate NMR signals, that is, flip their signals into the *xy*-plane and allow longitudinal relaxation to reduce the resulting signal. In DEST, application of selective CW saturation to the frequencies covered by the broadened dark-state, results in saturation of the dark-state (Figure 1-6). If the dark-state exists in exchange with an NMR visible state, such as in the case of a protein undergoing reversible self-association, then the saturation will pass to the visible state, and result in detectable attenuation of the observable NMR signal. Mapping of this signal attenuation at different frequency offsets, and fitting of the resulting DEST profile to Bloch-McConnell equations for a two-state exchange model [253] enables quantification of the population and relaxation rates of the NMR dark state.

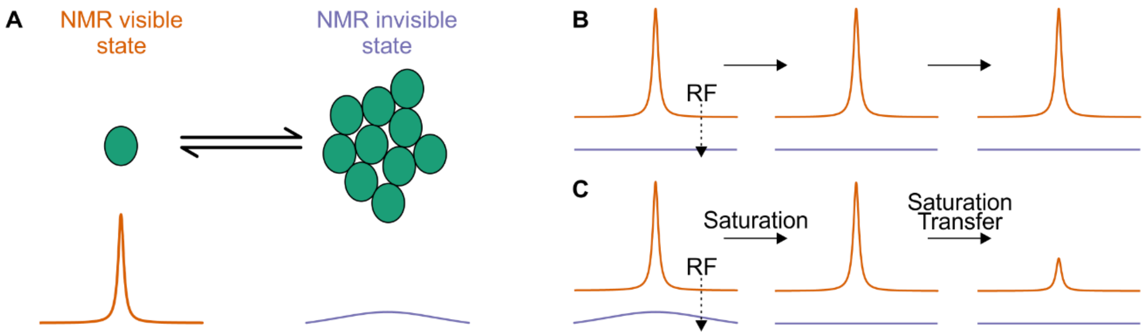

Figure 1-6. Detection of NMR invisible dark states by DEST. (**A**) Exchange between NMR visible and invisible states, with their respective NMR spectra below. Intensity of invisible state exaggerated for clarity. (**B**) In the absence of a dark state, an RF saturation pulse applied offset of the NMR visible species has no effect on the observed signal. (**C**) In the presence of a dark state, the saturation pulse saturates the dark-state, with this saturation then transferring to the visible state by exchange, resulting in attenuation of the observed signal.

DEST has been applied to study the formation of amyloid fibrils [252], as well as the interaction between small molecules and nanoparticles [254, 255].

1.5.3 Translational diffusion

The translational diffusion coefficient (D_L) is a measure of the speed at which molecules move across a given axis of a solution. This diffusion of a spherical particle in a dilute solution is governed by the Stokes-Einstein relationship:

$$D_L = \frac{k\,T}{6\pi\,\eta\,R_h} \qquad \text{(Equation 1.1)}$$

where k is Boltzmann's constant, T is temperature, η is dynamic viscosity, and R_h is the hydrodynamic radius of the particle.

In NMR, D_L is typically measured using pulsed field gradients in so called diffusion-ordered spectroscopy (DOSY) experiments [256]. Standard spectrometers, such as the ones used in the preparation of this Thesis, have a single Z gradient coil, which runs along the vertical length of the sample. Gradient coils, as the name suggests, apply a small linear magnetic field gradient along their axis, such that different positions in space experience slightly different magnetic fields. Due to these spatial differences in field strength, the Larmor frequency of molecules varies along the length of the sample, encoding a spatial component to NMR signals.

In pulsed gradient DOSY experiments, after initial excitation with a 90° pulse, a pulsed field gradient (gradient length δ) is used to encode spatial position. During a given diffusion time (Δ) in which the NMR signals decay by dephasing, a 180° pulse (in spin echo experiments) or a set of 90° pulses (in stimulated echo experiments) is used to refocus signals. Finally, a second matched field gradient pulse is used at the end of Δ to decode the initial spatial encoding. Molecules which have moved in the Z-axis during Δ will not be effectively refocused, and so the observed signal will reduce. As the field gradient strength (g) is sequentially increased in DOSY experiments, signal attenuation follows an exponential decay behaviour:

$$I = I_0 e^{-D_L \gamma^2 g^2 \delta^2 (\Delta - \frac{d}{3})} \qquad \text{(Equation 1.2)}$$

where I is the observed intensity, I_0 is the reference intensity in the absence of gradients, and γ is the gyromagnetic ratio of the observed nucleus. Therefore, D_L can be calculated by fitting DOSY signal decay to (Equation 1.2).

DOSY is typically used to separate signals in mixtures with components diffusing at different rates [257], which has been exploited in mAb samples to remove NMR signals from fast diffusing excipient molecules [218]. DOSY has also been used to study the self-association behaviour of biopharmaceutical insulins [230, 232].

1.5.4 Spatially-selective NMR

LLPS, particularly layer separation, results in differences in the distribution of phases across the sample, and thus an inhomogeneous sample. Generally, such samples are difficult to study by NMR spectroscopy due to poor magnetic field homogeneity (despite shimming), which results in distorted and broadened NMR lineshapes, on top of broadening resulting from high viscosity and slow molecular tumbling. Additionally, conventional bulk-detection NMR, in which spectra are recorded from the entire sample in the NMR coil region, is not well suited to studying the spatial distribution of phases or layers.

Spatially-selective NMR is an experimental technique which enables acquisition of signals from a specific volume or ‘slice’ of the NMR sample [258, 259]. Here, spatially-selective NMR will be considered in a single dimension, along the vertical Z-axis which aligns with the length of the NMR sample and the Z-axis gradient coils in most modern spectrometers. However, an extension of this approach into three-dimensions is magnetic resonance imaging (MRI), most typically applied in medicine [201].

In spatially-selective NMR, application of a magnetic field gradient by the Z-gradient coils (G_z) results in nuclei experiencing different total magnetic fields relative to their vertical position (Z) in the sample (Figure 1-7A). Therefore, the nuclei spin at different resonance frequencies relative to their position, encoding a spatial component to their NMR signals:

$$\Omega = \gamma \; G_z \; Z \qquad \text{(Equation 1.3)}$$

where Ω is the offset from the original resonance frequency (in Hz), γ is the gyromagnetic ratio of the nuclei (in Hz T^{-1}), G_z is the applied gradient (in T mm^{-1}), and Z is the vertical position relative to the centre of the gradient coils (in mm). Application of a selective radio-frequency pulse, such as a Gaussian pulse cascade [260], during this gradient, selectively excites nuclei in a defined horizontal slice of the sample:

$$\Delta Z = \frac{\Delta B}{\gamma \, G_z} \qquad \text{(Equation 1.4)}$$

where ΔZ is the thickness of the horizontal slice (in mm), and ΔB is the bandwidth of the selective radio-frequency pulse (in Hz). The gradient is subsequently turned off and the signals from the excited slice are then acquired at their normal resonance frequencies (Figure 1-7B).

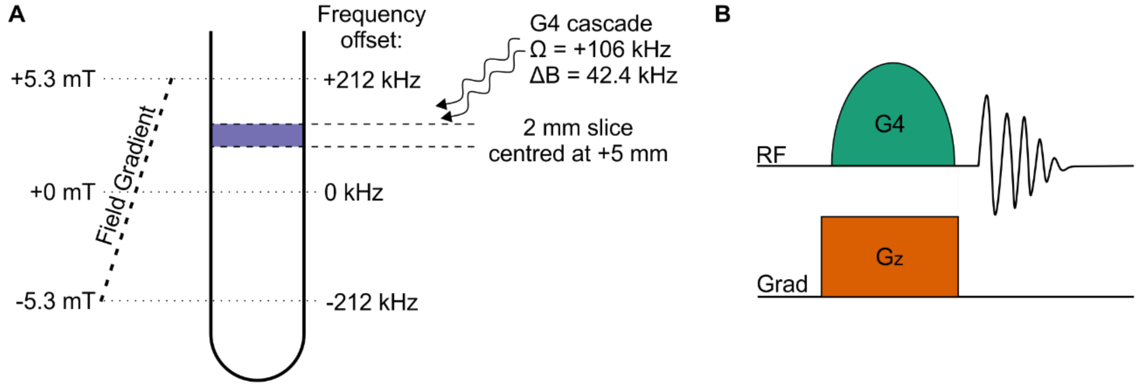

Figure 1-7. Spatially-selective NMR. (**A**) Schematic of spatially-selective NMR with representative values for ^{19}F NMR on a 470 MHz (11.7 T) NMR spectrometer. Application of a 5.3 mT cm^{-1} magnetic field gradient results in ^{19}F nuclei at +5 mm above the coil centre experiencing a +106 kHz frequency offset. A selective RF pulse with a bandwidth of 42.4 kHz applied at this offset excites a 2 mm slice (in purple), centred at +5 mm. (**B**) Basic pulse sequence for spatially-selective NMR.

Spatially-selective NMR can be used to study complex inhomogeneous solutions [249, 261, 262]. Additionally, magnetic field inhomogeneity in individual slices is smaller than across the whole sample, resulting in narrower undistorted lineshapes, particularly in inhomogeneous samples. These make spatially-selective NMR potentially well-suited to characterise LLPS. However, sensitivity is markedly reduced compared to bulk-detection NMR as a result of acquiring from a significantly reduced sample volume

[263]. Furthermore, the total volume observable by spatially-selective NMR experiments is lower than bulk-detection NMR as a result of gradient non-linearity approaching the edges of the gradient coils [264].

1.6 Introduction to the Thesis

This PhD Thesis was conducted as part of a Doctoral Training Partnership (DTP) programme, supported by the Biotechnology and Biological Sciences Research Council (BBSRC). Additionally, this work was conducted as part of a Collaborative Awards in Science and Engineering (CASE) studentship, involving a partnership with an industrial sponsor.

Here, the industrial sponsor was AstraZeneca UK, a global pharmaceutical and biopharmaceutical company with headquarters in Cambridge, UK. This work was specifically completed with the biologics division of AstraZeneca (MedImmune prior to 2019), who provided funding and a set of monoclonal antibodies to conduct experiments on, and offered an industrial perspective on the project. Additionally, a total of three months placement was undertaken at AstraZeneca's Granta Park site in Cambridge, providing access to biophysical techniques commonly employed in biopharmaceutical formulation.

1.6.1 Aims and structure of this Thesis

The main aim of this Thesis was to develop new NMR approaches to study the stability, self-association and liquid-liquid phase separation of antibody biopharmaceuticals by NMR spectroscopy.

This Thesis is presented in a journal format, with this first chapter providing a general introduction to the topic area. Chapters 2-6 are presented in the form of individual manuscripts, with separate Introduction, Material and Methods, Results, Discussion, and Supporting Information sections. The final Chapter is a general conclusion and discussion where the overall results of this Thesis are summarised and discussed in light of the initial aims of the project.

This Thesis initially focuses on using ^{1}H NMR spectroscopy to study mAbs. In Chapter 2, we demonstrate that ^{1}H NMR can be used to assess the stability of both the protein and excipient components of biopharmaceutical formulations, while in Chapter 3 we employ ^{1}H NMR alongside conventional formulation characterisation techniques to explore the use of LLPS as a method to concentrate mAb solutions. The second half of the Thesis then focuses on using ^{19}F NMR spectroscopy to study the self-association and LLPS of mAbs and other model proteins. In Chapter 4, we develop the use of Dark-state Exchange Saturation Transfer (DEST) NMR to study the self-association and clustering of mAbs covalently tagged with ^{19}F tags. In Chapter 5, we employ a fluorinated probe molecule, which is sensitive to local protein concentration, to study the phase and layer separation of a model protein, bovine serum albumin (BSA), by ^{19}F NMR. In Chapter 6, we extend this approach to study the phase and layer separation of a mAb.

2 Comprehensive assessment of protein and excipient stability in biopharmaceutical formulations using ^{1}H NMR spectroscopy

This chapter was written, peer-reviewed and published as:

Jack E. Bramham[1], Adrian Podmore[2], Stephanie A. Davies[2], and Alexander P. Golovanov[1], Comprehensive assessment of protein and excipient stability in biopharmaceutical formulations using ^{1}H NMR spectroscopy, *ACS Pharmacology & Translational Science,* **2021** 4(1):288-295, doi: https://doi.org/10.1021/acsptsci.0c00188

[1] Manchester Institute of Biotechnology and School of Chemistry, Faculty of Science and Engineering, The University of Manchester, Manchester, M1 7DN, UK
[2] Dosage Form Design & Development, BioPharmaceuticals Development, R&D, AstraZeneca, Cambridge, CB21 6GH, UK

Author contributions:

J.E.B. performed experiments, analysed the data, and drafted the manuscript. A.P. and S.A.D. supplied the Abs and provided guidance and supervision from an industrial perspective. A.P.G. conceived and supervised the project and provided input regarding data analysis. The manuscript was written through contributions of all authors. All authors have given approval to the final version of the manuscript.

2.1 Abstract

Biopharmaceutical proteins are important drug therapies in the treatment of a range of diseases. Proteins, such as antibodies (Abs) and peptides, are prone to chemical and physical degradation, particularly at the high concentrations currently sought for subcutaneous injections, and so formulation conditions, including buffers and excipients, must be optimised to minimise such instabilities. Therefore, both the protein and small molecule content of biopharmaceutical formulations, and their stability are critical to a treatment's success. However, assessing all aspects of protein and small molecule stability currently requires a large number of analytical techniques, most of which involve sample dilution or other manipulations which may themselves distort sample behaviour. Here, we demonstrate the application of ^{1}H nuclear magnetic resonance (NMR) spectroscopy to study both protein and small molecule content and stability *in situ* in high concentration (100 mg/mL) Ab formulations. We show that protein degradation (aggregation or fragmentation) can be detected as changes in 1D ^{1}H NMR signal intensity, whilst apparent relaxation rates are particularly sensitive to Ab fragmentation. Simultaneously, relaxation filtered spectra reveal the presence and degradation of small molecule components such as excipients, as well as changes in general solution properties, such as pH. ^{1}H NMR spectroscopy can thus provide a holistic overview of biopharmaceutical formulation content and stability, providing a preliminary characterisation of degradation and acting as a triaging step to guide further analytical techniques.

2.2 Introduction

Biopharmaceutical antibodies (Abs), such as monoclonal antibodies (mAbs) and, more recently, bispecific antibodies (BsAbs), are increasingly important therapies in the treatment of a wide range of diseases, including cancer, arthritis, and diabetes. Within the biopharmaceutical industry, there is considerable interest in the development of high-concentration (>100 mg/mL) protein formulations to enable subcutaneous administration of the lowest possible volume injection [67, 75], potentially by the patient themselves [72]. Such administration strategies result in lower treatment costs and better patient experience, particularly in the treatment of chronic conditions such as autoimmune disorders [265]. However, high protein concentrations are associated with increased levels of physical instabilities, such as self-association [120, 266], aggregation

[267], and liquid-liquid phase separation (LLPS) [59, 140, 143], in addition to chemical degradation, such as fragmentation [82, 268] and oxidation.

To ensure therapeutic proteins remain stable and therefore safe and efficacious at high-concentrations, formulation conditions, such as buffers, pH, ionic strength, and small molecule excipients, must be optimised [269, 270]. In this regard, the long-term stabilities of both the protein molecules themselves and the small molecule formulation components are important. Degradation of the small molecule components required for protein stability [271, 272], or their reaction with proteins [86, 92], may subsequently lead to protein instabilities. Optimisation of formulation conditions, and continued assessment of formulation stability, requires analytical techniques capable of assessing both protein and small molecule content and behaviour, ideally *in situ* in intact formulations. However, in practice, a wide range of techniques are deployed [273-275], and these techniques typically require manipulation of high-concentration formulations, such as dilution, addition of a probe molecule, or salt removal, potentially leading to changes in protein and small molecule structure and behaviour.

Nuclear magnetic resonance (NMR) spectroscopy is a powerful biophysical technique, which can be applied *in situ* at high concentration without sample dilution. The range of NMR experiments, from saturation transfer for detection of protein-excipient interactions [215, 216], to diffusion and relaxation assessment of mAb solution behaviour [232, 276], and fingerprinting of mAbs and biosimilars higher-order structure [218, 277, 278] mean that NMR can be used to study a wide range of biopharmaceutical problems. In formulation studies, NMR has been used to characterise the presence of residual small molecule contaminants from bioprocessing [212, 214] and to quantify small molecule levels [279], whilst low resolution benchtop spectroscopy has been applied to study mAb degradation based on broad changes in the relaxation rate of the water signal [280, 281]. For complex formulations, there may be advantages in observing multiple parameters to characterise multiple degradation pathways, and in principle high-resolution ^{1}H NMR allows observation of all proton containing species, including proteins and small molecules.

Here, we explore the use of high-resolution ^{1}H NMR spectroscopy to report on the content and behaviour of both small molecule and Ab protein components simultaneously in model formulations. For three high concentration Abs (100 mg/mL) stored under stressed stability conditions (40°C), we demonstrate that complex ^{1}H NMR spectra of Ab solutions can be separated into small molecule and protein regions by the application of a simple transverse relaxation (T_2) filter. Having spectroscopically separated protein and small molecule components, we show that the signal intensities and apparent relaxation rates of Abs can be used to monitor protein stability and the occurrence of degradation, such as aggregation and fragmentation, over a 12-week period. NMR observations are compared with a standard size-exclusion chromatography analysis. Additionally, the appearance, intensity and chemical shift of small molecule components can be simultaneously used to study the presence and degradation of excipients themselves, as well as changes in general solution properties, such as pH. Through the use of sealed NMR tubes with coaxial inserts, these assessments are observed *in situ* at high concentration without sample dilution or manipulation. We demonstrate that ^{1}H NMR spectroscopy is a suitable orthogonal technique to provide a comprehensive overview of formulation content and stability, and can act as a triaging step to guide further detailed analysis.

2.3 Materials and Methods

2.3.1 Sample preparation

Two mAbs and a BsAb were supplied by AstraZeneca – COE-03 (IgG1, MW 144.8 kDa, pI 8.44), COE-07 (bispecific IgG1, MW 196.7 kDa, pI 8.0), and COE-19 (IgG1, MW 148 kDa, pI 7.4 – 7.9). All Abs were dialysed (six buffer exchanges over three days) into 20 mM phosphate buffer, pH 6.5 (sodium phosphate dibasic (Na_2HPO_4) and sodium phosphate monobasic (NaH_2PO_4) (both Sigma-Aldrich)), with 200 mM NaCl (Fisher) in GeBAflex-Maxi-tubes (MWCO 8 kDa, Generon, rinsed with 20% ethanol and then distilled water). Small molecules from the original formulations remaining after this extensive dialysis, and the phosphate buffer with NaCl, were treated as the final model formulations. Sample concentration was conducted in Vivaspin 20 centrifugal concentrators (MWCO 30 kDa, Sartorius), with final solutions filtered using 0.22 µm filters (PVDF, Merck Millipore). Concentration measurements were based on absorbance at 280 nm (A280) using known extinction coefficients and a NanoDrop spectrophotometer (Thermo Scientific).

All samples were prepared to 100 mg/mL protein concentration, with 0.05% sodium azide (Fisher) added to prevent bacterial growth. Samples for NMR spectroscopy (400 µL) were prepared in triplicate and placed in 5 mm borosilicate glass NMR tubes (Wilmad-LabGlass), with a coaxial insert (50 mm stem height, Wilmad-LabGlass) containing 60 µL ^2H_2O (Sigma-Aldrich) to provide spectrometer lock without sample dilution or change in formulation. Samples (one per time point) for HPSEC were placed in borosilicate glass vials (Sigma-Aldrich, 1 mL). All samples were sealed with an appropriate cap and Parafilm wrap (Cole-Parmer), and stored upright at 40°C in a Heratherm compact incubator (Thermo Scientific, uniformity ±1.2°C, stability ±0.2°C). One non-NMR sample per Ab was frozen at each time point for analysis at a later date.

2.3.2 NMR spectroscopy

NMR experiments were acquired at 40°C using a Bruker 800 MHz Avance III spectrometer equipped with 5 mm TCI cryoprobe and variable temperature control unit, with temperature calibrated against a standard methanol sample and verified with an external thermocouple placed in a sample tube.

^1H 1D spectra were recorded using WATERGATE water suppression (p3919gp Bruker pulse program), with this water suppression also used in relaxation experiments. Longitudinal relaxation rates (R_1) were measured using the standard Bruker inversion recovery sequence (t1ir), with 10 recovery delays ranging from 1 ms to 3 s. Transverse relaxation rates (R_2) were measured using a Carr-Purcell-Meiboom-Gill (CMPG) sequence, with temperature compensation to ensure equal sample heating during the CPMG acquisition and a fixed echo time of 3.6 ms. T_2 filtered spectra were extracted from the CPMG data, with 32 echoes producing a 116 ms relaxation filter.

Spectra were processed and analysed using Topspin 4.0 (Bruker). Apparent ^1H longitudinal and transverse relaxation rates at spectral points (0.05 ppm intervals) across the spectral width were calculated in Dynamics Center 2.6 (Bruker). Relaxation rates were fitted to single component models, with two or more component models not significantly improving fitting. The processed data were plotted in GraphPad Prism 6.0.

2.3.3 High Performance Size Exclusion Chromatography

Analysis of mAb and BsAb monomeric, aggregate, and fragment species was performed using high performance size exclusion chromatography (HPSEC). This was performed using an Agilent 1200 system with a TSKgel SW_{XL} column (30 cm x 7.8 mm, 5 µm particle size, Tosoh Bioscience). Samples were diluted to 10 mg/mL and 0.45 µm filtered prior to assessment with centrifugal filters (Ultrafree-MC-HV, Merck Millipore). 25 µL was injected each time and the system was run at 1.0 mL/min, with a mobile phase of 0.1 M Na_2HPO_4, 0.1 M Na_2SO_4, pH 6.8. Absorbance wavelength for detection was set at 280 nm. Chromatograms were analysed in ChemStation (Agilent).

2.4 Results

2.4.1 Initial NMR characterisation of formulation content

Protein formulations are routinely stored at elevated temperatures to trigger degradation and infer long term formulation stability. Here, we used this stressed stability approach to explore how ^{1}H NMR spectroscopy can be used to study the content and stability of non-labelled Abs samples, such as those obtained from mammalian production pipelines which do not permit easy isotope labelling. First, the initial baseline ^{1}H NMR spectra and parameters were recorded for each of the three Ab formulations at 40°C (at time t=0). The acquired NMR spectra represent a complex mixture of overlapping protein and small molecule signals (Figure 2-1A). Despite this overlap, some spectral regions are clearly dominated by sharper, more intense signals arising from small molecules, which are also often present in much larger concentrations. As measuring individual proton longitudinal (R_1) or transverse (R_2) relaxation rates is impossible, we measured the apparent relaxation rates for each point in the spectra at 0.05 ppm intervals, thus providing a characteristic relaxation profile for each formulation (Figure 2-1B and 1C). As large and small molecules have significantly different tumbling rate, their R_2 is also significantly different. Factoring that excipients and small molecules have $R_2<75\ s^{-1}$ the spectra can be classified into regions dominated by Ab signals (shown in white) and small molecules (shown in grey).

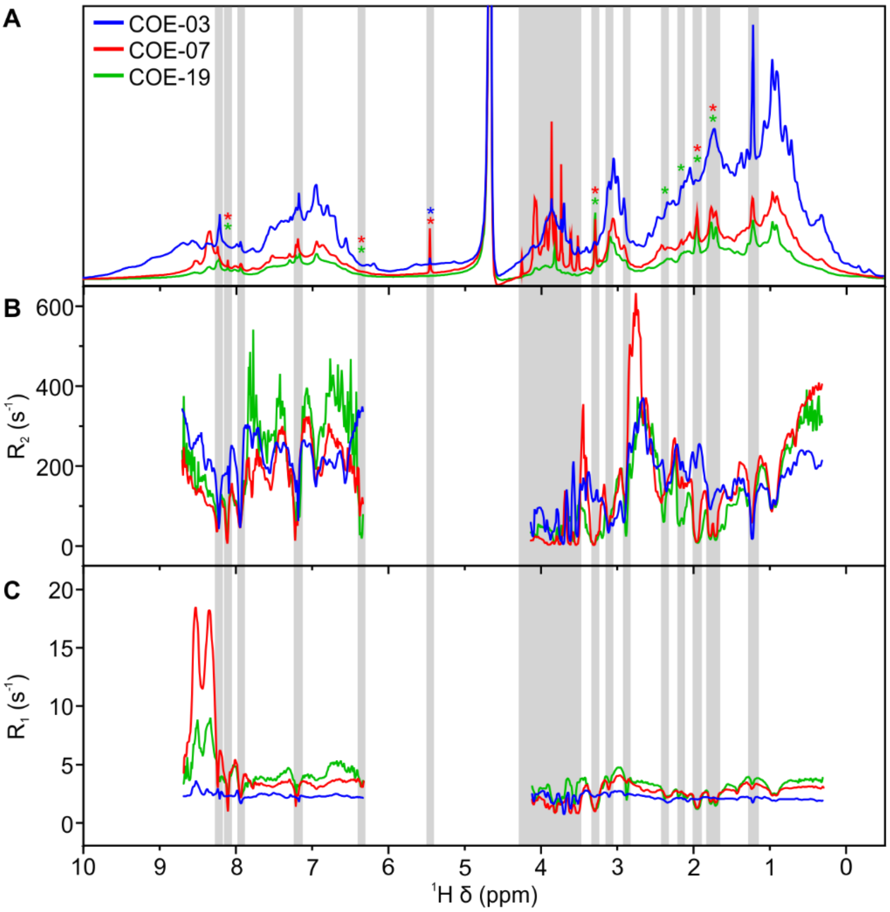

Figure 2-1. Initial NMR spectra and relaxation rates of the three Abs recorded at 40°C. (**A**) ^{1}H NMR spectra overlay of COE-03 (blue), COE-07 (red), and COE-19 (green). Apparent R_2 (**B**) and R_1 (**C**) were measured for each spectral point. Mean rates from triplicate samples. Grey areas include signals arising from small molecule components. Coloured asterisks indicate small molecules present in specified Ab samples only. Blank regions in apparent relaxation spectra were excluded due to low signal and large measurement errors. Residual water signal at 4.7 ppm.

In the protein-dominated regions of ^{1}H spectra (Figure 2-1A), the three Abs display markedly different signal intensities despite identical protein concentrations and similar formulations. COE-07 and COE-19 signals generally exhibited faster relaxation rates than COE-03 (Figure 2-1B-C). These spectra and parameters indicate that COE-07 and COE-19 exhibit greater self-association than COE-03, in agreement with previous observations of the three Abs' behaviour [282]. Noticeably, despite the differences elsewhere, the characteristic Ab methyl signals at 0.9-1.0 ppm result in similar R_1 and R_2 values for all three Abs, suggesting this invariant spectral region represents a flexible structural feature common to all Abs tested. Additionally, R_1 values in the protein spectral region around 8.5 ppm appear acutely sensitive to differences between the Abs.

The presence of small molecule components (shaded grey in Figure 2-1) is easily identified by their slow R_2, and their separated spectra is most conveniently obtained by running T_2 filtered experiments [214] (Figure S2-1). These T_2-filtered spectra reveal the presence of residual components from the original formulations which were not completely removed by multiple rounds of dialysis during sample preparation – histidine in all three Abs, sucrose in COE-03 and COE-07, and arginine in COE-07 and COE-19. Additionally, trace ethanol was present in all Ab solutions, likely carried over from washing dialysis membranes before use. Protein translational diffusion (D_L) in principle may also report on molecular size [232], however for such concentrated Ab solutions the quality of ^{1}H DOSY spectra was very poor for Ab signals (data not shown) due to particularly fast relaxation and slow diffusion. Therefore, relaxation profiling using R_1 and R_2 values provides a sensitive alternative for characterising highly-concentrated Ab formulations.

2.4.2 Changes in Ab 1D ^{1}H NMR spectra upon accelerated stability storage

Having acquired baseline spectra and parameters for the Ab and small molecule components at the initial time point, NMR experiments were subsequently acquired after 1, 2, 3, 4, 8, and 12 weeks storage at 40°C for the same sealed samples. 1D ^{1}H NMR spectra represent the simplest and fastest acquired experiments, so they may provide the easiest assessment of Ab stability. The ^{1}H NMR spectra of COE-07 and COE-19 exhibit increases in signal intensity with time (Figure 2-2), indicating protein degradation. Noticeably, the upscaled spectra of these Abs retain the same overall shape as the initial spectra. As the amount of material present in the sample remains the same, the broad increase in signal intensity across the spectra for COE-07 and COE-19 suggests predominantly fragmentation occurring, resulting in smaller freely tumbling Ab domains. These retain the same general spectral profile as the intact Ab due to the same domain fold, but have higher apparent signal intensity due to their smaller molecular weight and hence faster rotational correlation time (τ_c). However, mAb disaggregation, which would produce similar behaviour, cannot be ruled out. Conversely, COE-03 spectra were largely unchanged, even after 12 weeks storage at 40°C.

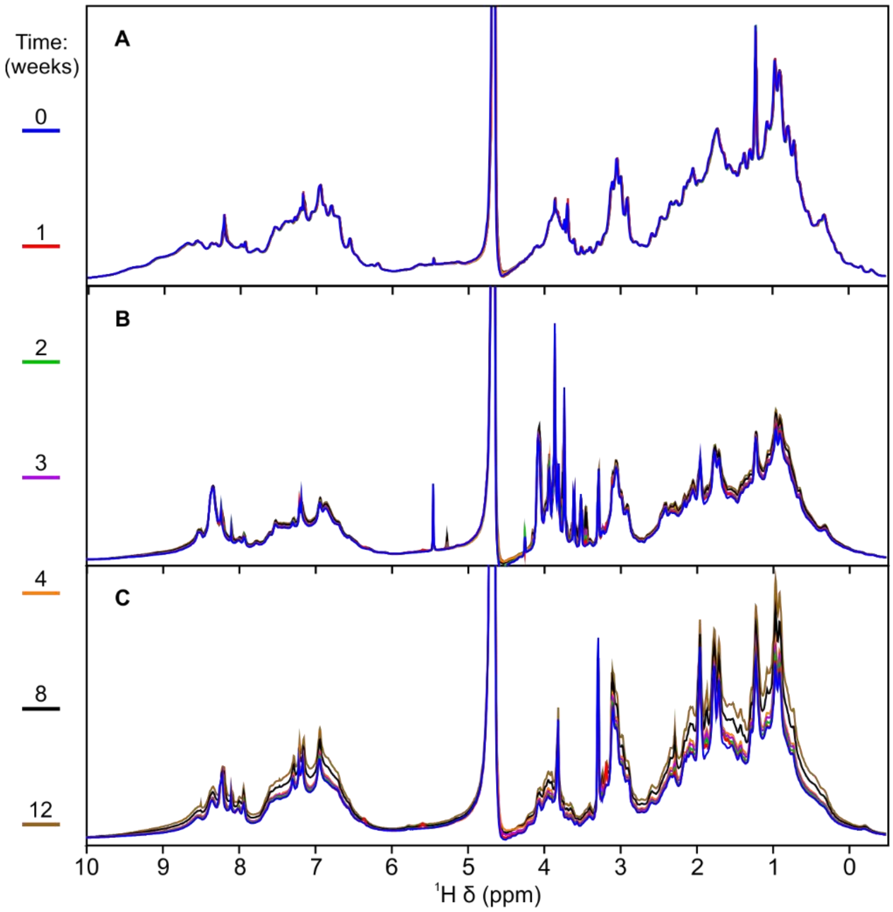

Figure 2-2. Changes in ^{1}H NMR spectra during accelerated stability storage at 40°C over time. (**A**) COE-03, (**B**) COE-07, and (**C**) COE-19. Spectra for COE-07 and COE-19 are scaled up for clarity two-fold and three-fold, respectively, compared to COE-03 spectra.

We have previously shown that protein aggregation results in decreases in observed signal intensities as slower-tumbling or NMR-invisible species are formed [233]. Therefore, the predominant changes in NMR signal intensity for a given sample reveal the predominant underlying Ab degradation process, with increasing and decreasing intensities reflecting fragmentation and aggregation, respectively. In a more complex scenario, if both fragmentation and aggregation occur simultaneously it may be envisaged that opposing changes in intensity may largely balance each other (see Figure S2-2 for illustrative modelling). As we will show, this is the case for COE-03, where no significant change in intensity is observed (Figure 2-2A). In such a situation, additional spectral considerations need to be taken into account to correctly interpret whether no degradation has occurred, or whether fragmentation and aggregation have occurred simultaneously.

2.4.3 Changes in protein apparent relaxation rates during accelerated stability storage

Given the potential complex behaviour of 1D ^{1}H NMR spectra in response to degradation, we next considered changes in apparent relaxation rates. Large protein aggregates, such as those resulting from >150 kDa Abs, with slow τ_c and rapid R_2 are likely largely ‘NMR-invisible’ and as such make a negligible contribution to the measured apparent rates. Conversely, small protein species with faster tumbling are expected to contribute more prominently. For all three Abs, the apparent R_2 values for protein-dominated spectral regions show a tendency to decrease with storage time (Figure 2-3). The reductions in Ab R_2 with time are larger for COE-07 and COE-19 than for COE-03, both for absolute values (Figure 2-3A-C) and for relative values expressed as a percentage of the original R_2 values (Figure 2-3D-F). As the R_2 rate for a large protein is roughly proportional to the molecular size, the observed decreases in R_2 are consistent with an average decrease in the molecular size of the observed species i.e. the occurrence of protein fragmentation. In this respect, the changes in absolute R_2 values for the spectral region around 2.8 ppm appears to be particularly sensitive to fragmentation given its relatively high initial R_2 for all three Abs. The behaviour in spectral regions dominated by small molecule signals is more complex, and cannot be interpreted based solely by R_2 values. Our further analysis (below) reveals chemical changes occurring for these formulation components.

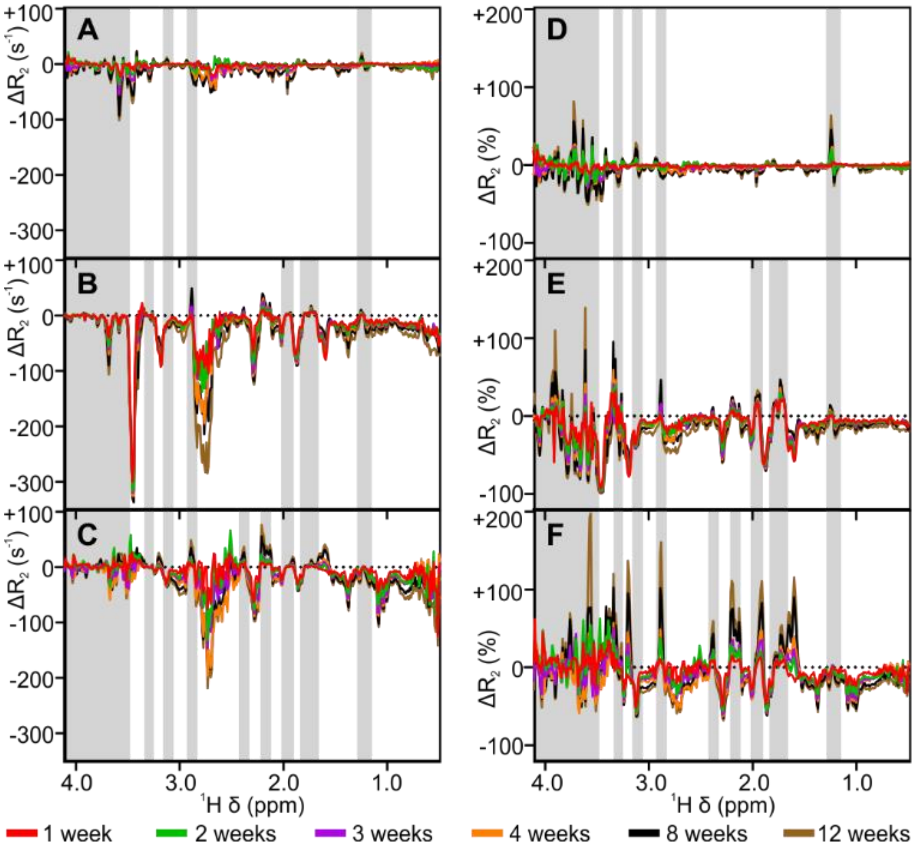

Figure 2-3. Changes in ^1H R_2 during accelerated stability storage. Absolute change (s^{-1}) in R_2 for (**A**) COE-03, (**B**) COE-07, and (**C**) COE-19. Change in R_2 relative to the initial value at time t=0 (%) for (**D**) COE-03, (**E**) COE-07, and (**F**) COE-19. Grey areas highlight regions of spectra containing small molecule signals. Dotted line denotes a baseline with no change.

R_1 values are more complex to interpret than R_2 in terms of molecular tumbling rates, given the V-shaped relationship between τ_c and longitudinal relaxation. Here, all Ab signals exhibit reductions in R_1 rates with time which are fairly linear across the breadth of the Ab NMR spectra (Figure 2-4). Again, COE-07 and COE-19 exhibit larger decreases in relaxation rate than COE-03 for both absolute (Figure 2-4A-C) and relative values (Figure 2-4D-F). Together, both relaxation rates indicate protein degradation for all three Abs, with the observed decreases in R_2 specifically indicating fragmentation occurring in all three Abs. Therefore, for COE-03, the observation of fragmentation based on relaxation rates, yet no net change in 1D spectra, infers that aggregation must also be occurring for this mAb. For COE-07 and COE-19, the NMR observables show the predominant occurrence of fragmentation, but do not rule out aggregation in these two Abs.

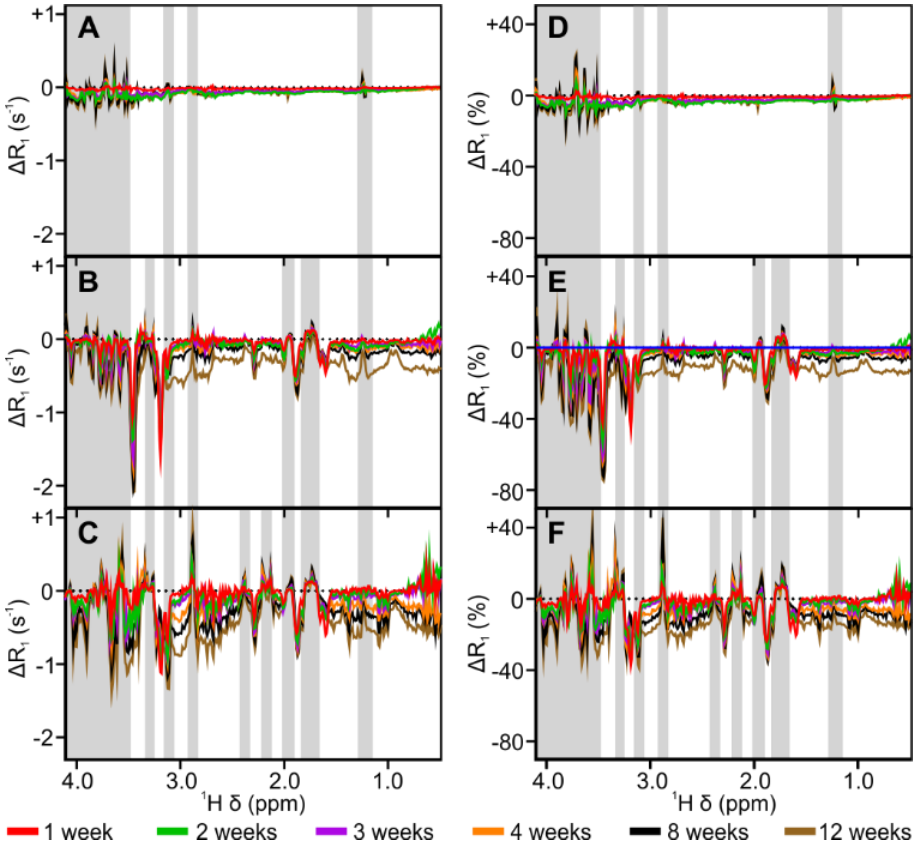

Figure 2-4. Changes in ^{1}H R_1 during accelerated stability storage. Absolute change (s^{-1}) in R_1 for (**A**) COE-03, (**B**) COE-07, and (**C**) COE-19. Change in R_1 relative to the initial value at time t=0 (%) for (**D**) COE-03, (**E**) COE-07, and (**F**) COE-19. Grey areas highlight regions of spectra containing small molecule signals. Dotted line denotes a baseline with no change.

2.4.4 Protein degradation detected by high-performance size exclusion chromatography analysis

To relate NMR observations of Ab stability with standard orthogonal measurements, we analysed the monomer, aggregate, and fragment content using high performance size exclusion chromatography (HPSEC) (see Figure S2-3 for chromatograms) of Ab samples stored in identical formulations under identical conditions (Figure 2-5). All three Abs exhibited both fragmentation and aggregation in a time-dependent manner, with the rates of aggregation and fragmentation slowest for COE-03. Additionally, a lower molecular weight oligomer and a higher initial level of aggregates were detected in COE-19 samples (Figure 2-5D). This concurs with lower observed initial 1D NMR signal intensity for COE-19, with these oligomers expected to contribute less to the observable signal (Figure 2-1). Overall, the NMR observations of protein degradation are in agreement with the HPSEC measurements, with NMR spectra sensitive to protein degradation occurring at a rate of <1% per week.

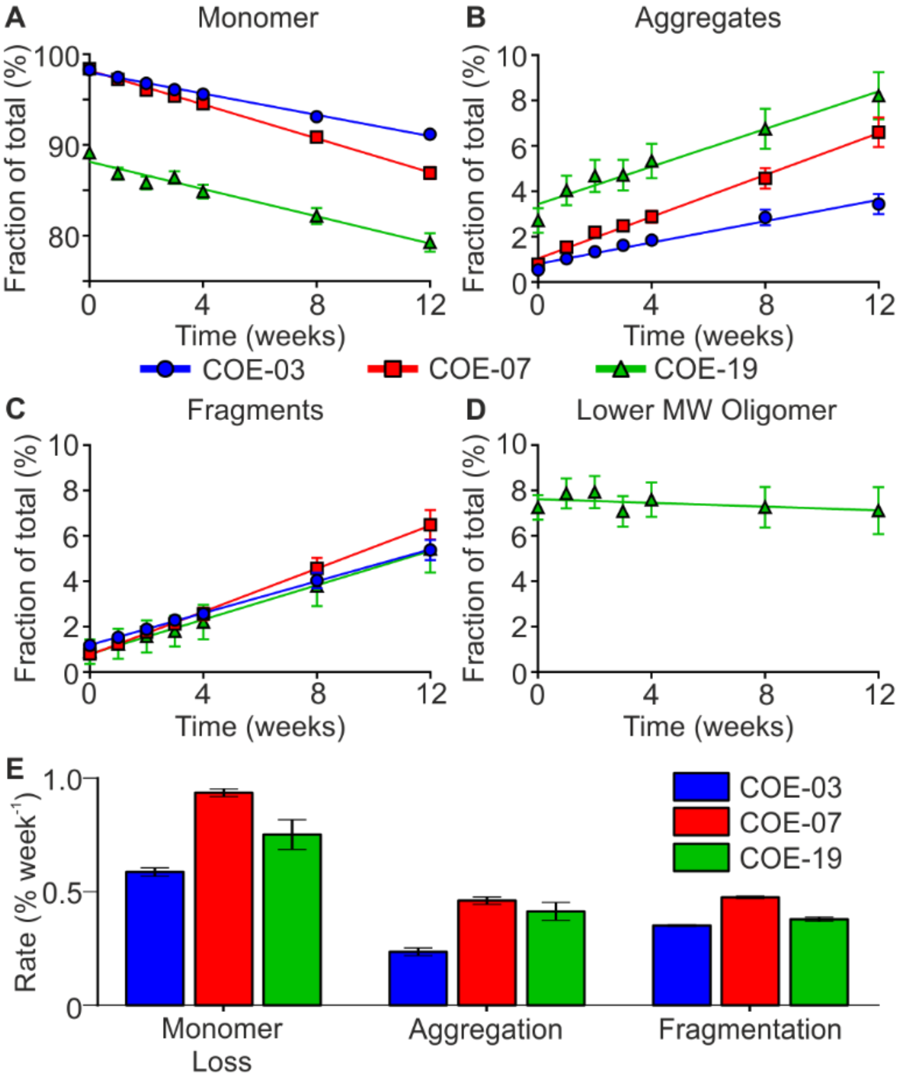

Figure 2-5. Assessment of monomer, aggregate and fragment content by HPSEC. Monomer (A), aggregate (B), and fragment (C) species as a percentage of total observed species (± SD of three replicates). (D) Lower molecular weight oligomer detected in COE-19. Experimental data with linear fit. (E) Rates of monomer loss, aggregation and fragmentation per week, derived from linear fits with 95% confidence intervals.

2.4.5 Small molecule degradation detected by T_2 filtered ^{1}H NMR

Along with stability of the biopharmaceutical protein itself, the stability of small molecule components such as buffers and excipients is critical to the overall formulation. With this in mind, the NMR signals from the residual small molecule components from the original Ab formulations were monitored using T_2 filtered experiments (116 ms filter), which essentially remove signals from the faster relaxing protein. Over time a number of small molecules exhibited changes in NMR signals associated with degradation. In COE-03 and COE-07 samples, sucrose (not present in COE-19) exhibited reduction in glycosyl C1-^{1}H signal intensity, accompanied by appearance and increases in glucose C1-^{1}H signal (Figure 2-6A-B). This degradation was markedly greater in COE-07 than in COE-03 (Figure 2-6C). Notably in COE-07 samples, increases in glucose signal were not proportional with sucrose signal reduction, as would be expected from the breakdown of one sucrose molecule into one molecule of glucose and one molecule of fructose. This indicates further degradation of glucose in COE-07, potentially in the form of glycation of protein molecules.

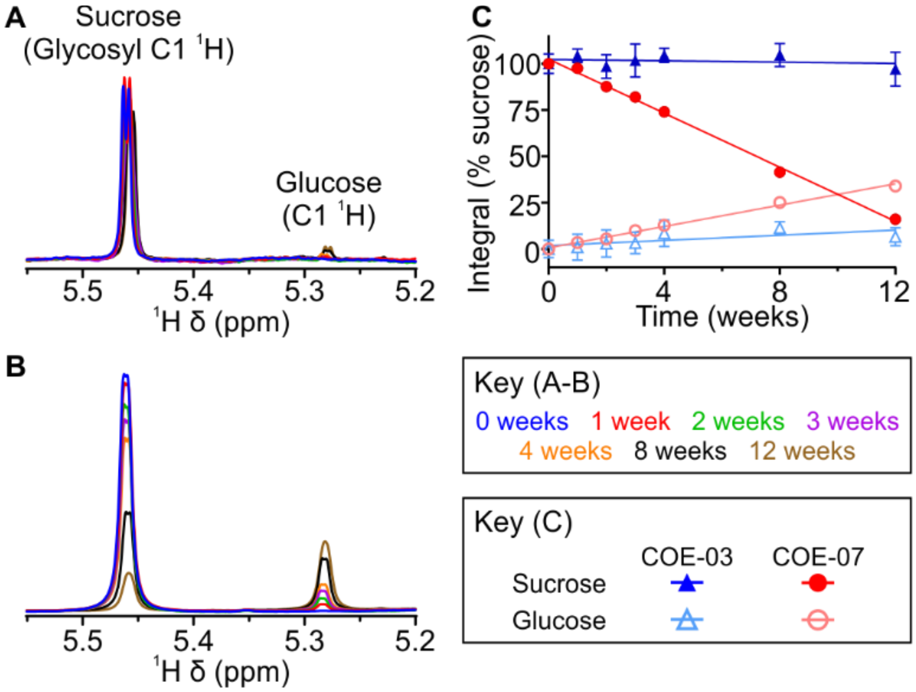

Figure 2-6. Degradation of sucrose detected by ^{1}H NMR spectroscopy. ^{1}H NMR spectra for (**A**) COE-03 and (**B**) COE-07, with sucrose (glycosyl C1-^{1}H) and glucose (C1-^{1}H) at 5.46 and 5.28 ppm, respectively. (**C**) Change in sucrose and glucose integrals (expressed as a percentage of the initial sucrose integral in each Ab sample) over time. Mean ± SD for three replicates, with linear fit.

^{1}H NMR also detected degradation of arginine present in COE-07 and COE-19 formulations (not present in COE-03) (Figure 2-7A-B). Here, reduction in arginine signals was accompanied by the appearance of new upfield resonances, consistent with arginine oxidation [283]. Arginine degradation occurred at similar levels in both Ab solutions. Finally, histidine present in all Ab samples exhibited minor upfield shifts in both imidazole carbon bound protons (Figure 2-7C&D). These signals are sensitive to solution pH as a result of imidazole ring protonation, and as such these changes suggest a slight increase (~0.1 pH units based on calibration curves [284]) in solution pH over the 12 week period. All together the data suggest that comprehensive analysis of even a simple set of NMR spectra, including ^{1}H 1D, supplemented by R_1 and R_2 relaxation profiles and T_2-filtered 1D experiments, can provide a comprehensive assessment of protein formulations, and reveal degradation of both protein and small molecules.

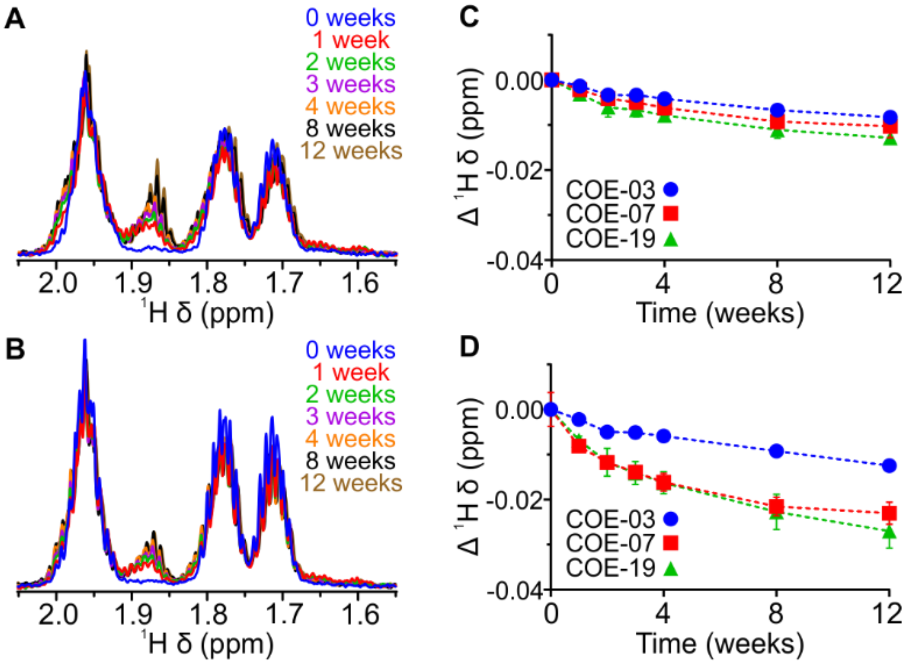

Figure 2-7. Arginine degradation and solution pH changes detected by ^{1}H NMR spectroscopy. ^{1}H NMR spectral region containing arginine signals (C_β- and C_γ-^{1}H's) for (**A**) COE-07 and (**B**) COE-19. Changes (Δ) in ^{1}H chemical shifts for histidine $C_{\delta2}$-^{1}H (**C**) and $C_{\varepsilon1}$-^{1}H (**D**) over the course of the stability study. Mean ± SD for three replicates, with dashed lines as guides only.

2.5 Discussion

Monitoring both small molecule and protein content and stability is vital to the successful optimisation of Ab formulations and achieving a long product shelf-life. However, assessment of formulations typically requires numerous techniques, with separate sample manipulations which may distort the analysis, for example, sample dilution would alter the equilibrium of reversible self-association present in the original formulation. We show here that ^{1}H NMR spectroscopy can be used as an orthogonal technique to simultaneously characterise the content and stability of both protein and small molecule formulation components, perhaps as a triaging approach to inform decisions on which specialised techniques should be employed to quantify or study particular forms of degradation in more detail.

In NMR, initial Ab signal intensity and relaxation rates report on Ab solution behaviour, with molecules exhibiting greater self-association or with oligomer species displaying lower signal intensities and higher relaxation rates (Figure 2-1). Following degradation at 40°C, the observed broad increases in Ab signal intensity with retention of the overall spectral appearance (Figure 2-2) indicate fragmentation in COE-07 and COE-19. This is consistent with previous comparisons of enzymatically digested mAb fragments with intact mAbs by 2D natural abundance NMR [277]. Conversely, 1D spectra may exhibit reductions in intensity if aggregation is dominant [233]. However, as 1D ^{1}H NMR spectra represent a balance between monomers, aggregates and fragments, such spectra coincidentally may be insensitive to degradation if the effects of aggregation and fragmentation on signal intensity cancel each other out (Figure S2-2), as in the case of COE-03 here (Figure 2-2 & Figure 2-5). However, the addition of relaxation rate analysis revealed that fragmentation occurred in COE-03 (Figure 2-3 & Figure 2-4), which, with the observed static 1D spectra, allowed inference of the occurrence of aggregation. For the two other Abs, 1D spectral changes revealed the presence of significant degradation immediately. As protein and small molecule signals are monitored simultaneously, this more detailed approach may be advantageous compared to recently suggested analysis based on the single parameter relaxation rate of the water signal [281, 285]. Our approach could also be extended to study chemical modification of Abs [226, 286] and small molecule formulation components at the same time, alongside Ab degradation.

Small molecules, such as buffers and excipients, are also an integral component of biopharmaceutical formulations, responsible for stabilising and solubilising the therapeutic protein. If they degrade, their stabilising function may be diminished. Most common buffers and excipients contain NMR observable protons [279]. As demonstrated here, ^{1}H NMR is well suited to monitoring the presence and degradation of small molecules, particularly after the application of a T_2 filter to remove fast relaxing protein signals (Figure 2-6). This is particularly applicable to studying the degradation of sacrificial excipients, such as methionine [89, 287] and other antioxidants, which are believed to protect proteins from degradation by undergoing degradation themselves. Additionally, the chemical shift of ionisable species, such as buffer molecules (e.g. histidine here), or spiked into solution as a tracer, can be used as an inbuilt pH meter (Figure 2-7) when compared to a known calibration curve. These assessments of small molecule stability may be coupled with NMR identification of small molecule contaminants or processing impurities [212, 214] to provide an overarching assessment of the small molecule content of solutions throughout the manufacturing process.

2.6 Conclusion

NMR assessment of both protein and small molecule components provides a holistic characterisation of the content and stability of an overall biopharmaceutical formulation. Observation of changes in protein signal intensity or apparent relaxation rates indicate that monomer, aggregate and fragment content should be investigated, for example, by HPSEC or capillary gel electrophoresis (CGE). Changes in excipient signal intensity or chemical shift, or appearance of new signals indicates chemical degradation of small molecules. After detection of degradation of specific small molecules, such as sucrose degradation into glucose observed here, specific protein modifications, such as protein glycation which may impact pharmacokinetics and pharmacodynamics [88, 288], should be investigated. This NMR assessment of small molecule and protein content and stability can be performed *in situ* at high concentration without further sample manipulation, making it a useful orthogonal assessment of overall formulation stability and helping to triage the use of specialised techniques for more detailed characterisation.

2.7 Acknowledgments

J.E.B. was supported by CASE DTP PhD studentship BB/M011208/1 from the UK Biotechnology and Biological Sciences Research Council (BBSRC) in partnership with AstraZeneca UK. We are grateful to Matthew Cliff for NMR facility management and to Grace Haagensen for assistance with HPSEC experiments.

2.8 Supplementary Information

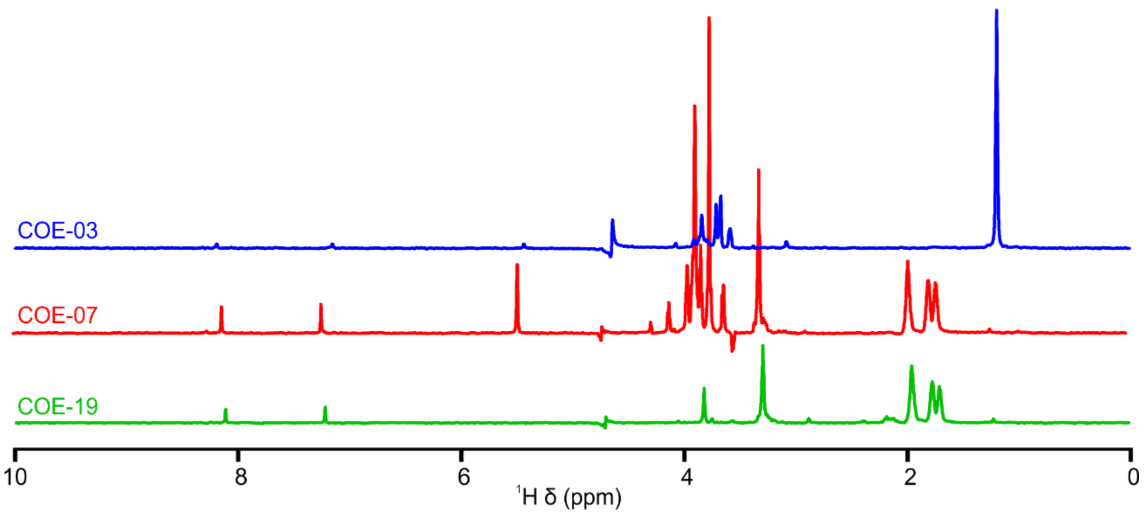

Figure S2-1. T_2-filtered NMR spectra of the three Ab formulations at T=0, highlighting the presence of the small molecule components. A 116 ms T_2 filter was used, corresponding to 32 echoes with 3.2 ms delay. COE-03 (blue), COE-07 (red), and COE-19 (green). All spectra were acquired with the same receiver gain, 24 scans, and for samples with same Ab concentration, and as such the signal intensities reflect the levels of small molecule constituents present in solution after extensive dialysis.

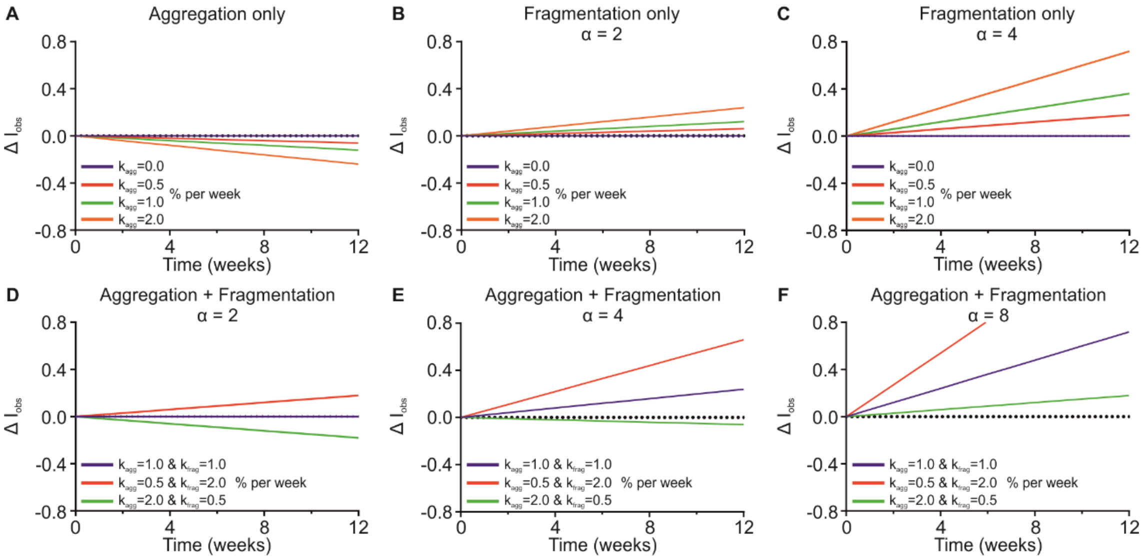

Figure S2-2. Modelling of the effects of aggregation and fragmentation, in isolation and together, on 1D ^{1}H NMR signal intensity. (**A**) Aggregation only and (**B&C**) fragmentation only, with α=2 and α=4, respectively. Combination of aggregation and fragmentation, with (**D**) α=2, (**E**) α=4, and (**F**) α=8. Change in observed signal intensity (ΔI_{obs}) from the initial value modelled against storage time. For an Ab formulation, I_{obs} can be described as:

$$I_{obs} = (P_{mon}\ x\ I_{mon}) + \left(P_{frag}\ x\ I_{frag}\right) + \left(P_{agg}\ x\ I_{agg}\right)$$

where I_{mon}, I_{frag} and I^{agg} are the characteristic signal intensities of monomer, fragment and aggregate species, respectively, for a given protein/solution conditions, and P_{mon}, P_{frag} and P_{agg} are the populations of each species. These populations are time-dependent, with $P_{mon} = P_{\mathrm{mon},0} + k_{mon} \times t$, $P_{frag} = k_{frag} \times t$ and $P_{agg} = k_{agg} \times t$, where k_{mon}, k_{frag} and k_{agg} are the rates (% per week) of monomer loss, and fragmentation and aggregation, respectively; t is time, and $P_{mon,0}$ is the initial population of the monomer. The populations are normalised as: $P_{mon} + P_{frag} + P_{agg} = 1$. For fragments which tumble faster than monomer we assume $I_{frag} = \alpha\ I_{mon}$, where $\alpha>1$ (and may vary between Abs or solution conditions). For large aggregates such as those generated by Abs, we assume $I_{agg} \approx 0$. Although this simple model is clearly underdetermined and does not allow quantitative fitting of experimental parameters, it can be used to illustrate some typical behaviours of this system in different regimes. Aggregation alone (A) results in decreases in signal intensity, whilst fragmentation alone (B&C) results in increases in signal intensity, with the extent of the increase dependent upon the value of α. For systems undergoing both aggregation and fragmentation (D-F), in certain situations there may be no or negligible change in I_{obs} if the effects of aggregation and fragmentation counteract each other.

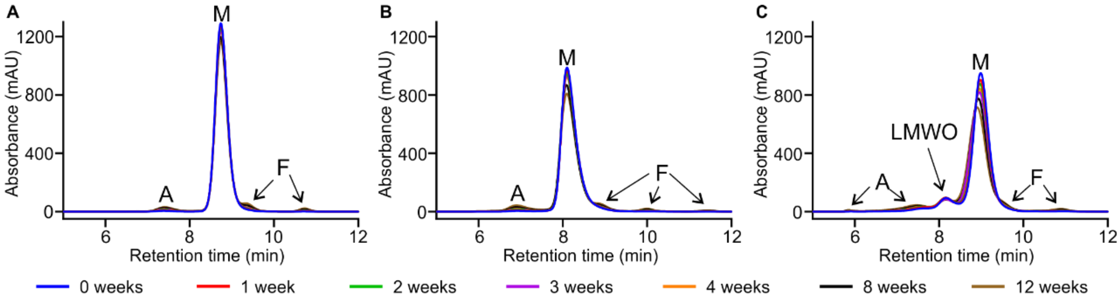

Figure S2-3. HPSEC chromatograms of the three Abs over 12 weeks accelerated stability storage. (**A**) COE-03, (**B**) COE-07, and (**C**) COE-19 chromatograms. Aggregates are marked with ‘A’, monomer peaks with ‘M’, and fragments with ‘F’. The lower molecular weight oligomer species in COE-19 is marked ‘LMWO’

3 Stability of a high-concentration monoclonal antibody solution produced by liquid-liquid phase separation

This chapter was prepared for submission as a research paper:

Jack E. Bramham[1], Stephanie A. Davies[2], Adrian Podmore[2], and Alexander P. Golovanov[1]

[1] Manchester Institute of Biotechnology and School of Chemistry, Faculty of Science and Engineering, The University of Manchester, Manchester, M1 7DN, UK
[2] Dosage Form Design & Development, BioPharmaceuticals Development, R&D, AstraZeneca, Cambridge, CB21 6GH, UK

Author contributions:

J.E.B. performed experiments, analysed the data, and drafted the manuscript. A.P. and S.A.D. supplied the Ab and provided guidance and supervision from an industrial perspective. A.P.G. conceived and supervised the project and provided input regarding data analysis. The manuscript was written through contributions of all authors.

3.1 Abstract

Subcutaneous injection of a low volume (<2 mL) high concentration (>100 mg/mL) formulation is an attractive administration strategy for monoclonal antibodies (mAbs) and other biopharmaceutical proteins. Using concentrated solutions may be also beneficial at various stages of bioprocessing. However, concentrating proteins by conventional techniques, such as ultrafiltration, can be time consuming and challenging. Isolation of the dense fraction produced by macroscopic liquid-liquid phase separation (LLPS) has been suggested as a means to produce high-concentration solutions, but questions arise regarding the practicality of this method, and the stability of the resulting protein solution. In this proof-of-concept study, we demonstrate that LLPS can be used to concentrate a mAb solution to >170 mg/mL. We show that the structure of the mAb is not altered by LLPS, and unperturbed mAb is recoverable following dilution of the dense fraction, as judged by ^{1}H NMR spectroscopy. Finally, we show that the physical properties and stability of a model high concentration protein formulation obtained from the dense fraction can be improved, for example through the addition of the excipient arginine·glutamate. This results in a stable high-concentration protein formulation with reduced viscosity and no further macroscopic LLPS. Concentrating mAb solutions by LLPS represents a simple and effective technique to progress towards producing high-concentration protein formulations for bioprocessing or administration.

3.2 Introduction

Since the introduction of the first protein therapeutic in 1982, biopharmaceutical proteins, such as monoclonal antibodies (mAbs), have developed into major treatments for a wide range of diseases [4, 44, 61]. For the prolonged treatment of chronic conditions, such as arthritis and other autoimmune diseases, subcutaneous injection by the patient themselves represents an attractive administration strategy for mAbs [68, 72]. Due to the limited injection volume (<2 mL) possible into the subcutaneous tissue [75], such strategies require high-concentration protein formulations, with protein concentrations typically greater than 100 mg/mL [76]. Using high-concentrations solutions may also be beneficial during bioprocessing and manufacturing. However, achieving such high concentrations and stabilising the final formulation against degradation remains challenging [289].

During bioprocessing, biopharmaceutical protein solutions are typically concentrated using ultrafiltration techniques involving membranes, such as tangential-flow filtration [64]. However, achievable protein concentrations may be limited, with concentration-induced viscosity, self-association, and aggregation potentially resulting in significant back pressure, membrane fouling and reduced filtration rates [129, 270, 290]. Alternatively, lyophilisation followed by reconstitution in a reduced diluent volume may be used, but this may require significant time for freeze-drying, plus additional reconstitution times [291], or may generate physical instabilities due to the stresses of freeze-drying and reconstitution [292]. Therefore, other methods to concentrate biopharmaceutical proteins are required.

Liquid-liquid phase separation (LLPS) has been suggested as a novel technique to concentrate biopharmaceutical solutions [136, 178, 293]. During macroscopic LLPS, a homogenous medium-concentration protein solution spontaneously separates into an upper low-concentration lean layer and a lower high-concentration dense layer. Whilst LLPS is typically considered an unwanted physical instability in biopharmaceutical solutions [140, 147], selective triggering of LLPS, for example, through addition of salts, or changes in temperature, may be used to concentrate a protein solution. Aqueous two-phase extraction, a similar approach involving polymers to trigger phase partitioning, is already widely used during purification in biotechnology [294-296].

Despite the potential of LLPS as a method to concentrate mAb solutions, phase separation is still largely viewed as an undesired physical instability, and there remain questions about the practicality and suitability of its use. For example, due to the attractive protein-protein interactions required for LLPS, there may be concerns about the promotion of aggregation in the high-concentration dense fraction [121, 267]. Additionally, the dense fraction may be excessively viscous [140, 158] and potentially difficult to handle during bioprocessing or administration. Such concerns are common in the development of any highly-concentrated biopharmaceutical protein formulation, where they are typically alleviated through optimisation of solution conditions, including buffer, pH, ionic strength, and addition of excipients [105, 269, 270]. However, to our knowledge, such a formulation approach has not been trialled for high-concentration dense fractions produced by LLPS.

In this study, we explore how the properties and stability of a high-concentration mAb solution produced by LLPS can be improved through the addition of an excipient, arginine·glutamate (Arg·Glu) [105, 152], to the isolated dense fraction. We demonstrate that LLPS can be used to concentrate a mAb from 80 mg/mL to >170 mg/mL, and show, using ^{1}H nuclear magnetic resonance (NMR) spectroscopy, that structurally unperturbed mAb is recoverable following dilution of the dense fraction. Viscosity measurements and high-performance size exclusion chromatography (HPSEC) analysis shows that Arg·Glu improves the physical properties and stability of a model high-concentration formulation produced from the dense fraction. Controlled LLPS and subsequent addition of excipients offers a simple and effective method to produce stable high-concentration antibody formulations.

.

3.3 Materials and Methods

3.3.1 Sample preparation

A mAb, COE-13 (MW 149 kDa, pI 8.1 – 8.6), known to be prone to LLPS under specific conditions [147], was supplied by AstraZeneca. 20 mM acetate buffer (sodium acetate trihydrate (Sigma-Aldrich) and glacial acetic acid (Fisher Chemical)), pH 5.5, was prepared fresh as required. Concentrated NaCl (Fisher) was also prepared in buffer. Solutions were filtered with 0.2 µm syringe filters (Minisart SFCA, Sartorius) or 0.22 µm membrane filters (GSWP, Merck Millipore). Protein concentrations were determined by absorbance at 280 nm using a NanoDrop One (Thermo Scientific) in triplicates with dilution in buffer as required.

Stock solutions of COE-13 (46 mg/mL) were dialysed in acetate buffer, using GeBAflex-Maxi dialysis tubes (3 ml, MWCO 30 kDa, Generon) or Slide-A-Lyzer MINI dialysis devices (0.5 ml, MWCO 20 kDa, Thermo Scientific) for large and small volumes, respectively. Extensive buffer exchange was conducted over five days. Samples not to undergo LLPS were subsequently prepared by dilution with additional buffer and concentrated NaCl to lean phase protein (10 mg/mL) and NaCl concentration (75 mM). Samples to undergo LLPS were initially concentrated using a centrifugal concentrator (30 kDa MWCO, Amicon) to >90 mg/mL, with subsequent dilution with buffer and concentrated NaCl to 80 mg/mL protein concentration and 75 mM NaCl. Macroscopic LLPS was induced by incubation at 4°C for 24 hours.

Solution	**Volume (µL)**	**Concentration (mg/mL)**	
		Measured	**Calculated**
Before LLPS	545	80 ± 0.9	-
Extracted lean fraction	300	10 ± 0.3	-
Dense layer with residual lean fraction	245	-	165 ± 0.4
Dense fraction	230	171 ± 55	175 ± 5

Table 3-1. Volumes and protein concentrations of the various solutions obtained during LLPS experiments. Measured concentrations determined by absorbance at 280 nm following appropriate dilution. High variability in measured dense fraction concentration caused by difficulties in handling such a viscous solution. Calculated concentrations were determined based on measured solution volumes (second column), and the measured concentration of the lean fraction.

Following LLPS, the fractions were separated by removal of the lean fraction (Table 3-1). To generate two model high concentration formulations, the remaining dense fraction (with a small residual amount of lean fraction) was brought to 20°C, remixed and supplemented with 0.02 % (w/v) sodium azide (Sigma-Aldrich) to inhibit bacterial growth. A 100 mM Arg·Glu (final concentration) formulation was generated by addition of concentrated Arg·Glu (equimolar L-arginine and L-glutamic acid mixture, both Sigma-Aldrich) dissolved in buffer supplemented with 75 mM NaCl, while a reference formulation was generated by addition of an equivalent volume of buffer with 75 mM NaCl. Aliquots of the model formulations were then stored under either refrigerated (4°C) or stressed stability (40°C) conditions. The sample aliquots were frozen after 0, 7, 14, or 28 days for further analysis.

3.3.2 NMR spectroscopy

NMR experiments were acquired using a Bruker 800 MHz Avance III spectrometer equipped with 5 mm TCI cryoprobe and variable temperature control unit. Sample temperature was calibrated against a standard methanol sample and verified with an external thermocouple placed in a sample tube in the probe. NMR samples (400 µL) were prepared in 5 mm NMR tubes (541-PP-7, Wilmad) with a coaxial insert (50 mm stem, Wilmad) filled with ^2H_2O to provide for external lock without sample adulteration. For variable temperature experiments, samples were left to equilibrate for 30 minutes upon reaching the desired temperature, with automated tuning, shimming and pulse calibration conducted following equilibration. For NMR analysis of mAbs after LLPS, lean fractions were assessed neat, whilst dense fractions were assessed neat or after dilution to lean phase concentration (10 mg/mL) with buffer containing 75 mM NaCl.

1D ^1H spectra were recorded using excitation sculpting water suppression (Bruker pulse program *zgesgp*). Apparent transverse relaxation rates (R_2) were measured using a Carr-Purcell-Meiboom-Gill (CPMG) pulse sequence, with temperature compensation and a fixed echo time of 2.8 ms. Spectra were processed and analysed with TopSpin 4.0 (Bruker). Apparent R_2 at spectral points (0.05 ppm intervals) across the spectral width were calculated in Dynamics Center 2.6.1 (Bruker). Processed data were plotted in GraphPad Prism 8.0.

3.3.3 High-performance size exclusion chromatography

Analysis of mAb monomeric, aggregate, and fragment species was performed using high-performance size exclusion liquid chromatography (HPSEC), with a Agilent 1200 series HPLC system with a TSKgel SW_{XL} column (30 cm x 7.8 mm, 5 µm particle size, Tosoh Bioscience). Model formulations were diluted to 10 mg/mL and 0.45µm filtered prior to analysis, Ultrafree-MC-HV, Merck Millipore). A 25 µL injection volume was used, with the system run at 1.0 mL/min with a mobile phase of 0.1 M Na_2HPO_4, 0.1M Na_2SO_4, pH 6.8. Absorbance wavelength for detection was set at 280 nm. Chromatograms were analysed in ChemStation (Agilent).

3.3.4 Viscosity measurements

Dynamic viscosities of the model formulations were measured at different temperatures using a VROC initium (Rheosense) with a B05 VROC cell and Peltier temperature control. Viscosities were measured according to the manufacturer's instructions at a controlled shear rate of 345 s^{-1}, with three repeated measurements per temperature. Samples were equilibrated for two minutes prior to analysis. Cleaning was conducted between samples with 1% Aquet detergent (Bel-Art), isopropyl alcohol, and filtered air.

3.4 Results

3.4.1 Using LLPS to concentrate mAb solutions

To demonstrate the use of LLPS to concentrate a mAb, LLPS was triggered in 80 mg/ml COE-13 in 20 mM acetate buffer, pH 5.5, by addition of 75 mM NaCl and incubation at 4°C (Figure 3-1). The initially opalescent solutions underwent rapid macroscopic LLPS, with two layers visible after 20 min, and the boundary between these layers sharpening over time. After 24 hours, the upper lean and lower dense fractions were isolated. Protein concentration measurements showed that LLPS resulted in a >2-fold increase in concentration in the dense layer (171 mg/mL) compared to the initial solution, while the lean fraction concentration was 10 mg/mL.

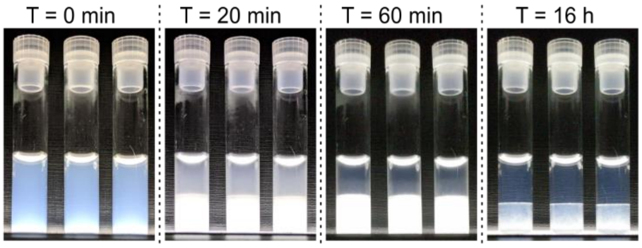

Figure 3-1. LLPS of COE-13 triggered by incubation at 4°C. Triplicate solutions illuminated from underneath to visualise light scattering and opalescence. Images taken at 4°C after the incubation times indicated. Beyond 20 minutes, the visible bottom layer corresponds to the dense fraction, and upper layer to the lean fraction.

To investigate whether LLPS resulted in any aberrant irreversible changes in mAb structure and behaviour, ^{1}H NMR spectra and transverse relaxation rate (R_2) profiles were recorded for the lean fraction, and the dense fraction before and after dilution with buffer (containing 75 mM NaCl to maintain ionic strength). Additionally, spectra were recorded for a dilute COE-13 solution which had not undergone LLPS. All samples were in equivalent buffers (20 mM acetate, pH 5.5, with 75 mM NaCl), with 10 mg/mL COE-13, apart from the intact dense fraction, where protein concentration was significantly higher (171 mg/mL). ^{1}H NMR spectral fingerprints of the characteristic methyl region (Figure 3-2A) report on the apparent structure and colloidal behaviour of mAbs [233]. The lean fraction (green) and the diluted dense fraction (purple) exhibited very similar NMR spectra to the COE-13 solution which had not undergone LLPS (blue), indicating that the protein in these solutions has very similar higher order structure. NMR spectra of the neat dense fraction had significantly lower signal intensity than the other solutions, despite a 17-fold higher protein concentration, in agreement with our previous observations [147].

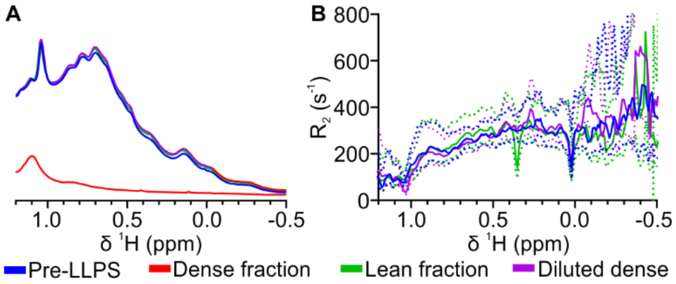

Figure 3-2. NMR comparison of mAb structure and colloidal behaviour before and after LLPS. (**A**) 1D ^{1}H NMR spectra and (**B**) R_2 profiles comparing a non-phase separated protein solution, the intact lean fraction, and diluted dense fraction (all 10 mg/mL), with the intact dense fraction collected after LLPS (171 mg/mL). All solutions were in 20 mM acetate buffer, pH 5.5, with 75 mM NaCl. Dense fraction not shown on R_2 profile due to rapid R_2 rate and poor signal in CPMG experiments. Dotted lines indicate the respective 95% confidence bounds of the fitted relaxation rates.

NMR transverse relaxation rates (R_2) are coupled to molecular motions and apparent molecular size through rotational correlation time, and so report on apparent intermolecular interactions. The similar R_2 spectral profiles (Figure 3-2B) between the three 10 mg/mL solutions show that protein-protein interactions and colloidal behaviour of COE-13 are not irreversibly perturbed by LLPS. Conversely, R_2 was markedly faster in the intact dense fraction, such that COE-13 relaxation rates were essentially unmeasurable in this fraction. Along with the significantly reduced signal, this suggests significant attractive protein-protein interactions and the occurrence of protein self-association and high viscosity in the highly-concentrated dense fraction. On the other hand, the NMR observations indicate that unperturbed COE-13 is recoverable from the lean fraction and after dilution of the dense fraction, suggesting that the self-association observed in the dense fraction is fully reversible.

3.4.2 Production of model high-concentration formulations from the dense fraction

Whilst the neat dense fraction produced by LLPS may in principle have a satisfactorily high protein concentration, its properties, such as viscosity, self-association and protein stability, may render it unsuitable for bioprocessing, storage and administration. In our NMR assessments (Figure 3-2) we observed clear evidence of significant protein self-association, likely as a result of attractive protein-protein interactions. To understand if this self-association could be reduced while maintaining this high concentration, we next investigated whether the addition of an excipient, arginine·glutamate (Arg·Glu), could improve the properties of the mAb solution obtained from the dense fraction and shift the self-association equilibrium towards a monomeric, non-associated state. Two model high-concentration protein formulations were generated from the isolated dense fractions: a formulation with 100 mM Arg·Glu (final concentration), and a reference formulation without Arg·Glu. Final protein concentration in both formulations was 148 mg/mL, while final buffer and NaCl concentrations were identical to the starting solutions, at 20 and 75 mM, respectively. These model formulations were used for further comparative analysis.

3.4.3 Arg·Glu improves the stability of model formulations derived from the dense fraction

LLPS is typically considered an unwanted physical instability, and there therefore may be concerns that proteins which have undergone LLPS may be inherently prone to further aggregation and degradation. To investigate this behaviour, the physical and chemical stability of the model high-concentration formulations generated from the phase-separated dense fraction was examined by storage at standard refrigerated conditions (4°C) or under stressed degradation conditions (40°C) for 4 weeks.

The behaviour of the two model COE-13 formulations during storage was markedly different (Figure 3-3). The reference formulation underwent LLPS again following storage at 4°C (Figure 3-3, right-hand side), with re-establishment of the LLPS equilibrium concentrations. Conversely, the formulation with 100 mM Arg·Glu remained as a single homogenous solution, with Arg·Glu preventing further LLPS at 4°C. Both formulations exhibited no LLPS when incubated at 40°C, above the apparent critical temperature (T_C) for this system (~13°C).

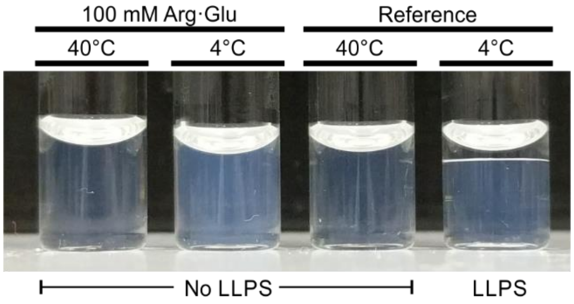

Figure 3-3. Behaviour of the model formulations after 24 hours incubation at 4 or 40°C. Image taken at ambient room temperature immediately after removal from incubation. Macroscopic LLPS present in the reference formulation stored at 4°C (right-hand side).

Antibody degradation by fragmentation and aggregation during storage was assessed using high performance size-exclusion chromatography (HPSEC) (Figure 3-4). When stored at 4°C, both model high-concentration formulations exhibited no additional degradation after 28 days storage. This demonstrates that the protein solutions concentrated by LLPS are not inherently unstable or prone to degradation during storage at lower temperature. Meanwhile, model formulations stored under stressed degradation conditions at 40°C exhibited both aggregation and fragmentation (Figure 3-4A-C). However, the formulation with 100 mM Arg·Glu was more stable than the reference formulation, with Arg·Glu reducing the rate of antibody aggregation two-fold, whilst also marginally reducing the rate of fragmentation (Table 3-2). This illustrates that excipients, such as Arg·Glu, can improve the stability of high concentration protein solutions generated by LLPS against degradation.

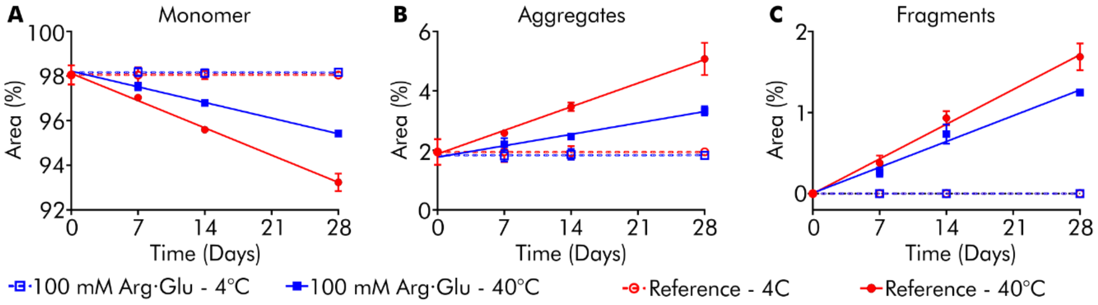

Figure 3-4. Monomer loss, aggregation and fragmentation of model formulations following storage at 4 or 40°C. Monomer (**A**), aggregate (**B**) and fragment (**C**) content for COE-13 formulations over 4 week storage.

Model formulation	Monomer loss (%/month)	Aggregation (%/month)	Fragmentation (%/month)
Reference	5.31 ± 0.18	3.45 ± 0.12	1.86 ± 0.10
With 100 mM Arg·Glu	3.04 ± 0.05	1.67 ± 0.18	1.38 ± 0.23

Table 3-2. Rates of degradation (± standard errors) for the model formulations stored at 40°C. Rates based on linear regression of HPLC data.

Next, the temperature dependence of the dynamic viscosities of the model high-concentration formulations produced by LLPS was explored (Figure 3-5). High viscosity resulting from protein self-association at high protein concentration (e.g. 148 mg/mL here) may pose handling challenges during biopharmaceutical fill-finish and administration, and therefore formulation viscosity should be monitored and minimised. The reference model formulation was particularly viscous, with its viscosity exceeding 200 mPa·s at temperatures below 25°C. Such a high viscosity for a mAb formulation renders it largely unsuitable for processing and syringing, i.e. for subcutaneous administration. Conversely, the model formulation with 100 mM Arg·Glu exhibited significantly lower viscosity, ranging from 12 to 113 mPa·s across the explored temperature window (37°C to 5°C). At ambient room temperature and above, this formulation would likely be syringeable, with viscosity beneath the apparent limit of syringeability (50 mPa·s) [128]. Viscosity of the samples stored at 4 and 40°C for 28 days were not significantly different, indicating that the aggregation and fragmentation observed following storage at 40°C (Figure 3-4) did not have a significant effect on the viscosity of either formulation. Both model formulations follow the expected exponential temperature dependent viscosity relationship, with viscosity reduced at higher temperatures. In conclusion, this study shows that LLPS can yield high-concertation mAb formulation with satisfactory stability, viscosity and syringeability properties, by adding a suitable excipient to the dense fraction.

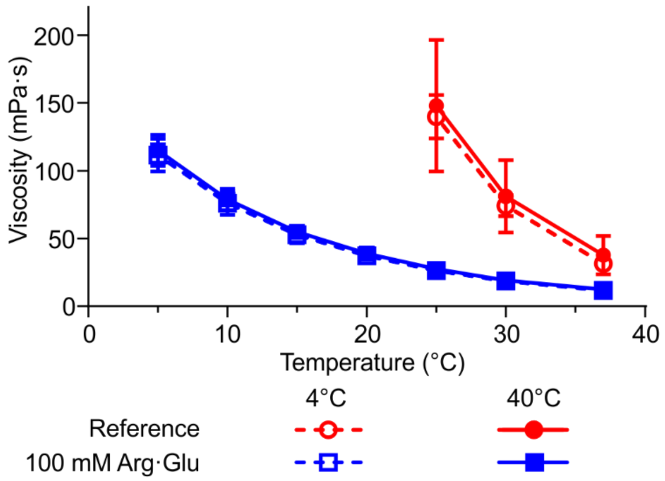

Figure 3-5. Viscosity of the model high-concentration formulations across a range of temperatures after 28 days storage at either 4 or 40°C. Mean ± standard deviation of three replicate measurements. For the reference formulation, the viscosity of solutions below 25°C exceeded the measurement capacity of the specific VROC Initium chip (~200 mPa·s).

3.5 Discussion

Obtaining stable high-concentration antibody formulations is critical to the development of subcutaneous injections as a viable means of biopharmaceutical administration. However, concentrating some biopharmaceutical protein solutions beyond >100 mg/mL and stabilising these solutions against self-association and degradation may be challenging. In this proof-of-principle study, we demonstrate that LLPS can be harnessed to generate high-concentration antibody solutions without adversely affecting higher-order protein structure, and that the addition of excipients improves the properties (e.g., viscosity, aggregation state and storage stability) of model formulations generated from the resulting dense fraction.

Here, LLPS was triggered in 80 mg/ml COE-13 in a formulation containing 75 mM NaCl by incubation at 4°C (Figure 3-1). This lead to a greater than two-fold spontaneous increase in protein concentration to 175 mg/mL in the dense fraction, with such a concentration, in principle, suitable for subcutaneous administration [76]. Although LLPS was relatively fast, the speed of macroscopic layer separation following LLPS, and thus the speed of concentrating of the protein solution, may be improved further through centrifugation of the solution during the process [297]. Whilst the conditions used here to trigger LLPS of COE-13 were previously identified [147], for other mAbs a formulation screening approach may be set up using conventional high-throughput platforms, but aiming to determine phase-separation conditions instead. A variety of additives, salts, polyethylene glycol (PEG), polyvalent ions or other suitable molecules, as well as environmental conditions like temperature, can be used to induce LLPS [144, 171, 174]. After the dense phase is separated, conventional formulation screening [150, 298] could be used to establish which excipients are able to prevent further phase separation, reduce self-association and solution viscosity, and achieve long-term storage stability.

NMR spectroscopy is increasingly used as a fingerprinting tool to assess the higher-order structure of biopharmaceutical proteins [218, 222, 278]. Here, ^{1}H NMR spectra showed that COE-13 in both the dense and lean fractions is not irreversibly affected by the process of LLPS, with the lean fraction and diluted dense fraction displaying similar fingerprint 1D spectra and transverse relaxation rate profiles to protein which had not undergone LLPS. Additionally, as protein in the lean fraction was shown to be structurally unperturbed following LLPS, this suggests that this extracted fraction may be recycled through conventional concentrating techniques, and then phase separated to produce further dense fraction, thus increasing yield and reducing waste.

While LLPS may be used to concentrate protein solutions, the attractive protein interactions which drive phase separation, may in principle result in solutions with properties unsuitable for further handling during processing and administration. Moreover, recovery and dilution of this dense fraction may trigger further LLPS, which is undesirable in any final formulation. Here, we show that addition of an excipient, such as Arg·Glu, to the isolated dense fraction improves the properties of model high-concentration formulations generated from the dense fraction. As previously observed with other protein solutions [154, 299], Arg·Glu reduced the viscosity of the model formulation (Figure 3-4). Importantly, Arg·Glu also prevented further LLPS of the model formulation (Figure 3-3). Furthermore, the high concentration antibody solutions generated here by LLPS were shown to not be inherently unstable when stored under typical refrigerated conditions, with Arg·Glu reducing both aggregation and fragmentation of the model formulations stored at 40°C to a level typical for other mAb formulations [105, 300]. Overall, the LLPS ‘history’ of the concentrated mAb sample did not result in any additional instabilities, and we conclude that typical formulation optimisation approaches applied to a separated dense fraction should yield a stable high concentration protein formulation.

3.6 Acknowledgments

J.E.B. was supported by CASE DTP PhD studentship BB/M011208/1 from the UK Biotechnology and Biological Sciences Research Council (BBSRC) in partnership with AstraZeneca UK. We are grateful to Matthew Cliff for NMR facility management, to Grace Haagensen for assistance with HPSEC experiments, and to Leanne Amery for assistance with viscosity measurements.

4 ^{19}F Dark-state Exchange Saturation Transfer NMR reveals reversible formation of protein-specific large clusters in high-concentration protein mixtures

This chapter was written, peer-reviewed and published as:

John M. Edwards[1†], Jack E. Bramham[1†], Adrian Podmore[2], Seven M. Bishop[3], Christopher F. van der Walle[2], and Alexander P. Golovanov[1], ^{19}F Dark-state Exchange Saturation Transfer NMR reveals reversible formation of protein-specific large clusters in high-concentration protein mixtures, *Analytical Chemistry*, **2019** 91(7):4702-4708, doi: https://doi.org/10.1021/acs.analchem.9b00143

[1] Manchester Institute of Biotechnology and School of Chemistry, Faculty of Science and Engineering, The University of Manchester, Manchester, M1 7DN, UK
[2] Dosage Form Design & Development, BioPharmaceuticals Development, R&D, AstraZeneca, Cambridge, CB21 6GH, UK
[†] Shared first authorship

Author contributions:

J.M.E. and J.E.B. contributed equally. J.M.E. prepared samples, performed experiments, analysed the data, and drafted the manuscript. J.E.B. performed experimental set-up, created data analysis scripts, analysed the data, and drafted the manuscript. A.P., S.M.B. and C.v.d.W. supplied the Abs and provided guidance and supervision from an industrial perspective. A.P.G. conceived and supervised the project and provided input regarding data analysis. The manuscript was written through contributions of all authors. All authors have given approval to the final version of the manuscript.

4.1 Abstract

Proteins frequently exist as high-concentration mixtures, both in biological environments and increasingly in biopharmaceutical co-formulations. Such crowded conditions promote protein–protein interactions, potentially leading to formation of protein clusters, aggregation and phase separation. Characterising these interactions and processes *in situ* in high-concentration mixtures is challenging due to the complexity and heterogeneity of such systems. Here we demonstrate the application of the dark-state exchange saturation transfer (DEST) NMR technique to a mixture of two differentially ^{19}F-labeled 145 kDa monoclonal antibodies (mAbs) to assess reversible temperature-dependent formation of small and large protein-specific clusters at concentrations up to 400 mg/mL. ^{19}F DEST allowed quantitative protein-specific characterisation of the cluster populations and sizes for both mAbs in the mixture under a range of conditions. Additives such as arginine glutamate and NaCl also had protein-specific effects on the dark-state populations and cluster characteristics. Notably, both mAbs appear to largely exist as separate self-associated clusters, which mechanistically respond differently to changes in solution conditions. We show that for mixtures of differentially ^{19}F-labeled proteins DEST NMR can characterise clustering in a protein-specific manner, offering unique tracking of clustering pathways and a means to understand and control them.

4.2 Introduction

Proteins in biological environments are often part of complex mixtures at high concentration. Such conditions lead to macromolecular crowding and increased protein–protein interactions, which may be involved in normal or aberrant biological processes [182, 301, 302]. Understanding molecular mechanisms of protein-specific clustering is needed in diverse areas of science ranging from biopharmaceutical development to cell biology and biotechnology. For example, in biopharmaceuticals such as monoclonal antibodies (mAbs), which constitute a large and rapidly growing section of the pharmaceutical market [303, 304], there is considerable interest in formulating at high concentrations (≥100 mg/mL) [76, 305, 306] and/or as co-formulations of two or more proteins [307, 308]. However, high concentrations may promote formation of reversible and irreversible oligomers, aggregates, and clusters [119, 197, 309].

Assessing protein stability and interactions *in situ* in high-concentration mixtures is non-trivial for both biopharmaceutical formulations [270, 310] and biological mixtures. Standard biophysical techniques, such as dynamic or static light scattering (DLS or SLS) and analytical ultracentrifugation (AUC), often do not permit measurements at such high concentrations [311]. Characterisation becomes even more challenging for mixtures and co-formulations, where proteins mixed together may undergo both self- and cross-interactions [307, 308].

Extrinsic differential labelling of proteins with ^{19}F tags was recently suggested for monitoring the behaviour of individual mAbs in high-concentration mixtures *in situ* by ^{19}F NMR, using diffusion ordered spectroscopy (DOSY) and relaxation experiments [234]. Proteins can be labelled using a variety of ^{19}F tags [312], with even proteins as large as mAbs giving rise to strong, well-resolved signals in the ^{19}F spectrum [234].

Increases in protein concentration in solution do not always result in a concomitant increase in NMR signal intensity. This situation has been explained by concentration-dependent self-association, with consequential increase of protein oligomer size and so broadening of its signals [147, 233, 234]. Large self-associated species undergo such rapid transverse relaxation that they are no longer visible in a conventional NMR spectrum, and so can be described as existing in an NMR-invisible “dark state”. The size and populations of these dark-state species under various conditions may be used for understanding molecular mechanisms of cluster formation [119]: for biopharmaceuticals, for example, these would serve as useful criteria for designing successful formulations which minimise aggregate formation.

One NMR technique used to study dark states is dark-state exchange saturation transfer (DEST) [251, 252, 313].This technique exploits the principle that the rapid transverse relaxation rates of the NMR dark state results in very broad NMR signals. Therefore, selective radiofrequency saturation applied offset from the visible NMR signal will saturate only the dark state. However, if the dark state undergoes exchange with the observable monomer or lower-oligomer species, saturation will transfer to the NMR visible state, leading to signal attenuation. Mapping of this signal attenuation at numerous offsets allows quantitative characterisation of the dark state [252, 313].

DEST is typically conducted on ^{15}N or ^{13}C nuclei in isotopically labelled proteins [251, 252, 313], but such labelling is impractical for mAbs produced in mammalian cells on an industrial scale [207] and not possible for proteins purified from biological samples. ^{1}H DEST on unlabelled proteins is hindered by spin diffusion, complicating quantitative analysis [251].

Here we demonstrate that the DEST technique can be applied to proteins as large as 145 kDa mAbs in mixtures if they are labelled extrinsically with ^{19}F tags. We investigate by ^{19}F DEST and other NMR techniques a co-formulation of two differentially ^{19}F-labeled mAbs known to associate reversibly at high concentrations under a range of conditions, including variable temperature and concentration, and in the presence of excipients. We show that ^{19}F DEST enables us to quantify formation of individual types of protein clusters co-existing in highly concentrated mixtures, providing a measurable parameter to understand the mechanism of protein-specific cluster formation and the potential ability to control the size distribution and concentration of clusters using various additives.

4.3 Materials and Methods

4.3.1 ^{19}F Labelling

The monoclonal IgG antibody samples (mAb2, MW = 144.8 kDa, pI = 8.44 and COE-19, MW 148 kDa, pI = 7.4) used in this study were supplied by MedImmune Ltd., Cambridge, UK, and have previously been described [105, 234]. Two ^{19}F labels were used here: TFBPD (1-(4-(trifluoromethyl)benzyl)-1H-pyrrole-2,5-dione), which was custom synthesised by Charnwood Molecular Ltd., Loughborough, UK, and TFCS (N-(ε-trifluoroacetylcaproyloxy)succinimide ester) [314, 315] supplied by Fisher Scientific, Cat. no. 22299. The mAbs were diluted from a supplied concentration of 45 mg/mL in citrate buffer to 5 mg/mL by addition of pH 7.2 100 mM sodium phosphate buffer. TFBPD and TFCS labelling was carried out following the previously reported procedure for these mAbs [234], with overall labelling efficiencies varying batch-to-batch between 100% and 200% (i.e., an average of 1–2 tags per protein molecule). Protein concentrations were measured based on optical density (OD) at 280 nm (extinction coefficients of mAb2 and COE-19 are 1.435 and 1.780 mL mg^{-1}cm^{-1}, respectively). For extremely high (400 mg/mL) mAb concentrations, samples were diluted prior to OD measurement.

4.3.2 NMR experimental details

NMR experiments were carried out on a Bruker 500 MHz Avance III spectrometer using a QCI-F cryoprobe with cooled ^{1}H and ^{19}F channels and sample temperature control unit. The NMR buffer used throughout was 100 mM pH 5.5 sodium acetate buffer with 10% (v/v) D_2O. Spectra were processed and analysed using Topspin 2.5 and Dynamics Centre 2.4.8.

DEST experiments were conducted with continuous-wave (CW) saturation of 1.0 s duration at three (50, 100, and 200 Hz) saturation field strengths (γB1) for simultaneous fitting. DEST experiments were conducted as pseudo-2D experiments, with CW saturation applied at 31 offset frequencies between −50 and +50 kHz from the frequency carrier position set at the observable ^{19}F signal.

Longitudinal relaxation times (T_1) for ^{19}F were measured using a standard Bruker inversion recovery sequence (*t1ir*). Translational diffusion coefficients (D_L) were collected using diffusion ordered spectroscopy (DOSY) by stimulated echo- pulsed-field gradient pulse program stebpgp1s19 from Bruker's standard library adapted for ^{19}F. The diffusion time (Δ) and the gradient length (δ) were set to 200 and 2 ms, respectively.

^{19}F transverse relaxation rates (R_2) were measured using a combination of modified Bruker Carr–Purcell–Meiboom–Gill (CPMG) sequences [316]. Examples of decay curves from these experiments are shown in Figure S4-1.

4.3.3 DEST data fitting and protein cluster size analysis

Experimental DEST profiles [252] were fitted to a two-state model describing exchange between an NMR-visible state A (reporting on monomeric or lower-oligomeric species) and an NMR-invisible dark state B (reporting on large protein clusters):

$$\underset{(NMR\ visible)}{A} \underset{k_{BA}}{\overset{k_{AB}^{app}}{\rightleftharpoons}} \underset{(dark\ state)}{B}$$

where k_{AB}^{app} is the apparent on rate and k_{BA} is the off rate [251, 252, 313]. The DEST effect for this two-state system was modelled using an homogeneous form of the Bloch–McConnell equations [253] in MATLAB, as shown in the

$$\frac{d}{dt}\begin{bmatrix} E/2 \\ I_x^A \\ I_y^A \\ I_z^A \\ I_x^B \\ I_y^B \\ I_z^B \end{bmatrix} = -\begin{bmatrix} 0 & 0 & 0 & 0 & 0 & 0 & 0 \\ 0 & R_2^A + k_{AB}^{app} & \Omega^A & -\omega_y & -k_{BA} & 0 & 0 \\ 0 & -\Omega^A & R_2^A + k_{AB}^{app} & \omega_x & 0 & -k_{BA} & 0 \\ -2\theta^A & \omega_y & -\omega_x & R_1^A + k_{AB}^{app} & 0 & 0 & -k_{BA} \\ 0 & -k_{AB}^{app} & 0 & 0 & R_2^B + k_{BA} & \Omega^B & -\omega_y \\ 0 & 0 & -k_{AB}^{app} & 0 & -\Omega^B & R_2^B + k_{BA} & \omega_x \\ -2\theta^B & 0 & 0 & -k_{AB}^{app} & \omega_y & -\omega_x & R_1^B + k_{BA} \end{bmatrix} \times \begin{bmatrix} E/2 \\ I_x^A \\ I_y^A \\ I_z^A \\ I_x^B \\ I_y^B \\ I_z^B \end{bmatrix}$$

Figure S4-2, taking into account lifetime line broadening derived from relaxation rate R_2^{obs} measured at each condition, following the well-established protocols [251, 252, 313]. The analysis reveals the fractions and relaxation rates of the visible monomeric and dark states present in solution ($P^A = P^{vis}$ and $P^B = P^{dark}$, and R_2^A and R_2^B, respectively), as well as k_{AB}^{app} and k_{BA} rates for each protein separately.

For variable temperature DEST analysis, first the transverse relaxation rates of the reference monomeric species R_2^{rm} were measured at 313 K in diluted samples (<5 mg/mL) of isolated proteins (3.47 ± 0.27, 38.6 ± 0.03, 3.66 ± 0.29, and 46.5 ± 0.02 s^{-1} for mAb2-TFCS, mAb2-TFBPD, COE-19-TFCS, and COE-19-TFBPD, respectively). Control DEST experiments for these samples did not reveal any measurable dark-state populations. R_2 is proportional to the rotational correlation time τ_C of a particle with effective radius r_{eff}, calculated according to Stokes's equation:

$$R_2 \propto \tau_C = \frac{4\pi\eta(r_{eff})^3}{3kT} \qquad \text{(Equation 4.1)}$$

where k is the Boltzmann constant, η is viscosity, and T is absolute temperature. The values of $R_2^A = R_2^{mon}$ at lower temperature were re-calculated to compensate for slowing molecular tumbling and increased water viscosity [317] as:

$$R_2^A = R_2^{mon}\frac{\eta_T\, T_{ref}}{\eta_{ref}\, T} \qquad \text{(Equation 4.2)}$$

where η_T and η_{ref} are the viscosities of water at temperature T and reference temperature $T_{ref} = 313\ K$, respectively. The effective radius of dark-state clusters $r_{eff}^{cluster}$ at temperature T was derived from the apparent relaxation of dark state B ($R_2^B(T) = R_2^{dark}(T)$) as:

$$r_{eff}^{cluster} = \sqrt{\frac{R_2^{dark}(T)}{R_2^{mon}(T)}}\, r^{mon} \qquad \text{(Equation 4.3)}$$

where r^{mon} is the radius of the monomeric mAb, taken as 5 nm [234].

Effective mAb radii for visible species (r_{eff}^{vis}) were calculated directly from measured diffusion coefficients DL using the Stokes-Einstein equation, combined with a correction for the effects of molecular crowding [318, 319]:

$$r_{eff}^{vis} = \frac{kT}{6\pi\eta D_L}\frac{(1-\varphi)^3}{(1+\frac{3}{2\varphi}+2\varphi^2+3\varphi^3)} \qquad \text{(Equation 4.4)}$$

where φ is the total volume fraction of the proteins in solution assuming a protein density factor of 1.25 g/mL [318, 320].

4.4 Results

4.4.1 Characterisation of dark states in ^{19}F-tagged mAb mixtures

To assess whether DEST effects could be observed in ^{19}F-tagged mAbs, two equimolar mAb mixtures were prepared, one consisting of COE-19-TFBPD with mAb2-TFCS, and a second with the ^{19}F tags reversed (i.e. COE-19-TFCS mixed with mAb2-TFBPD). Data were collected at two different concentrations (160 and 400 mg/mL total) and across a range of temperatures rising from 277 to 313K. At each condition ^{19}F NMR spectra were collected measuring translational diffusion coefficients D_L (to capture the sizes of the visible species), as well as observed relaxation rates (R_1 and R_2^{obs}) and DEST spectra for full DEST fitting, taking into account lifetime line broadening, for each mAb represented by their ^{19}F tags. A typical example of a DEST profile fitted to the two-state model is shown in Figure 4-1. Further examples are shown in Figure S4-3, with fitted rate constants shown on Figure S4-4.

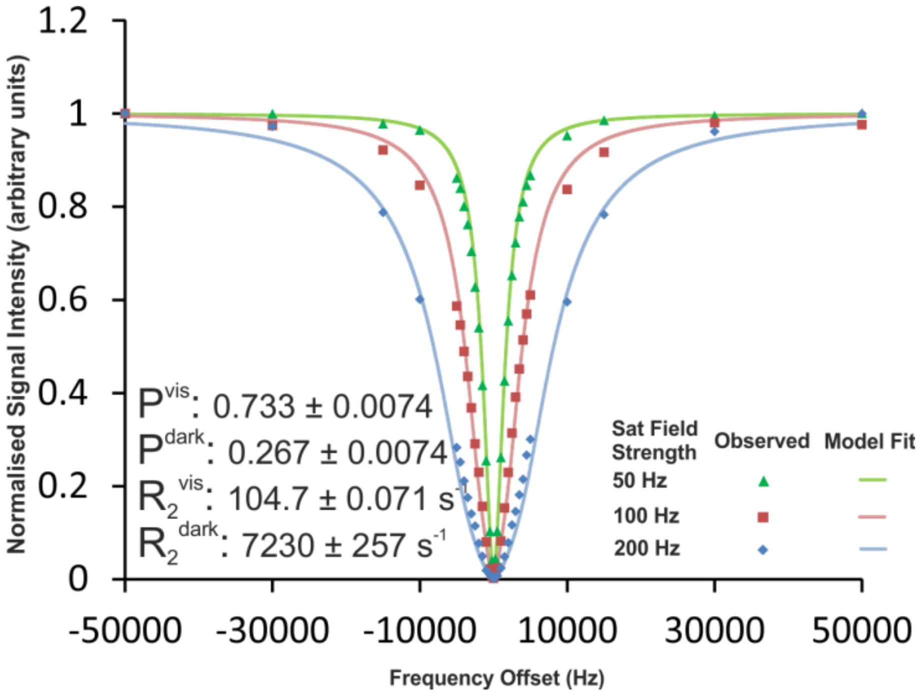

Figure 4-1. Example of DEST profiles for mAb2-TFBPD in an equimolar mixture with COE-19-TFCS (total concentration 160 mg/mL). Data was collected at 277K at three saturation field strengths and fitted simultaneously to minimize the combined residuals. Markers indicate the measured data points, while the continuous lines show the calculated DEST profiles from the model fitted to them.

It was noted that ^{19}F signal losses and signal broadening at low temperature were much greater for both mAbs when tagged with TFBPD than for the same mAbs tagged with TFCS. This effect is clearly visible in the 1D ^{19}F spectra (Figure S4-5) and in the observed different characteristic ranges for transverse relaxation values R_2^{obs} for TFCS and TFBPD tags when attached to mAbs (Figure 2). This difference can be explained by the relative differences in the tag length and flexibility (structures shown in Figure S4-5). TFCS contains a long flexible alkyl linker and attaches to lysine side chains, giving the fluorine moiety considerable freedom to move relative to the attached protein. TFBPD is more rigid and attaches to the shorter cysteine side chain, resulting in a faster relaxation rate. TFCS with its greater mobility will remain NMR visible even when attached to relatively large clusters, for which the signal of the less mobile TFBPD would have already been lost to the NMR dark state. We hypothesised that the two tags would essentially report on different size ranges of associates, both in visible and in dark states. When using the TFCS tag only the very large mAb clusters would have a high enough R_2 to be in the NMR dark state, with most of the smaller oligomers remaining in the visible fraction, which can be then observed for example by DOSY. When using the TFBPD tag more of the smaller oligomers will be in the dark state rather than the visible.

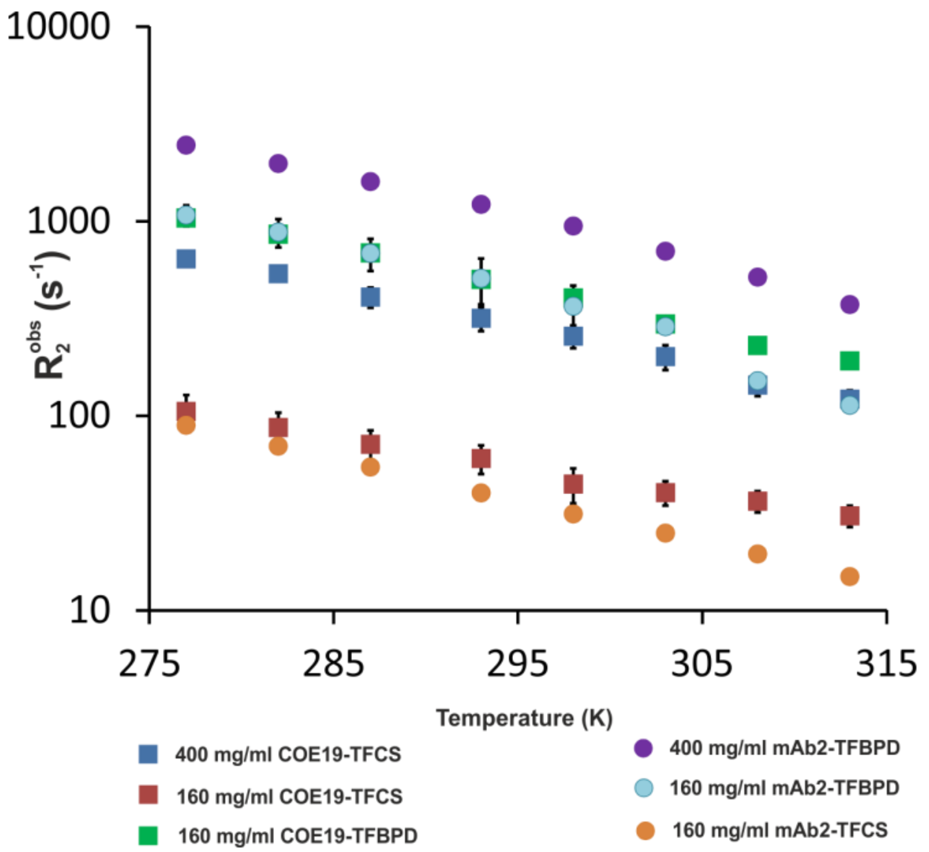

Figure 4-2. Temperature dependence of observed effective transverse relaxation rate (R_2^{obs}). Two mAb-tag combinations (COE-19-TFBPD/mAb2-TFCS and COE-19-TFCS/mAb2-TFBPD) in equimolar mixtures at different concentrations.

In order to explore this further, we analysed how the distributions of the visible and dark state populations depend on temperature and concentration of mAbs (Figure 4-3). As hypothesised, the dark state populations are significantly larger for each mAb when tagged with TFBPD than with TFCS. The data shows that for TFCS-tagged mAbs a wider range of apparent cluster sizes remains in the visible state. With the same tags used, COE-19 is consistently much more represented in the dark state population than mAb2 at each condition, revealing its greater aggregation propensity. Both mAbs show a consistent decrease in the populations of their dark state species at higher temperature, and an increase in the dark state at higher concentration (Figure 4-3). The data suggests that formation of large dark state protein clusters is exacerbated by low temperature and increased concentration, however different antibodies in the mixture are affected to varying extents.

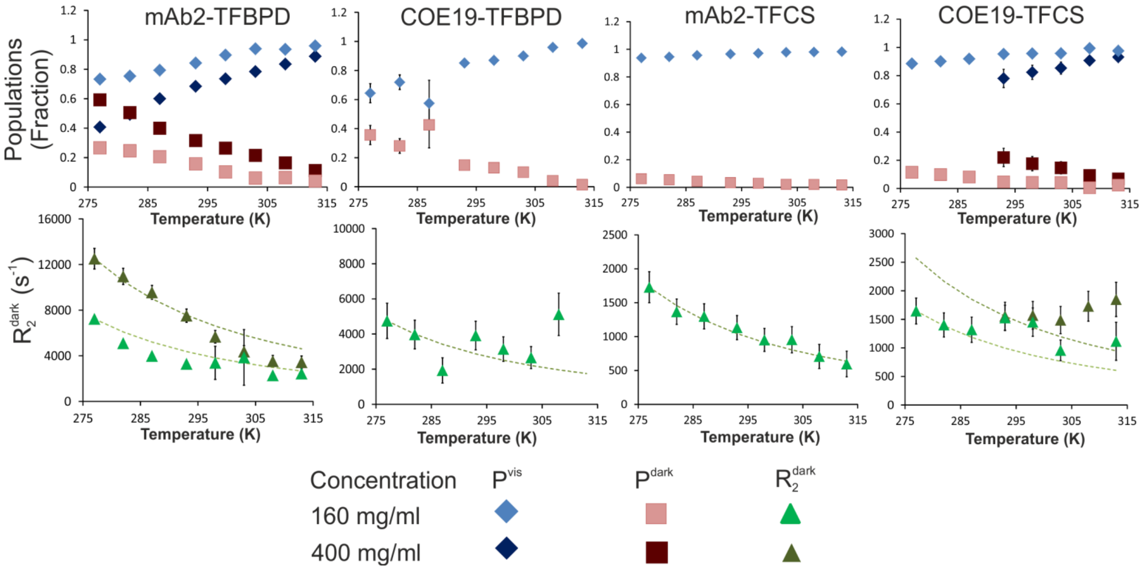

Figure 4-3. DEST data for all four mAb-tag combinations for temperatures from 277K to 313K. Upper row shows the variation of the visible population and the dark state population. Lower row shows relaxation rate R_2^{dark}. The green dashed guidelines show the projected change in R_2^{dark} based solely on the effect of temperature and viscosity. Data was obtained in the samples containing equimolar mixtures of labelled mAbs as shown, at total concentrations of 160 mg/mL, with selected data available for 400 mg/mL mixed sample. Error bars are present for all data points, but for some values are smaller than the markers shown. Where $P^{dark} \approx 0$ the value of R_2^{dark} is not defined and therefore is not shown for these points.

4.4.2 Effects of temperature and concentration on apparent radius of mAbs

The dependencies of the fitted relaxation rates R_2^{dark} on temperature are dominated by the expected change in water viscosity. The deviations from this expected trend can be interpreted as changes in the effective size of the dark state clusters. This allows calculation of a nominal effective radius of protein clusters in this dark state [313] (shown in Figure 4-4) and comparison to the effective radii r_{eff}^{vis} calculated from the translational diffusion coefficients $\mathrm{D_L}$ (Figure S4-6), which reflect the apparent size of the smaller mAb oligomers still visible in the NMR spectra. It can be seen that DEST consistently reports a larger effective radius $r_{cluster}^{vis}$ for the dark state clusters when using the TFCS tag compared to the TFBPD tag, in agreement with our hypothesis that the TFBPD dark state includes smaller oligomers than the TFCS dark state for a given protein. The translational diffusion data, which reports on the visible oligomeric species, consistently reports molecular sizes larger than expected for a monomer (ca. 5 nm).

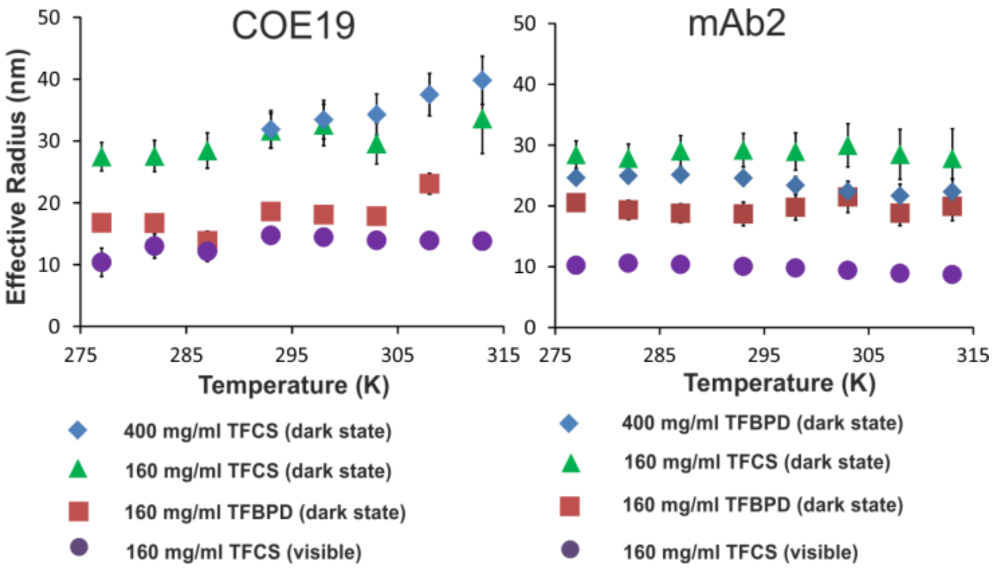

Figure 4-4. The temperature dependence of effective mAb radii. MAb visible oligomers r_{eff}^{vis} and dark state clusters $r_{eff}^{cluster}$ in the mixed samples of COE-19 and mAb2 labelled with different tags.

We can estimate the concentration of dark state clusters for each dataset (Figure 4-5). The apparent concentrations of large dark state clusters for TFCS-tagged mAbs are much lower than for TFBPD-tagged mAbs. Both mAbs show an increased cluster concentration at higher protein concentration and at lower temperature, however the nominal concentration of such clusters for each mAb is very small (<10 µM) when compared with the mAb concentration (1.3 mM). Interestingly at lower temperature an increase in the number of large COE-19 clusters (Figure 4-5) is accompanied by a reduction in their size (Figure 4-4). In contrast for mAb2, while the number of large clusters increases at lower temperatures, their size remains constant.

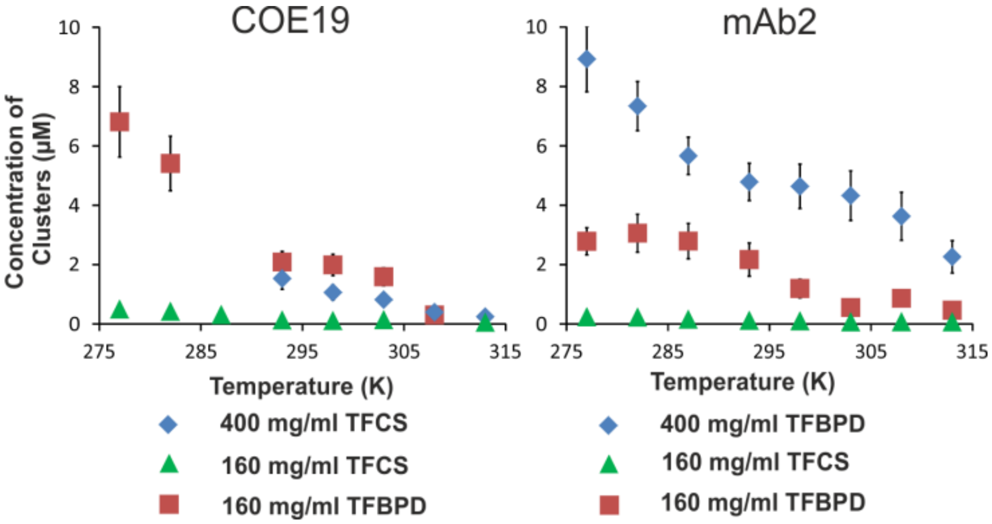

Figure 4-5. The calculated effective concentrations of dark state clusters. Concentrations for COE-19 and mAb2 derived from the dark state populations and cluster radii.

4.4.3 Effects of additives – excipients, salt and denaturant

^{19}F DEST can be used to investigate the effect of additives on disrupting the dark state mAb clusters, detecting reductions in cluster size, cluster concentration or both. Detailed understanding of protein-specific clustering mechanisms and effects of excipients would therefore require quantification of both the sizes and concentrations of protein clusters. An equimolar mixture of L-arginine and L-glutamate (Arg·Glu) has been reported to reduce aggregation of mAbs and other proteins [105, 152, 233]. Adding salt (NaCl) can potentially promote or disrupt aggregation controlled by the balance between electrostatic and hydrophobic interactions [195, 196, 321]. The effects of these additives on dark state clusters in COE-19-mAb2 mixtures are summarised in Table 4-1.

Generally, the effect of additives such as Arg·Glu and NaCl is mAb-specific. Arg·Glu does reduce the dark state population for COE-19 while showing a weak trend in reducing both its cluster size and concentration. For mAb2 in the same mixed sample, the overall dark state population does not change noticeably however the relaxation rate of the dark state R_2^{dark} is reduced, suggesting that the cluster size for mAb2 becomes smaller, at the expense of having slightly more clusters. Adding NaCl reduces the dark state population for COE-19 but has little effect on mAb2. R_2^{dark} for COE-19 increases, implying some increase in the average cluster size, which is however accompanied by drastic reduction in the overall concentration of these large clusters. The greater sensitivity of COE-19 to the solvent conditions fits with earlier observations that COE-19 is more prone to self-association and generally has lower solubility, and hence is more problematic than mAb2 [234]. Addition of denaturant (GdnHCl) completely removed the dark state populations for both COE-19 and mAb2 in the control sample, converting both proteins to an entirely monomeric and unfolded state (see Figure S4-7).

	mAb-tag Combination	**Additive**	**Conc (M)**	**P^{dark} (fraction)**	**R_2^{dark} (s^{-1})**	**k_{BA}, (s^{-1})**	**$r_{eff}^{cluster}$ (nm)**	**Cluster Conc., (μM)**
I	**COE-19-TFCS**	Arg·Glu	0	0.14 ± 0.02	1400 ± 200	900 ± 100	26.4 ± 1.2	0.7 ± 0.2
	COE-19-TFCS	Arg·Glu	0.200	0.08 ± 0.01	1200 ± 200	900 ± 200	24.4 ± 1.3	0.5 ± 0.2
	mAb2-TFBPD	Arg·Glu	0	0.30 ± 0.02	6500 ± 600	2500 ± 200	19.8 ± 0.6	3.5 ± 0.6
	mAb2-TFBPD	Arg·Glu	0.200	0.27 ± 0.03	4000 ± 500	2400 ± 300	16.8 ± 0.7	5.1 ± 1.4
II	**COE-19-TFCS**	NaCl	0	0.20 ± 0.03	1300 ± 200	800 ± 200	25.3 ± 1.4	1.1 ± 0.4
	COE-19-TFCS	NaCl	0.150	0.10 ± 0.01	2000 ± 300	1800 ± 400	29.4 ± 1.6	0.3 ± 0.1
	mAb2-TFBPD	NaCl	0	0.33 ± 0.02	8000 ± 700	2500 ± 200	21.2 ± 0.6	3.2 ± 0.5
	mAb2-TFBPD	NaCl	0.150	0.30 ± 0.02	8600 ± 700	3300 ± 200	21.7 ± 0.6	2.6 ± 0.4

Table 4-1. The effects of additives on dark state clusters of COE-19 and mAb2 observed at 277 K. The two samples (I and II) contained equimolar mixtures (160 mg/mL total) of COE-19 and mAb2 labelled as shown. The measurements were performed for each sample before and after pre-measured lyophilized additives were added at specified concentration. Those pairs showing absolute differences in observed values which are greater than the sum of the correspondent standard deviations are highlighted grey.

4.5 Discussion

Understanding the effects of external stimuli such as temperature or changes in solution conditions on protein-specific clustering at high concentrations is extremely challenging in heterogeneous solutions containing several protein components. Whether the clusters are formed by a mixture of proteins, or if each protein tends to be part of its own homogeneous cluster, cannot be easily deduced from traditional measurements such as light scattering. ^{19}F DEST NMR described here in combination with the differential labelling strategy proposed previously [234] allows detection and quantification of dark state aggregates for multiple proteins simultaneously and independently in the same sample. The analysis can then show if the observed proteins become part of the same cluster, in which case they should both experience joint tumbling, or different clusters of substantially different size. Even if proteins do not interact with each other tightly to form functional biological complexes, under extremely high concentrations and in crowded conditions weak cross-interactions between proteins become as important as self-interactions.

Large cluster formation may lead to unwanted mAb solution opalescence, and identifying which components of the mixture are responsible would be important [322]. Here we studied cluster formation in a mixture of two mAbs at high concentration, up to 400 mg/mL. We found no evidence for uniformly-mixed clusters composed of both proteins, in either the dark state or the visible state (which will include some low oligomers). The protein cluster sizes showed different tendencies, with both large and small COE-19 cluster radii increasing with temperature, whereas for mAb2 radii remained the same for large clusters but reduced slightly for the smaller NMR-visible clusters (Figure 4-4). The concentrations of the large dark state clusters generally increased at low temperature for both mAbs (Figure 4-5). The clusters of these two mAbs also responded differently to the addition of Arg·Glu and NaCl (Table 4-1). These observations reveal that different mAbs in the mixture may respond differently to the external stimuli and change of conditions. ^{19}F DEST allows the clustering properties of different proteins to be observed even when they are mixed together at very high concentration, allowing straightforward testing of conditions and excipients, without signal interference from any other unlabelled sample constituents. Although in our studies we have not observed that addition of relatively small ^{19}F-tags affects association properties of large protein molecules such as mAbs [234], appropriate care should be taken in new systems studied.

Different ^{19}F tags, depending on their length and flexibility, enable us to sample slightly different characteristic sizes of protein clusters. This would allow fine-tuning the nature of the tag to the requirements of the system. For example when investigating very large slow-tumbling proteins a longer tag (such as TFCS) will still provide a useful reporter signal.

4.6 Conclusions

This study has demonstrated that novel ^{19}F DEST analysis enables detection and characterization of different types of large NMR-invisible clusters formed reversibly by differentially-tagged mAbs at high concentration. Selection of ^{19}F tags with differing inherent flexibility and transverse relaxation rates allows sampling of different cluster sizes. Use of ^{19}F differential labelling allows working with large proteins (e.g. the 145 kDa antibodies tested here) and complex solutions without any interference from background signals. This is particularly relevant when it is necessary to study mAb mixtures at ultra-high concentrations (up to 400 mg/mL), for example, in drug product stability testing. The results suggest that instead of engaging in uniformly-mixed clusters, IgG proteins mAb2 and COE-19 are involved in more homogeneous large self-assemblies which co-exist in solution at relatively low concentrations, and which respond somewhat differently to external stimuli, such as temperature or additives. The measurable parameters thus allow us to reveal the mechanisms of protein-specific reversible cluster formation in complex concentrated mixtures and fine-tune the conditions to achieve the required solution properties, such as minimal overall aggregation and solution viscosity. The proposed approach could be used to study the onset of phenomena such as aggregation, opalescence and liquid-liquid phase separation in any protein mixture.

4.7 Acknowledgments

JME was funded by MedImmune Ltd, part of AstraZeneca plc. JEB was funded by CASE DTP Ph.D. studentship BB/M011208/1 from the UK Biotechnology and Biological Sciences Research Council (BBSRC) in partnership with MedImmune Ltd. We are grateful to Professors Jeremy Derrick and Alan Dickson, and Jiali Du

(MedImmune) for useful discussions, to Dr Matthew Cliff for help with pulse sequence programming and for looking after the NMR Facility, and to the Marius Clore and Vincenzo Venditti groups, and Vitali Tugarinov for sharing sample DEST fitting scripts.

4.8 Supporting Information

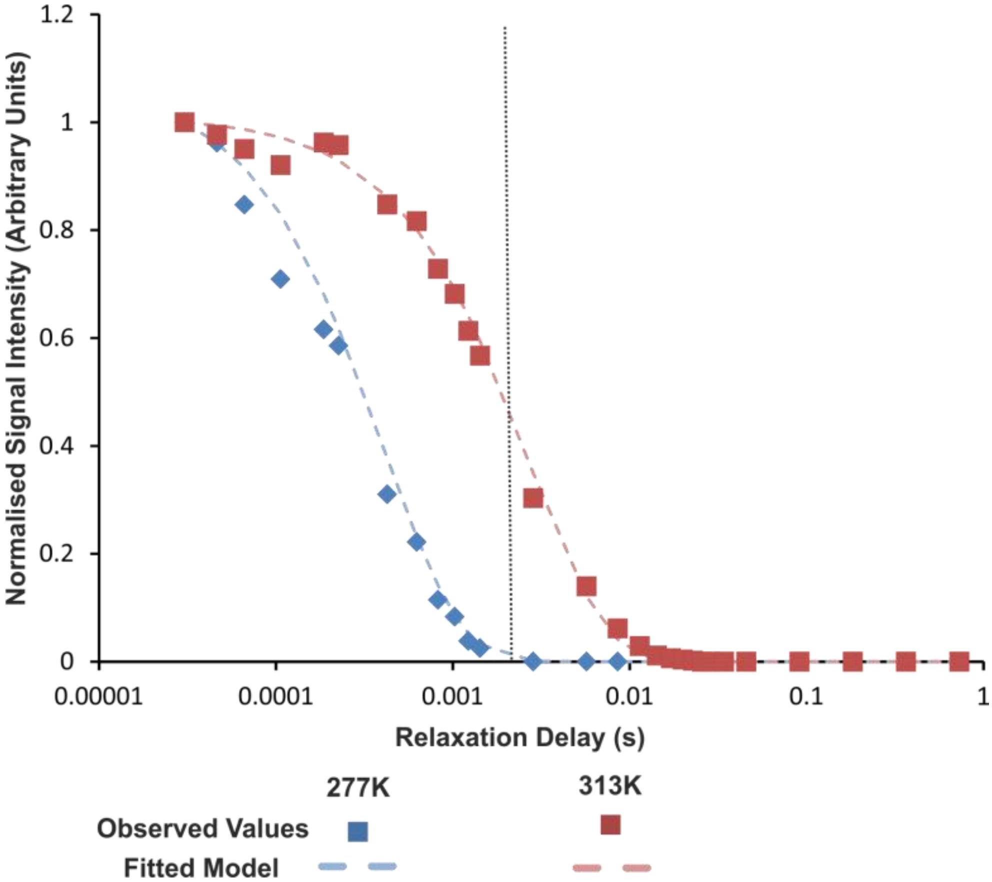

Figure S4-1. Examples of intensity decay curves from a combined pair of R_2 relaxation experiments. These consist of one experiment covering T2 relaxation delays of 2.8 ms to 730 ms while varying the number of echo pulses separated by fixed echo delays, and an additional identical experiment in which the number of echo pulses was fixed at the minimum and the echo delay was decreased incrementally to produce effective delay times of between 1.5 and 0.03 ms. Data points from both experiments were combined and fitted simultaneously using Dynamics Center 2.4.8 to extract the single ‘observed’ R_2^{obs} value. X-axis is logarithmic. Data is for mAb2-TFBPD at 400 mg/mL total mAb concentration, shown for temperatures of 277K and 313K. This sample at 277K had the most rapid relaxation measured in this study. The black dotted line indicates the join between the data from the modified NMR experiment for ultra-fast relaxation (left) and the conventional CPMG experiment (right).

$$\frac{d}{dt}\begin{bmatrix} E/2 \\ I_x^A \\ I_y^A \\ I_z^A \\ I_x^B \\ I_y^B \\ I_z^B \end{bmatrix} = -\begin{bmatrix} 0 & 0 & 0 & 0 & 0 & 0 & 0 \\ 0 & R_2^A + k_{AB}^{app} & \Omega^A & -\omega_y & -k_{BA} & 0 & 0 \\ 0 & -\Omega^A & R_2^A + k_{AB}^{app} & \omega_x & 0 & -k_{BA} & 0 \\ -2\theta^A & \omega_y & -\omega_x & R_1^A + k_{AB}^{app} & 0 & 0 & -k_{BA} \\ 0 & -k_{AB}^{app} & 0 & 0 & R_2^B + k_{BA} & \Omega^B & -\omega_y \\ 0 & 0 & -k_{AB}^{app} & 0 & -\Omega^B & R_2^B + k_{BA} & \omega_x \\ -2\theta^B & 0 & 0 & -k_{AB}^{app} & \omega_y & -\omega_x & R_1^B + k_{BA} \end{bmatrix} \times \begin{bmatrix} E/2 \\ I_x^A \\ I_y^A \\ I_z^A \\ I_x^B \\ I_y^B \\ I_z^B \end{bmatrix}$$

Figure S4-2. Bloch-McConnell matrix used for modelling the DEST effect for exchange between NMR-visible species A and the dark state B. Here, E is unity; k_{AB}^{app} and k_{BA} are the apparent forward association and reverse dissociation rate constants, respectively; I_x^n, I_y^n, I_z^n are the equilibrium magnetisation in the x, y, and z axis, respectively, with I_z^n dependent upon equilibrium state populations ($P^A = P^{vis}$ and $P^B = P^{dark}$); R_1^n and R_2^n are the longitudinal and transverse relaxation rates, respectively; $\theta^n = R_1^n \times I_z^n$, Ω^n is the saturation frequency offset in rad·s^{-1}; and ω_x and ω_y are the CW saturation field strength (γB1) (rad·s^{-1}) about the x and y axis, respectively. Lifetime line broadening was calculated as R_2^{obs} - R_2^{mon}, providing an estimate of k_{AB}^{app} at each condition, with $k_{BA} = k_{AB}^{app} \times \frac{P^A}{P^B}$. Model parameters P^A (= P^{vis}), P^B (= P^{dark}) $= 1 - P^A$, and R_2^B (=R_2^{dark}) were fitted to experimental profiles using an in-house MATLAB script, which minimises the difference between experimental and simulated DEST profiles for the two or three saturation field strengths simultaneously. Fitting uncertainties for the model parameters were computed using Monte-Carlo simulations, with uncertainties of derived parameters calculated by error propagation.

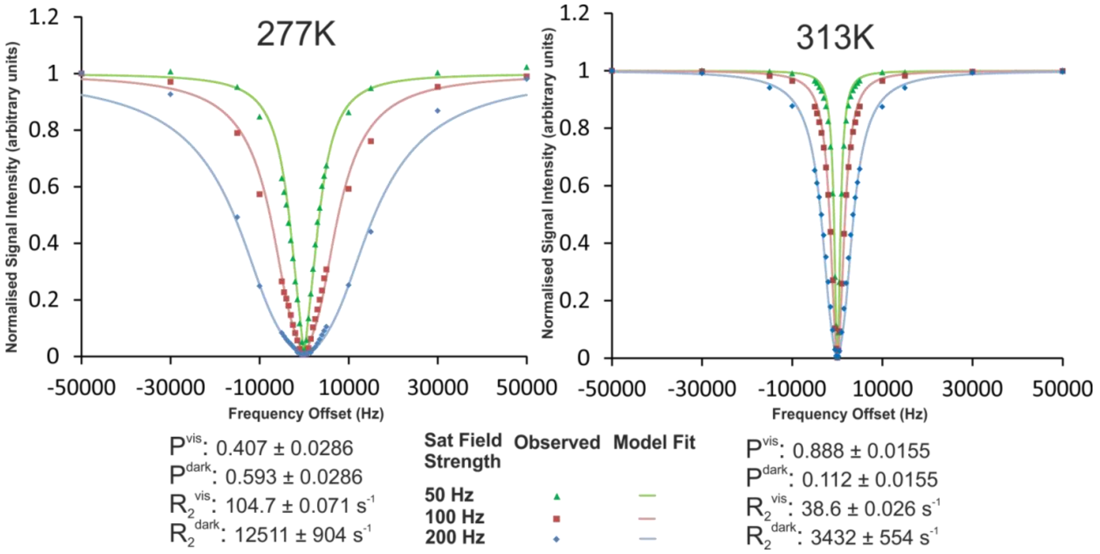

Figure S4-3. Further examples of DEST models fitted to observed data. Examples shown are for mAb2-TFBPD in a 400 mg/mL equimolar sample (200 mg/mL mAb2-TFBPD, 200 mg/mL COE-19-TFCS). Data collected at 277K and 313K, at three saturation fields: 50 Hz, 100 Hz, 200 Hz. R_2^{mon} value of 38.6 ± 0.03 s^{-1}.

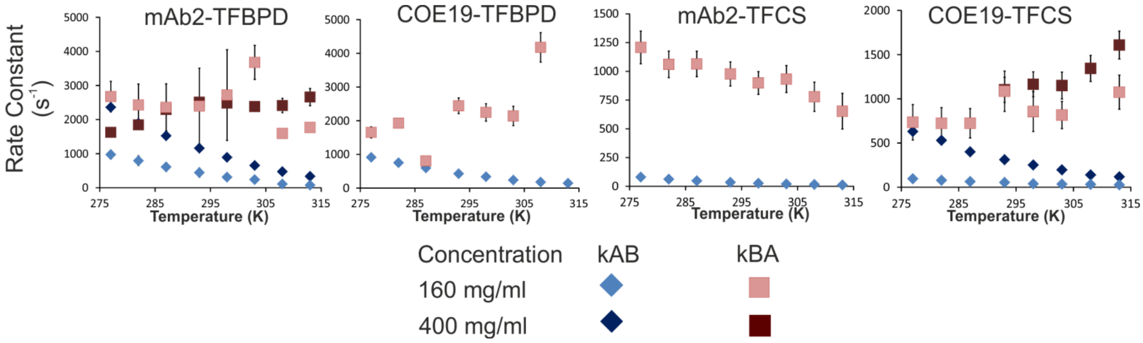

Figure S4-4. Rate constant data for two mAbs at different temperatures. The value of k_{AB}^{app} at each condition was derived from lifetime line broadening calculated as R_2^{obs} - R_2^{mon}, with $k_{BA} = k_{AB}^{app} \times \frac{P^A}{P^B}$.

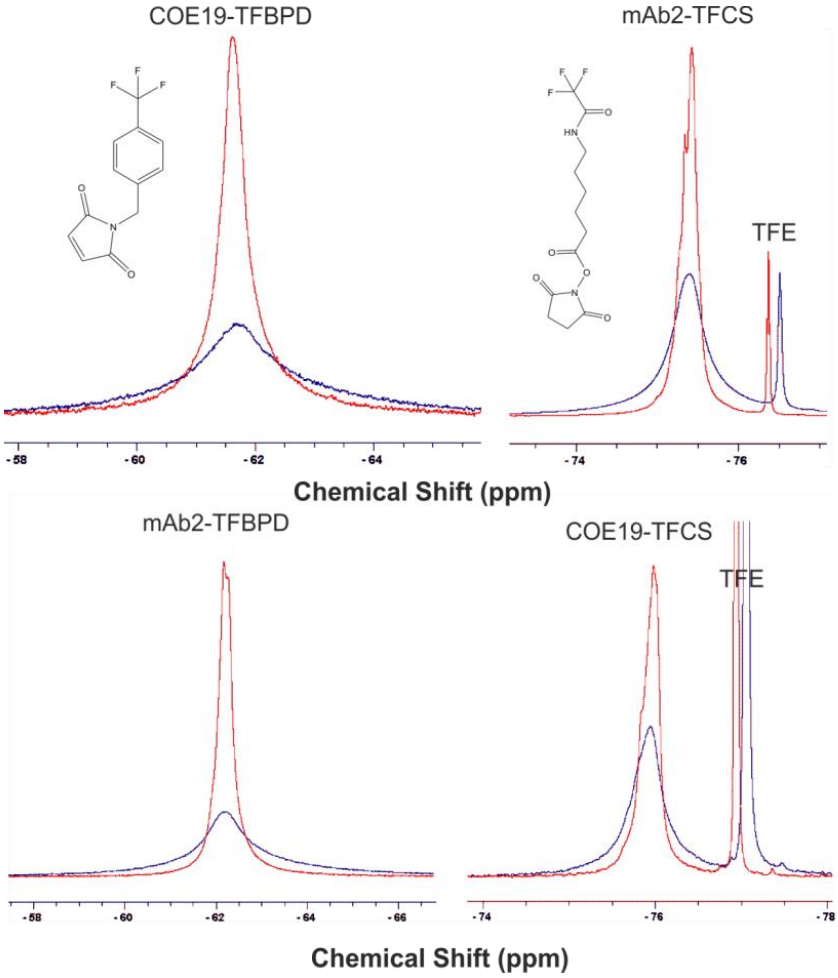

Figure S4-5. Overlays of the 1D ^{19}F NMR spectra for the four mAb-Tag combinations at 277K (in blue) and 313K (in red). Each peak is shown on the same scale at the two temperatures, but different mAb-Tag combinations are not to scale due to differences in labelling efficiency and hence absolute signal intensity. Spectra chemical shifts have been aligned so mAb peaks are directly overlaid. The additional signal visible at around 76.5 ppm is from the small molecule trifluoroethanol (TFE) added as an internal reference to check dilution accuracy.

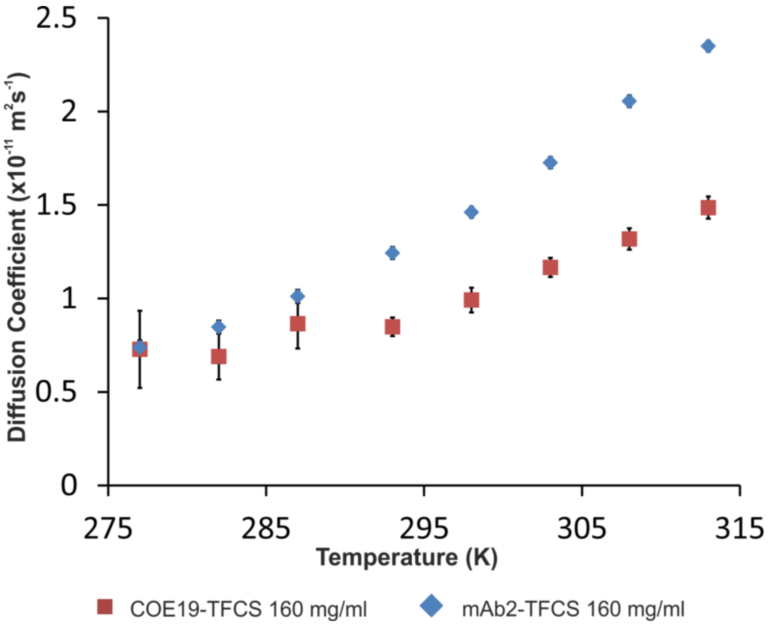

Figure S4-6. Raw diffusion coefficients D_L for both mAbs tagged with TFCS. Data is for 160 mg/mL total mAb concentration samples. Data could not be collected for TFBPD tagged mAbs, or at higher concentration, as rapid relaxation resulted in complete loss of signal before measurable diffusion could occur.

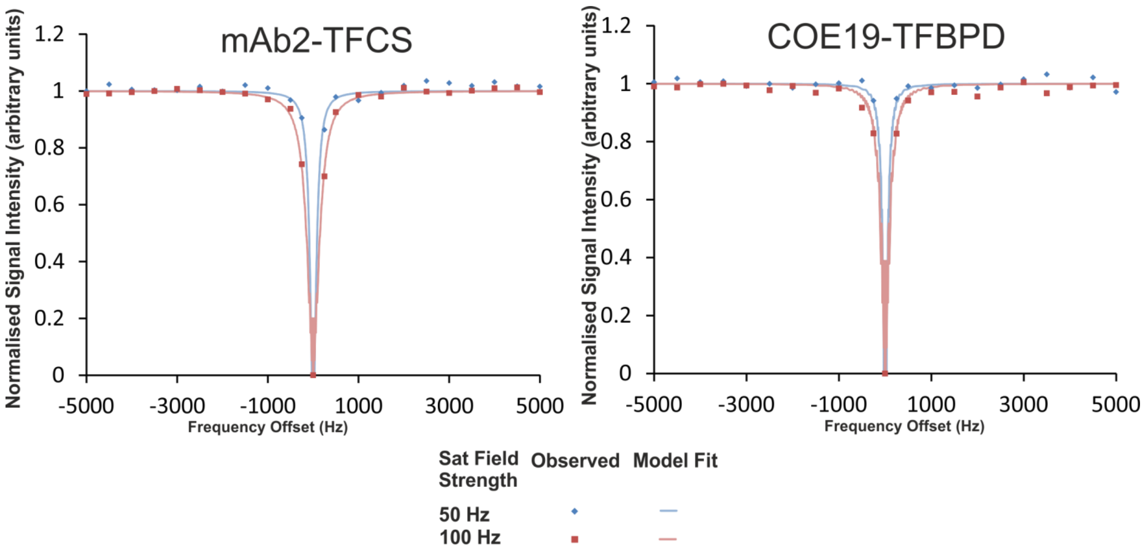

Figure S4-7. DEST model, with fixed P^{vis} = 0.99999 (i.e. no dark state population) simulated for experimental data of an equimolar sample of mAb2-TFCS and COE-19-TFBPD completely denatured with 6 M GdnHCl. Relaxation rates $R_2^A = R_2^{mon}$ corresponding to monomeric states of mAb2-TFCS and COE-19-TFBPD in these experiments were also measured in the presence of 6M GdnHCl (1.83 and 3.41 s^{-1} for mAb2-TFCS and COE-TFBPD, respectively). Data was collected at 313 K, in a 3 mm NMR tube.

5 Temporal and spatial characterisation of protein liquid-liquid phase separation using NMR spectroscopy

This chapter was prepared for submission as a research paper:

Jack E. Bramham[1], and Alexander P. Golovanov[1]

[1] Manchester Institute of Biotechnology and School of Chemistry, Faculty of Science and Engineering, The University of Manchester, Manchester, M1 7DN, UK

Author contributions:

J.E.B. performed experiments, analysed the data, and drafted the manuscript. A.P.G. conceived and supervised the project and provided input regarding data analysis. The manuscript was written through contributions of all authors.

5.1 Abstract

Liquid-liquid phase separation (LLPS) of protein solutions is increasingly recognised as an important phenomenon in cell biology and biotechnology. However, opalescence and concentration fluctuations render LLPS difficult to study, particularly when characterising the kinetics of the phase transition and layer separation. Here, we demonstrate the use of a probe molecule trifluoroethanol (TFE) to characterise the kinetics of protein LLPS by NMR spectroscopy. The sensitivity of the TFE probe to protein concentration enables bulk-detection ^{19}F NMR to simultaneously report on the formation and evolution of lean and dense phases throughout the sample. Meanwhile, spatially-selective ^{19}F NMR, in which spectra are recorded from smaller slices of the sample, is used to track the distribution of the different phases during layer separation. This experimental strategy enables comprehensive characterisation of the process and kinetics of LLPS, and may be useful to study phase separation in protein systems as a function of their environment.

5.2 Introduction

During liquid-liquid phase separation (LLPS), a homogenous mixture of macromolecules separates into two distinct liquid phases, the 'dense' phase enriched with a subset of components, and the 'lean' phase depleted of these components. This process is increasingly recognised in biology [182, 323], where it is responsible for the formation of membraneless organelles, including the nucleolus [324] and stress granules [191], but also implicated in a range of diseases, including neurodegenerative diseases [190, 325, 326], cataracts [164, 192], and sickle cell anaemia [327]. LLPS is also an important phenomenon in biotechnology, as a purification and processing technique [328], or as an unwanted physical instability in biopharmaceuticals [136].

LLPS can manifest as a suspension of small dense liquid droplets within the lean phase (microscopic LLPS), or as distinct dense and lean layers following layer separation (macroscopic LLPS). The kinetics of these processes, and the effect of different conditions or additives on these kinetics [329], is of particular interest. However, these processes are difficult to study by existing techniques. Light scattering due to the presence of liquid droplets, or fluctuations in density or refractive index often results in opalescent or turbid solutions, rendering quantitative optical approaches very challenging [141, 330]. Additionally, layer separation results in a non-uniform distribution of phase throughout the sample, adding a complicating spatial component [170]. Therefore, the physical and geometrical constraints of biophysical techniques, such as microscopy, and neutron and X-ray scattering, mean that they may be limited to studying one aspect of LLPS, but not the entire process.

Nuclear magnetic resonance (NMR) spectroscopy is a powerful biophysical technique, which has recently been applied to characterise protein LLPS. High-resolution multidimensional approaches have been used to probe molecular interactions prior to biological LLPS, and in isolated lean and dense fractions [238, 243, 245, 331-333]. However, the typical properties of phase separating systems render it difficult to use NMR to study the actual process of LLPS, and in particular layer separation. Firstly, macroscopic LLPS leads to significant density and concentration differences across the sample, resulting in distorted or broadened NMR signals due to magnetic field inhomogeneity [249]. Secondly, increased viscosity in the dense phase typically results in poor NMR signal properties due to slow molecular tumbling and fast transverse relaxation [243, 250].

With these considerations in mind, we propose a new approach with the use of a fluorinated probe molecule, in combination with bulk-detection and spatially-selective NMR, to comprehensively study solution behaviour preceding, during and after protein LLPS. The use of a small fluorinated probe molecule in ^{19}F NMR spectroscopy results in a single observable signal, whose behaviour reflects that of the protein solution, but whose NMR signal properties, such as relaxation and tumbling, are more amenable than those of the larger macromolecules. Meanwhile, in spatially-selective NMR, application of a selective radiofrequency pulse during a magnetic field gradient allows investigation of a small defined slice of the sample [258], resulting in a localised NMR spectra with reduced field inhomogeneity [259, 263, 334]. Spatially-selective NMR therefore enables characterisation of the spatial component of LLPS.

In this study, we demonstrate the potential of this experimental approach to characterise both the temporal and spatial aspects of protein LLPS by applying it to the model protein bovine serum albumin (BSA), which undergoes spontaneous macroscopic LLPS in the presence of yttrium chloride (YCl_3) at elevated temperatures [160, 161, 170]. We show that trifluoroethanol (TFE) as a probe molecule is sensitive to the local protein concentration, and can report on different phases present simultaneously in the sample. The kinetics of LLPS at different temperatures are then examined by bulk-detection NMR, with the formation of dense and lean phases throughout the solution monitored over time. On a longer timescale, the process of the two phases separating into distinct layers is monitored and characterised by spatially-selective NMR. We show that a fluorinated probe molecule in combination with bulk-detection and spatially-selective ^{19}F NMR spectroscopy is an excellent experimental strategy to comprehensively assess the process of protein LLPS.

5.3 Materials and Methods

5.3.1 Sample preparation

Lyophilised bovine serum albumin (BSA) powder (essentially fatty acid and globulin free, >99%, Sigma-Aldrich, #A0281) was dissolved in distilled water (Mili-Q) to 10-20 mg/mL, then filtered with 0.1 µm syringe filters (Millex-VV, Merck). BSA solutions were subsequently concentrated by ultrafiltration (Vivaspin 20, 10 kDa MWCO, Sartorius) to the required concentration, with protein concentration measured by absorbance at 280 nm (A_{280}) with a NanoDrop (Thermo Scientific) following appropriate dilution. Yttrium chloride (YCl_3) (99.99%, Sigma-Aldrich) was also dissolved in distilled water, and then filtered with a 0.1 µm syringe filter.

LLPS was studied in protein solutions containing 200 mg/mL BSA with 20 mM YCl_3 and 10 mM TFE (Sigma-Aldrich). For NMR experiments examining LLPS *in situ*, 480 µL solution was pipetted into an NMR tube, with the coaxial insert inserted prior to LLPS. For NMR experiments involving bulk assessment of the separate layers, 1 mL protein solution was pipetted into an NMR tube, with LLPS and layer separation triggered in the tube by incubation at 40°C for 48 hours. After centrifugation with a hand crank tube centrifuge, the majority of the lean layer was then transferred to another tube. Finally, the residual lean layer and a small volume of the dense layer was discarded. Coaxial inserts were then inserted into the NMR tubes.

5.3.2 NMR spectroscopy

NMR experiments were conducted using a Bruker 500 MHz (470 MHz for ^{19}F) Avance III spectrometer with a QCI-F cryoprobe with cooled ^{1}H and ^{19}F channels, sample temperature control unit, and Z-gradient coils. Solutions containing the TFE probe molecule were placed in standard 5 mm O.D. NMR tubes (Wilmad), with coaxial inserts (50 mm stem length, Wilmad) containing deuterated dimethyl sulfoxide (DMSO-d_6) (99.8%, Eurisotop) for lock and 100 mM α,α,α-trifluorotoluene (TFT) (Sigma-Aldrich) as an external reference (see Figure S5-1 for schematic). For all experiments, NMR tubes were positioned such that the centre of the sample volume aligned with the centre of the NMR probe coil region. Magnetic field shimming was performed on the initial homogenous sample, with no further shimming between kinetic experiments.

For NMR with bulk detection (i.e. the conventional way of observing signals from the entire sample), 1D ^{19}F NMR spectra were recorded with the standard *zg* Bruker pulse sequence. Kinetic experiments were acquired in a pseudo-2D fashion, with the *zg2d* pulse sequence and processed with a 5 Hz exponential multiplication (EM) window function. All NMR spectra were initially processed in Topspin 4.0.8 (Bruker), with spectra plotted in Prism 8 (GraphPad).

5.3.3 Spatially-selective NMR

Spatially-selective NMR experiments were acquired by selective excitation applied during application of a magnetic field gradient, with the separate spectra observed for different areas of the same sample along the vertical z-axis. Here, a gradient field strength of 42.4 G/cm was applied concurrently to a G4 cascade selective pulse of bandwidth 16793 Hz, resulting in 1 mm wide excited slices. 12 evenly spaced selective pulse offsets, ranging from -93404.19 to +93404.19 Hz, were used, leading to twelve 1 mm slices collected, centred at -5.5 to +5.5 mm from the centre of the gradient coil (Figure S5-1). This central region exhibited acceptable gradient linearity (as judged by TFT reference signal integrals in spatially-selective spectra), with slice signal intensity corrected during processing to account for any non-linearity (Figure S5-2). Spatial experiments were acquired in an interleaved manner to enable use of a minimal relaxation delay (D_1) of 0.1 s.

Spatially-selective NMR series were initially processed in Topspin 4.0.8 with a 20 Hz EM window function, with auto-phase (*apk*0) and auto-baseline correction (*absn*). Processed spectra were exported in ASCII format, and further analysed, including peak picking, integration, and lineshape analysis, using in-house MATLAB scripts. When required, peak deconvolution was also performed using in-house MATLAB scripts, with two Lorentzian lineshapes fitted to the experimental data using nonlinear least-squares fitting.

5.3.4 ^{19}F Dark-state Exchange Saturation Transfer (DEST)

^{19}F DEST experiments were acquired according to the previously published protocol [282], with 1.0 s continuous-wave (CW) saturation applied at three saturation field strengths (50, 100, and 200 Hz) and at 24 unevenly-spaced offsets. ^{19}F DEST spectra were initially processed in Topspin 4.0.8. Further processing and fitting of the Bloch-McConnell model for two site exchange to the experimental data was performed in MATLAB with in-house scripts [282].

5.3.5 Relaxation

^{19}F longitudinal relaxation times (T_1) were measured using the standard inversion recovery sequence t1ir, while transverse relaxation times (T_2) were measured with a version of the Bruker Carr-Purcell-Meiboom-Gill (CPMG) sequence with perfect echo. CPMG echo time and repeats were altered to suit individual experimental conditions. T_1 and T_2 were calculated in Dynamics Center 2.5 (Bruker). Assuming that the transverse relaxation rate (R_2) is reduced only due lower viscosity and faster molecular tumbling at higher temperatures, the expected behaviour of R_2 at higher temperatures was calculated based on the proportionality of R_2 to rotational correlation time (τ_c), according to Stoke’s equation:

$$R_2 \propto \tau_C = \frac{4\pi\eta(r_{eff})^3}{3kT} \qquad \text{(Equation 5.1)}$$

where η is dynamic viscosity, r_{eff} is the effective radius of the species, k is the Boltzmann constant, and T is temperature. Rearranging the above equation gives the relaxation rate at temperature T:

$$R_2^T = R_2^{ref} \frac{\eta_T \, T_{ref}}{\eta_{ref} \, T} \qquad \text{(Equation 5.2)}$$

where η_T and η_{ref} are the dynamic viscosities of water at temperature T and the reference temperature T_{ref}, respectively.

5.3.6 Translational diffusion

Translational diffusion coefficients (D_L) were determined by diffusion ordered spectroscopy (DOSY) using the simulated echo pulsed-field gradient (PFG) pulse stebpgp1s. DOSY delays were optimised for each experimental condition, with diffusion times of 150 and 1500 ms, and gradient lengths of 1.5 and 0.3 ms for the lean and dense fractions, respectively. D_L were calculated in Dynamics Center 2.5. The expected values of the diffusion coefficient (D_L^e) at higher protein concentrations were calculated using the value of the diffusion coefficient measured in diluted conditions (D_L^e) and the model for molecular crowding [318, 319]:

$$D_L^e(\varphi) = D_L^{diluted} \times \frac{(1-\varphi)^3}{(1+\frac{3}{2}\varphi+2\varphi^2+3\varphi^3)} \qquad \text{(Equation 5.3)}$$

where φ is the BSA volume fraction in solution, calculated using protein concentrations and a specific volume of 0.735 mL/g for BSA [335]. The expected values of the diffusion coefficient at higher temperature T (D_L^T) were calculated using the rearranged Stoke's equation:

$$D_L^T = D_L^{ref} \frac{\eta_{ref} T}{\eta_T \, T_{ref}} \qquad \text{(Equation 5.4)}$$

where D_L^{ref} is the diffusion coefficient at the reference temperature T_{ref}, and η_T and η_{ref} are the dynamic viscosities of water at temperature T and T_{ref}, respectively.

5.4 Results

5.4.1 TFE signal is sensitive to local protein concentration

Previous observations suggest that monitoring LLPS by observing protein signals in NMR spectra is challenging, particularly in the dense fraction and approaching the phase transition, due to extreme signal broadening. Here, we investigated the use of a small fluorinated probe molecule, trifluoroethanol (TFE), added to the sample (10 mM final concentration) to study phase transitions and layer separation in a model protein system, BSA. We found that the TFE signal (observed at ∼ -77 ppm) is sensitive to protein concentration, as reflected by a number of NMR observable parameters (Figure 5-1), including exhibiting increased transverse relaxation rate (R_2) and reduced translational diffusion (D_L) with increasing protein concentration (Figure 5-1E-F), likely as a result of transient interactions with protein molecules. The concentration dependence of D_L closely follows the expected behaviour explained by increased molecular crowding alone (Figure 5-1F). Most importantly for our approach, TFE displays changes easily detectable in 1D ^{19}F NMR spectra, in particular linear chemical shift perturbations (Figure 5-1A) and increased linewidth (Figure 5-1C) with increasing protein concentration, allowing calibration of these parameters against known concentration values for a given protein and solution condition. As an additional control, 100 mM trifluorotoluene (TFT) in a coaxial insert in the same sample tube produces a simultaneously observed ^{19}F signal (at ~ -61 ppm) which reports on magnetic field homogeneity and temperature stability, while its solvent DMSO-d6 provides a lock signal without adulteration of the protein sample. This TFT signal is virtually unperturbed by changes in protein concentration (Figure 5-1), and its integral and chemical shift can be used as a convenient external reference. The observable signals from the probe molecules present in the sample therefore report directly both on protein concentration (TFE) and the macroscopic characteristics of the sample (TFT assessment of field homogeneity).

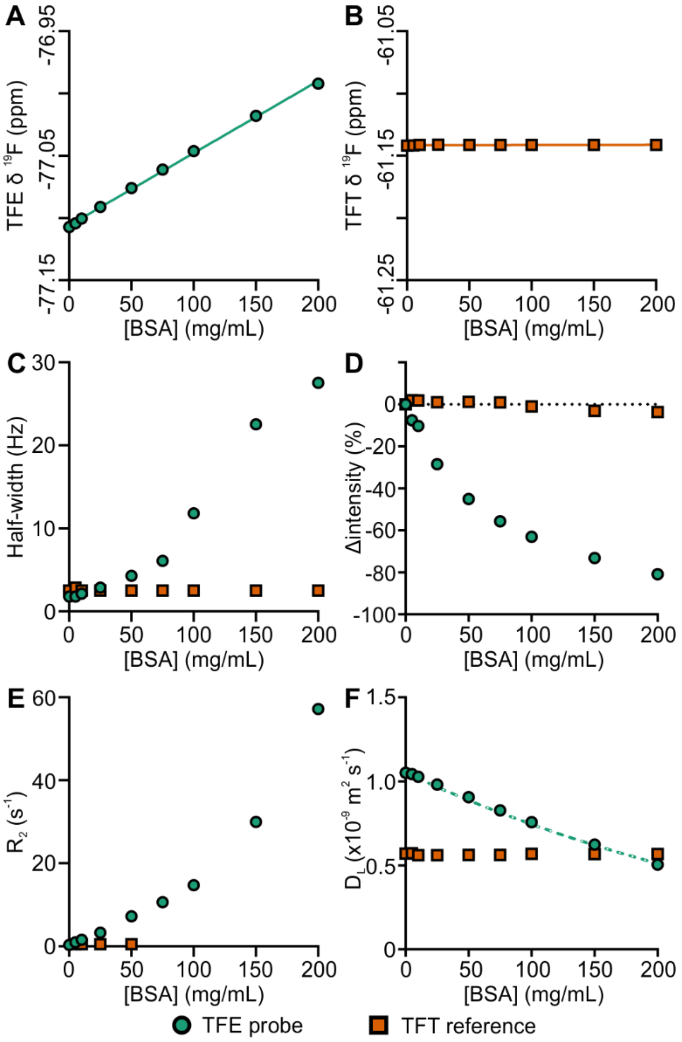

Figure 5-1. Effect of protein concentration on TFE probe and TFT reference NMR signal parameters. (**A**) TFE and (**B**) TFT chemical shift with increasing protein concentration, with linear fits plotted. (**C**) TFE and TFT linewidth. (**D**) Change in probe and reference intensities (normalised against intensity in the absence of BSA). Dotted guideline indicates zero level with no change. (**E** – **F**) Changes in transverse relaxation (R_2) and translational diffusion rates (D_L), respectively. The dotted guideline in F indicates the expected reduction in D_L as a consequence of increased molecular crowding ((Equation 5.3).

5.4.2 TFE behaviour in isolated dense and lean fractions

Having established that TFE is sensitive to protein concentration, we next investigated how protein behaviour differs between the dense (360 mg/mL) and lean (80 mg/mL) fractions produced by macroscopic LLPS at 40°C. LLPS was triggered in protein solutions by temperature incubation, with the resulting dense and lean layers separated, and each of the isolated fractions examined by bulk-detection NMR as a function of temperature (Figure 5-2).

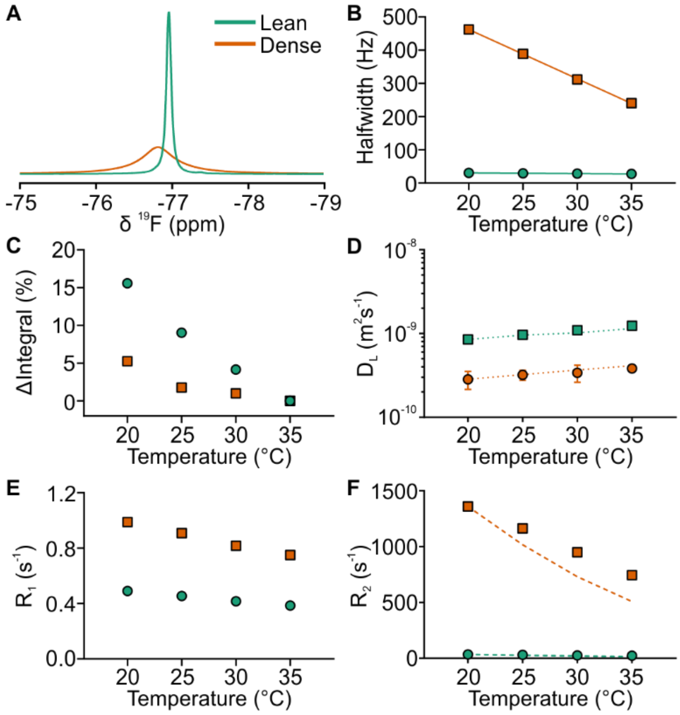

Figure 5-2. Analysis of the bulk-detected NMR spectra of isolated lean and dense fractions as a function of temperature. (**A**) Superimposed 1D ^{19}F NMR spectra of the two layers acquired at 35°C. Behaviour of 1D signal line width (**B**) and signal integral (**C**). (**D**) TFE translational diffusion coefficients as measured by DOSY NMR, with dotted lines indicating expected D_L based on temperature-dependent changes in water viscosity ((Equation ***5.4***). TFE longitudinal (E) and transverse (F) relaxation rates as a function of temperature. Dashed guidelines indicate expected behaviour given an assumption that relaxation rate is reduced only due to lower viscosity and faster molecular tumbling at higher temperature ((Equation ***5.2***).

TFE NMR signals were markedly different in the two fractions, with the lean fraction resulting in a narrow intense peak upfield of the broader dense fraction signal (Figure 5-2A). This chemical shift difference between the two fractions is consistent with the calibration relationship established earlier (Figure 5-1A). In the dense fraction, TFE exhibits significantly slower diffusion and faster relaxation rates (Figure 5-2D-F) than in the lean fraction, likely as a result of increased crowding and TFE interacting with self-associated BSA assemblies. Although the temperature dependence of molecular diffusion in both dense and lean fractions can be fully explained by changes in water viscosity (Figure 5-2D), R_2 in the dense fraction decreases with temperature slower than expected from viscosity alone (Figure 5-2F), suggesting additional temperature-dependent changes in the chemical exchange regime. To investigate the rapid R_2 observed in the dense fraction further, ^{19}F Dark-state Exchange Saturation Transfer (DEST) profiles were recorded at 20°C for the isolated fractions (Figure 5-3). DEST NMR reports on the presence of large NMR-invisible assemblies in exchange with NMR visible species [252, 282]. An NMR-dark state was detectable only in the dense fraction (Figure 5-3C), revealing that in the lean fraction all TFE present is visible by NMR, while in the dense fraction TFE broadened by the high protein concentration exists in exchange with TFE involved in even larger assemblies which are NMR invisible. Importantly, despite the presence of this NMR-dark state, the TFE signal in the dense fraction is easily observable and quantifiable, making it a good reporter signal.

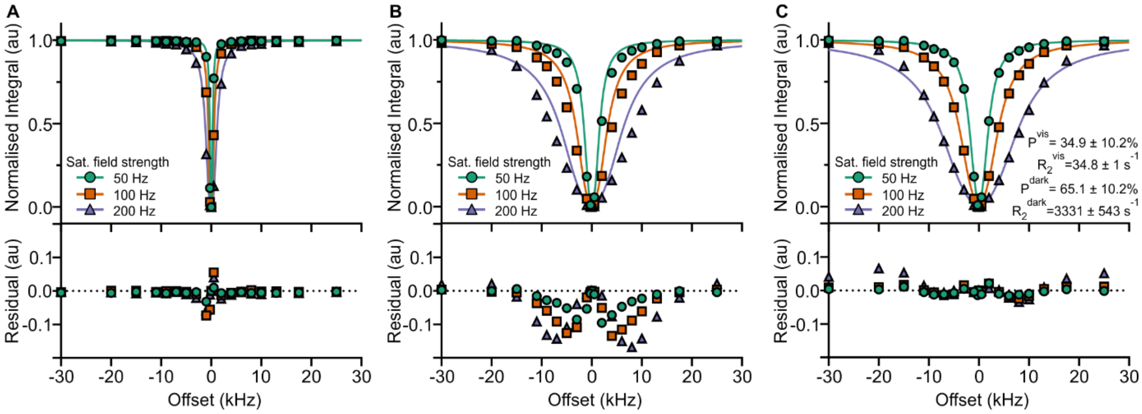

Figure 5-3. Detection and quantification of TFE in an NMR dark-state at 20°C. DEST profiles for the isolated (**A**) lean and (**B**) dense fractions, with curves fitted to the Bloch-McConnell model in the absence of an NMR dark-state with $R_2^{obs} = R_2^{vis}$. (C) DEST profile for the dense fractions with curves fitted to the model for two-state exchange between an NMR visible and an NMR dark state. R_2^{obs} in lean fraction used as R_2^{vis} in the dense fraction. Residuals plotted on bottom of all three plots. DEST profiles were fitted with an in-house MATLAB script.

5.4.3 Tracking fast kinetics of LLPS through bulk-detection NMR

As the lean and dense fractions give rise to distinctive TFE NMR signals, we next explored how NMR can be used to track the development of these phases during the course of LLPS. Here, 200 mg/mL BSA with 20 mM YCl_3 was subjected to temperature jumps from 25°C to 40, 45 or 50°C, with the rate of LLPS changing significantly with increasing temperatures. At the lower two temperatures, BSA underwent macroscopic LLPS with complete layer separation, while at 50°C the solution became extremely opalescent, but without subsequent layer separation, suggesting an arrested phase transition (Figure S5-3).

For the initial faster kinetics of LLPS preceding layer separation, bulk-detection NMR was used to observe evolution of the TFE probe signal, and thus the different phases, throughout the sample (Figure 5-4). Following the temperature jump trigger, the initial single peak develops into two overlapping species, a narrower upfield peak with a broader downfield shoulder. These species are in good agreement with the TFE signals observed in isolated fractions, with the broad shoulder originating from the dense phase, and the narrow peak originating from the lean phase. Additionally, the chemical shifts, widths and intensities of the species continue to evolve over time, indicating changes in the composition of the two phases during LLPS.

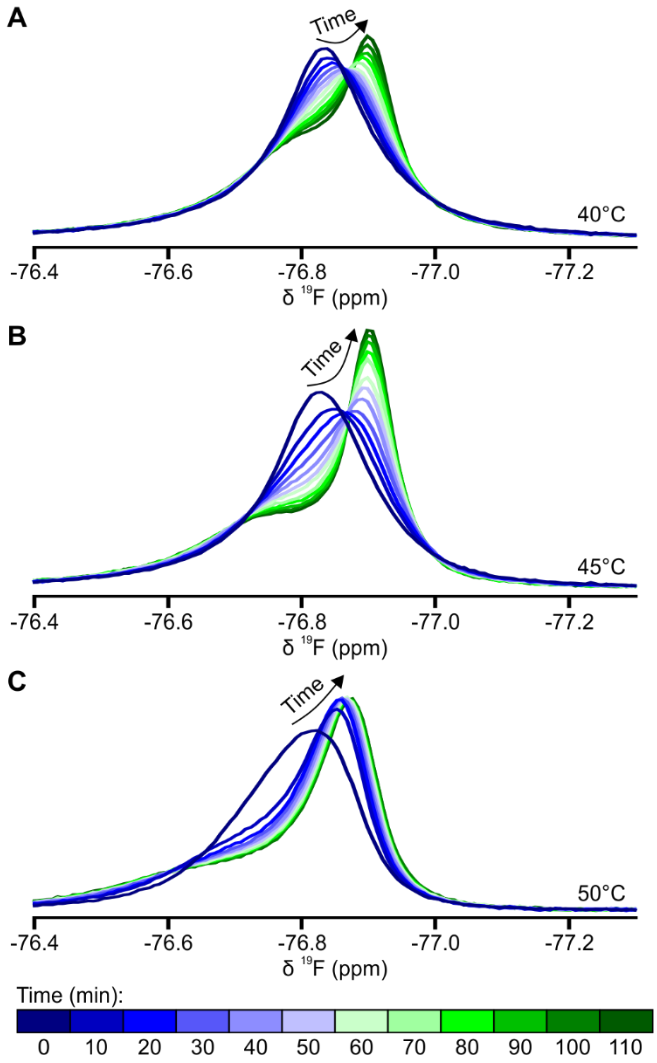

Figure 5-4. Examples of bulk-detected ^{19}F NMR spectra of TFE in BSA undergoing microscopic LLPS at different temperatures following a temperature jump. Spectra at 40°C (**A**), 45°C (**B**) and 50°C (**C**). The representative spectra shown here are sampled at 10 minute intervals, from t=0 to 110 minutes.

To quantify the process of LLPS, TFE probe signals were deconvoluted (Figure S5-4), revealing two emerging and evolving components, one with lower and another with higher characteristic concentration (Figure S5-5). As TFE chemical shift is linearly sensitive to BSA concentration (Figure 5-1A), this enabled determination of the concentrations of the two evolving species, while the fraction of total TFE signal in each environment reports on the apparent volumes of the two species present in the observed sample volume (Figure 5-5). For LLPS at 40°C and 45°C, the predominant component, the lean species, initially reflects the 200 mg/mL starting solution (Figure 5-5A&C), while the second component reflects a very highly concentrated but very low population species, likely an aggregated state (Figure 5-5B&D). As LLPS proceeds, the concentration and volume of the lean species decreases due to depletion of the initial solution, until its concentration approaches that of the final lean phase. Conversely, the apparent volume of the dense species increases from nearly zero, while its apparent concentration initially drops, as it becomes representative of the dense phase rather than the aggregated state. Beyond a certain point (90 min at 40°C and 30 min at 45°C) the apparent concentration of the dense species starts to increase, until it reaches stable concentration characteristic of the dense phase. For the temperature jump to 50°C, LLPS is so rapid such that the equilibrium, and dense and lean phases, are formed after 20 min, reaching the arrested state mentioned earlier (Figure S5-3B).

The rate of LLPS markedly differs with temperature, with higher temperatures resulting in semi-equilibrium being reached faster. Additionally, the concentration of the dense phase after 120 minutes was also higher at higher temperatures, while the lean phase concentration was very similar at all three temperatures. Conversely, the volume of the dense phase decreases with temperature (Figure 5-5B), such that the final mass of protein in each phase is broadly similar at all three temperatures (Figure 5-5E-F). Importantly, at all temperatures, the total calculated protein mass in the observed sample volume remains largely constant and is in good agreement with the expected protein mass (Figure 5-5G). This analysis therefore allows one to measure how the concentration and effective volume of each phase evolves with time, in a temperature-dependent manner, and quantitatively track the initial process of suspended phases emerging throughout the sample (i.e. microscopic phase separation).

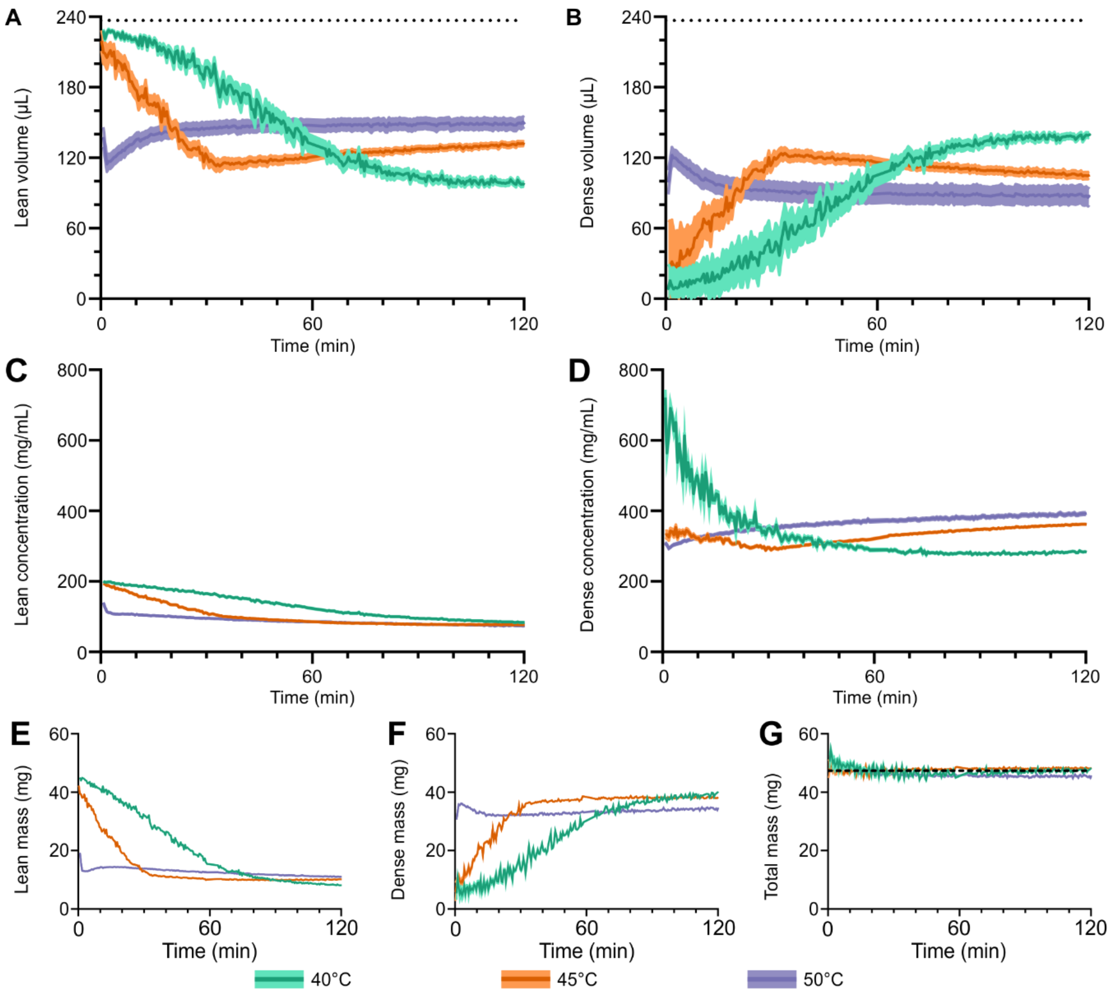

Figure 5-5. Fast kinetics of BSA LLPS at different temperatures as characterised by bulk-detected NMR. (**A-B**) Apparent volumes of the lean phase and high concentration, respectively, in the observed sample volume. Volumes were calculated based on deconvoluted integrals of the TFE signals and the known total observed volume (236.8 µL) marked by dotted lines. (**C-D**) Concentrations of the lean and dense phases, respectively. Concentrations were calculated based on deconvoluted peak chemical shifts and protein concentration calibration curve. (**E-F**) Mass of BSA in the lean and dense phases, respectively, present in the observed sample volume. Masses calculated from the apparent volumes and concentrations of each phase. (**G**) Total mass in the observed volume, based on calculated mass in the lean and dense phases. Dashed line indicates the expected total mass in the observed volume (47.36 mg). For all plots, dark line plots are the calculated values, while the lighter shaded regions represent 95% confidence intervals. Individual data points represent independent deconvolution results for different time points collected at 0.5 minute intervals.

5.4.4 Tracking slower kinetics of layer separation by bulk-detection and spatially-selective NMR

In some systems, LLPS may proceed beyond a suspension of dense droplets and instead exhibit macroscopic LLPS, with the droplets settling into a lower dense layer with a discrete boundary to an upper lean layer. Therefore, we next extended our experimental approach to study this process of layer separation. Here, the BSA solution previously observed undergoing LLPS at 40°C was monitored for an extended time period, catching both fast and slow kinetics (Figure 5-6). After 145 min, the TFE probe exhibited marked changes in behaviour, with a rapid increase in the apparent volume of the dense phase in the observed volume (Figure 5-6A). This was accompanied by an increase in the apparent total mass in the observed volume (Figure 5-6C), without significant increase in dense phase concentration (Figure 5-6B). These observations arise from layer separation resulting in a significant redistribution of protein across the entire sample volume, with the position of the NMR observed volume mainly capturing the dense layer towards the bottom of the tube (Figure S5-3A). Accompanying layer separation, the TFT reference exhibited signs of magnetic field inhomogeneity resulting from the protein solution, with altered lineshape leading to reduction in signal intensity and increases in signal width (Figure 5-6D). Remarkably, the magnitude of the changes in TFT lineshape are very small compared to the broader TFE signal, such that inhomogeneity in this instance does not significantly affect interpretation of the TFE probe signals.

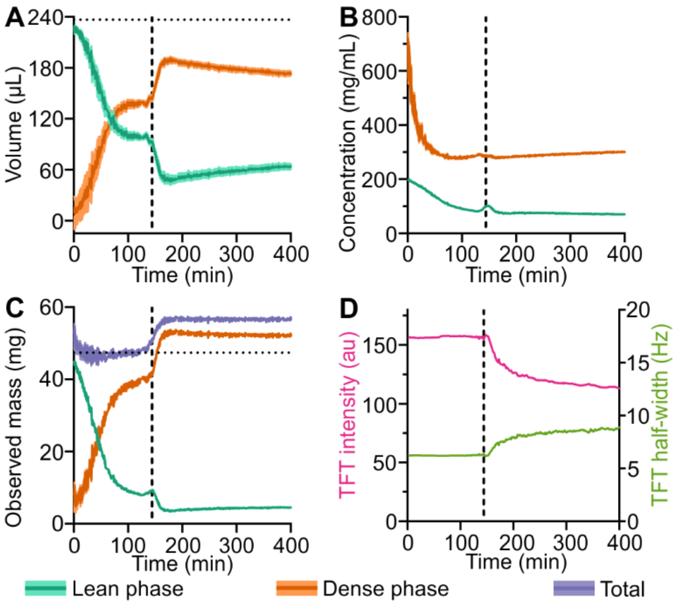

Figure 5-6. Kinetics of LLPS and layer separation of BSA at 40°C characterised by bulk-detection NMR. (**A**) Apparent volume of the lean and dense phases. Dotted horizontal line indicates the observed sample volume (236.8 µL). (**B**) Concentration of the lean and dense phases. (**C**) Apparent mass of BSA in the NMR-observed sample volume. Dotted horizontal line indicates the expected total mass in the observed volume in the absence of any layer separation (47.36 mg). (**D**) TFT reference peak intensity (pink, left axis) and half-width (green, right axis). Dashed vertical line at 140 minutes on all plots indicates the onset of layer separation.

As layer separation leads to differences in phase distribution across the BSA solution, we next investigated the use of spatially-selective NMR to examine this process in greater detail. Spatially-selective NMR enables signals from a specific horizontal slice of the sample to be collected. Due to non-linearity of the gradient coils required for spatially-selective NMR, the total observable sample length (12 mm / 130.1 µL) is less than for bulk-detected NMR (22 mm / 238.6 µL) allowing observation of the central part of the sample (Figure S5-1 & Figure S5-2).

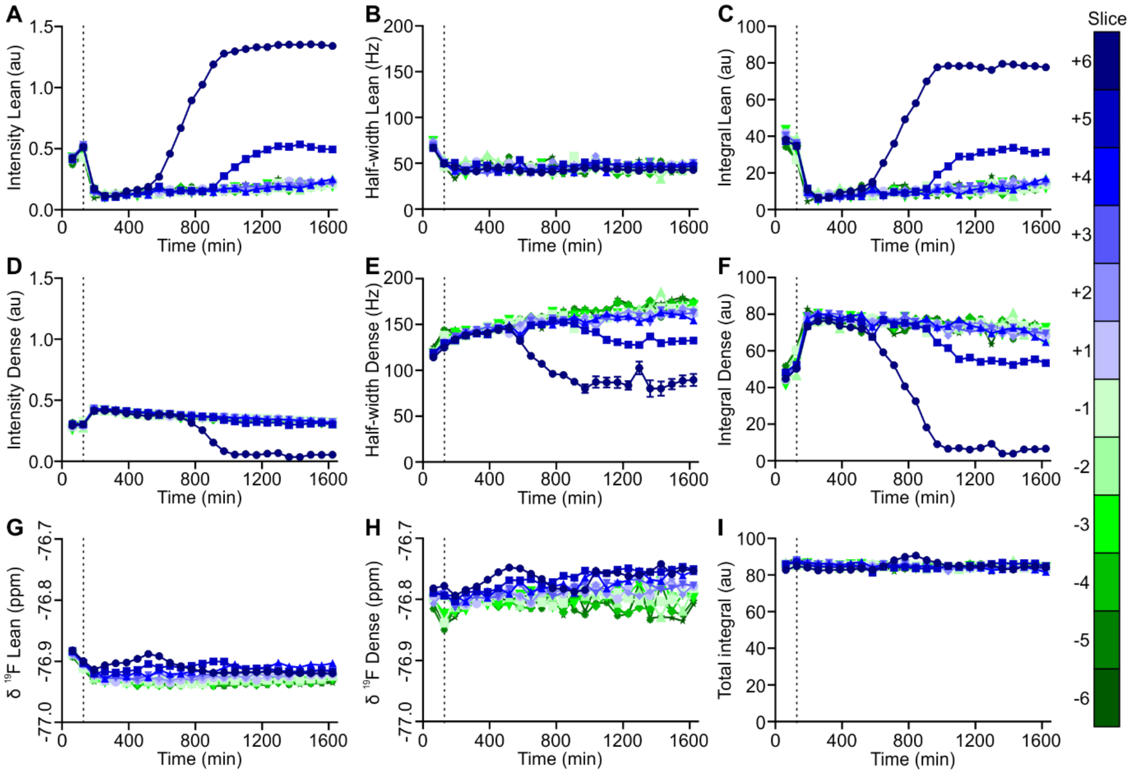

Figure 5-7. Slow kinetics of BSA LLPS at 40°C as characterised by spatially-selective NMR. Deconvoluted parameters for the TFE lean phase signal intensity (**A**), half-width

(**B**), integral (**C**), and chemical shift (**G**). Deconvoluted parameters for the TFE dense phase signal intensity (**D**), half-width (**E**), integral (**F**), and chemical shift (**H**). (**I)** Total TFE signal integral. Dashed vertical lines denote the onset of layer separation at 140 minutes, with fast initial kinetics preceding this time, and slower kinetics after this time.

During microscopic LLPS but before layer separation, the two phases occur uniformly across the sample, with spatially-selective NMR (Figure 5-7, first two data points) in good agreement with bulk-detection NMR (Figure 5-5). However, after the onset of layer separation at 140 min (dotted vertical line, as judged by bulk-detected NMR above), the entire volume of all observed slices quickly becomes dominated by the dense phase, which settles down from the top of the sample to fill up the observed volume. However, a small residual volume of lean phase remains mixed in these slices, indicating that the layer separation is incomplete and that the boundary between the two layers is likely a moving diffuse boundary. After 500 min, lean phase is observed increasing in the top slice (+6) until it is the only phase present in this slice after 900 min (Figure 5-7C). This indicates the boundary between the two layers shifting downwards as further settling of the dense phase occurs. After 900 min, the boundary is observed moving through the next slice (+5), before plateauing as the layer separation reaches an apparent equilibrium, suggesting the formation of a sharp boundary (Figure 5-7C). Analysis of the boundary position shows that the boundary sinks at a rate of 0.154 mm/hr (Figure S5-6). Together these data show that the TFE probe allows one to monitor the entire process of LLPS, from the onset and evolution of the phase transition, through to layer separation and settling, revealing the kinetics and complexities of LLPS.

5.5 Discussion

Phase transitions are seismic events, with the properties of the medium often changing discontinuously and abruptly, and with the kinetics of this process depending on a complex balance of parameters. The importance of LLPS in biology and biotechnology has been recognised recently [136, 182], but further experimental techniques are needed to characterise this elusive phenomenon. The nature of protein LLPS makes it a challenging process to study by biophysical techniques, including solution NMR spectroscopy. While conventional high-resolution NMR experiments may be applied under idealised conditions preceding LLPS, or with small amounts of dense droplets suspended in solution, or in isolated fractions [238, 250, 333], applying such techniques to studying the *process* of LLPS itself has thus far remained extremely challenging. Here, an alternative approach, employing a fluorinated probe molecule with bulk-detection and spatially-selective NMR analysis, is demonstrated as a unique tool to fully characterise the whole process and kinetics of microscopic and macroscopic protein LLPS.

Using a fluorinated molecule which transiently interacts with protein molecules as an NMR probe offers a number of advantages over assessing signals from proteins or other macromolecules themselves [336]. Firstly, fluorine spectra do not suffer from overlapping background signals from biological molecules. Secondly, small molecules have inherently better NMR signal properties than nuclei in proteins, including narrower lineshapes and stronger signal intensities, meaning that their signals are detectable even under challenging conditions, such as in the dense phase, or when recording spectra from a small slice during spatially-selective NMR. Finally, signals from probe molecules may be recorded with a few scans, allowing observations of kinetics at faster timescales. Other small molecules, such as sodium ions in ^{23}Na NMR or ammonium ions in ^{14}N NMR [337, 338], have been shown to have potential uses as NMR probes for studying biological condensates or macromolecular assemblies.

Here, the linear sensitivity of the ^{19}F chemical shift of TFE to protein concentration is key to detecting and studying the evolution of the phases during LLPS. However, a significantly different chemical shift is required in the two phases, particularly for spectral deconvolution, meaning that our experimental approach is best suited to systems where the dense and lean phases have markedly different protein concentrations and thus markedly different TFE ^{19}F chemical shifts. Although TFE is known to stabilise protein alpha helices [339, 340], the concentration employed here (0.1% v/v) is significantly beneath that expected to perturb protein conformation and thus LLPS behaviour. Alongside the fluorinated probe, another fluorinated molecule in a coaxial insert acts as an excellent external reference [341], and enables observation of magnetic field inhomogeneity without the complication of the reference solution itself undergoing LLPS. The coaxial insert is also crucial for housing deuterated solvent for field-frequency lock, thereby avoiding addition of $^{2}H_2O$ directly to the protein solution, which is known to alter the LLPS propensity of proteins [161, 342].

During microscopic LLPS, evolution of the TFE probe signal in bulk-detection NMR experiments reports on evolution of the lean and dense phases throughout the sample. Despite the presence of these two phases resulting in a heterogeneous solution, magnetic field homogeneity, as judged by TFT signal lineshape, is remarkably unperturbed during initial phase separation. After the onset of layer separation, field homogeneity degrades, although in this instance, the additional broadening of the TFE signal is very small compared to its linewidth. Spatially-selective NMR meanwhile reports on the distribution of the phases across the sample, particularly upon layer separation. Spatially-selective NMR detection is increasingly recognised as a powerful approach to study a range of complex phenomenon by NMR [263, 343, 344], and is possible in all modern NMR spectrometers with Z-gradient coils. It may also be applied to study individual layers in a heterogeneous sample after layer separation, without the need for further sample handling which may affect the equilibrium states. Spatially-selective NMR has previously been used to study liquid-liquid interfaces [345, 346] and phase separation in oil mixtures [261], but to our knowledge has not been applied to protein LLPS.

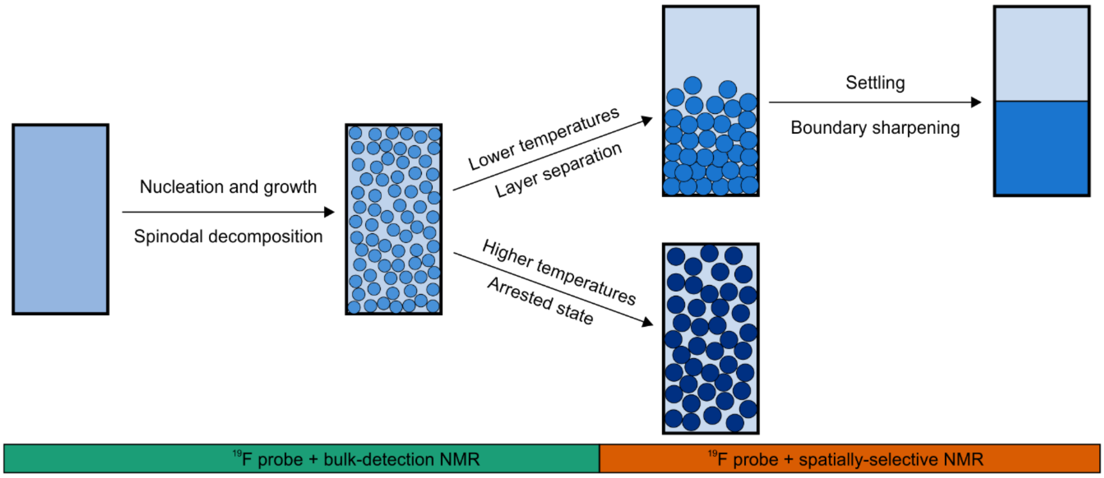

Figure 5-8. Schematic of types of BSA phase separation observed at different temperatures by bulk-detection and spatially-selective NMR. The initially homogenous solution undergoes phase separation by nucleation and growth, or spinodal decomposition. At 50°C, phase separation is arrested and a gel-like solution formed. At lower temperatures, phase separation progresses to layer separation, with this process and boundary sharpening characterised by spatially-selective NMR.

In this work, BSA served as a model system for protein LLPS, undergoing the transition with a lower critical solution temperature (LCST) in the presence of YCl_3. Previous studies have examined the process of BSA LLPS by neutron/X-ray scattering [170], but have been limited to the initial phase transition preceding layer separation. Kinetics of phase separation have previously been widely studied in polymer and colloidal systems [135, 347], and the BSA LLPS observed here concurs with the classical theories of LLPS derived from these experiments (Figure 5-8). The relatively slow phase separation observed at 40°C suggests a metastable phase transition with dense phase evolution by nucleation and growth [134], whereas the rapid phase separation at 50°C is consistent with spinodal decomposition. Additionally at 50°C, the arrested phase separation concurs with previous observations of arrested phase transitions in BSA at higher temperatures [170] and in other model proteins [348], with the TFE NMR signals here indicating a lean state of 60 mg/mL BSA interpenetrating a glassy state of ≈400 mg/mL.

5.6 Conclusion

This combination of bulk-detection and spatially-selective analysis, with a fluorinated probe molecule, is uniquely suited to studying the dynamic processes of phase and layer separation by NMR spectroscopy. The ability to monitor the evolution, particularly the concentration and volume, of both phases simultaneously *in situ*, with temporal and spatial resolution, makes this approach well-suited to studying the effects of different factors on the composition of the phases and the kinetics of LLPS. Finally, in systems undergoing layer separation, spatially-selective NMR enables tracking of the distribution of the phases and layers throughout the solution. This method of monitoring LLPS kinetics may also be applicable in other model systems, such as intrinsically disordered proteins, where the effect of amino acid substitutions or inclusion of RNA cofactors on LLPS propensity could be investigated [248, 349].

5.7 Acknowledgements

J.E.B. was supported by CASE DTP PhD studentship BB/M011208/1 from the UK Biotechnology and Biological Sciences Research Council (BBSRC) in partnership with AstraZeneca UK. We are grateful to Adrian Podmore and Stephanie Davies for valuable discussions, and to Matthew Cliff for assistance with spatially-selective NMR pulse programming.

5.8 Supporting Information

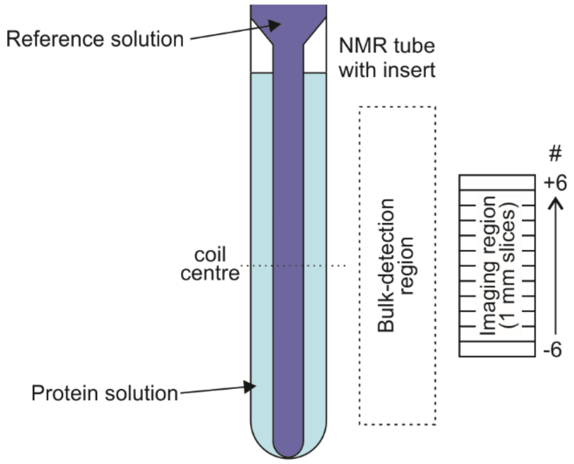

Figure S5-1. Schematic of NMR tube and NMR detection volumes. Protein solution (blue) with TFE probe molecule in standard 5 mm NMR tube, with reference solution (purple) with TFT in DMSO-d6 in coaxial insert inserted into the tube. Imaging region (12 mm length) for spatially-selective NMR in the centre of the bulk-detection region (22 mm). Not to scale.

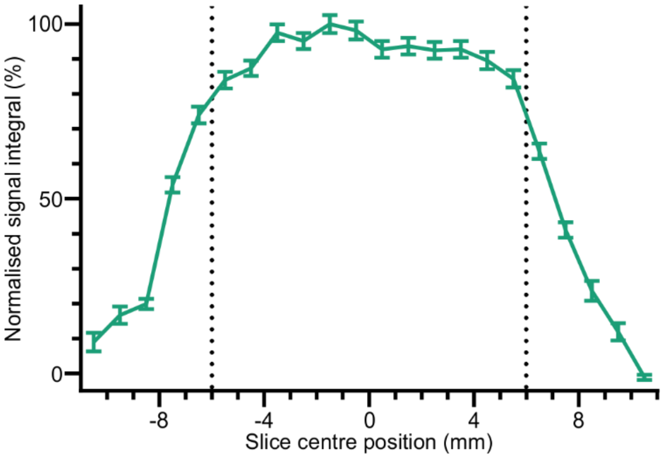

Figure S5-2. Effect of slice centre position on spatially-selective NMR signal integrals. Slice centre position relative to the centre of the gradient coils (e.g. 0 Hz offset). 1 mm slices, centred at 0.5 mm intervals, with positive values above the coil centre, and negative values beneath the coil centre. Area between the dotted lines represents the region used here in spatially-selective experiments. Outside of this central region, signal integrals falls rapidly (due to non-linearity of the gradient coils) to beneath acceptable levels, particularly when combined with the significantly reduced signal from the small slices.

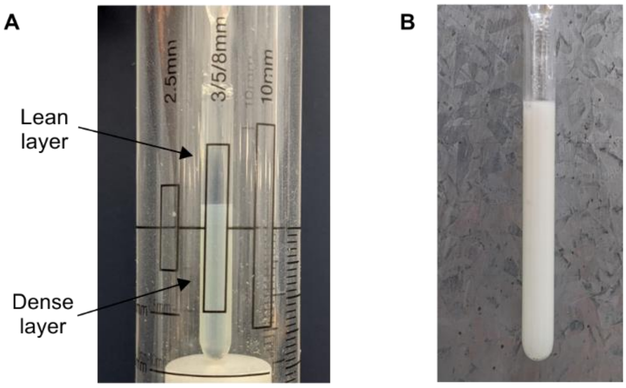

Figure S5-3. Appearance of phase-separated BSA solutions after incubation at 40°C and 50°C. (**A**) Layer separation after incubation at 40°C. Scale from NMR tube depth gauge (1 mm intervals visible on the right-hand side). (**B**) Arrested state after incubation at 50°C. Solutions were incubated for >18 hours, with image taken at room temperature immediately after removal from NMR spectrometer. Appearance of this arrested state was unchanged by cooling, or prolonged refrigerated storage.

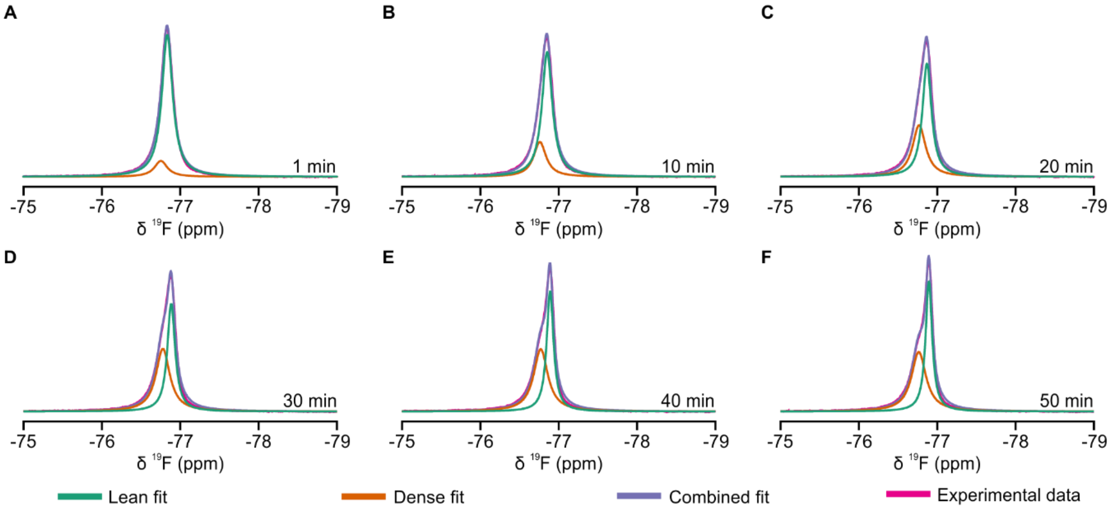

Figure S5-4. Examples of spectral deconvolution of the TFE ^{19}F NMR signal following LLPS at 45°C. Deconvoluted bulk-detected ^{19}F NMR spectra of TFE in BSA at (**A**) 1 min, (**B**), 10 min, (**C**) 20 min, (**D**) 30 min, (**E**) 40 min, and (**F**) 50 min after the temperature jump triggering LLPS. Experimental data (pink) fitted to two Lorentzian lineshapes representing the lean (teal) and dense (orange) phases, with the sum of these two lineshapes as the total combined fit (purple).

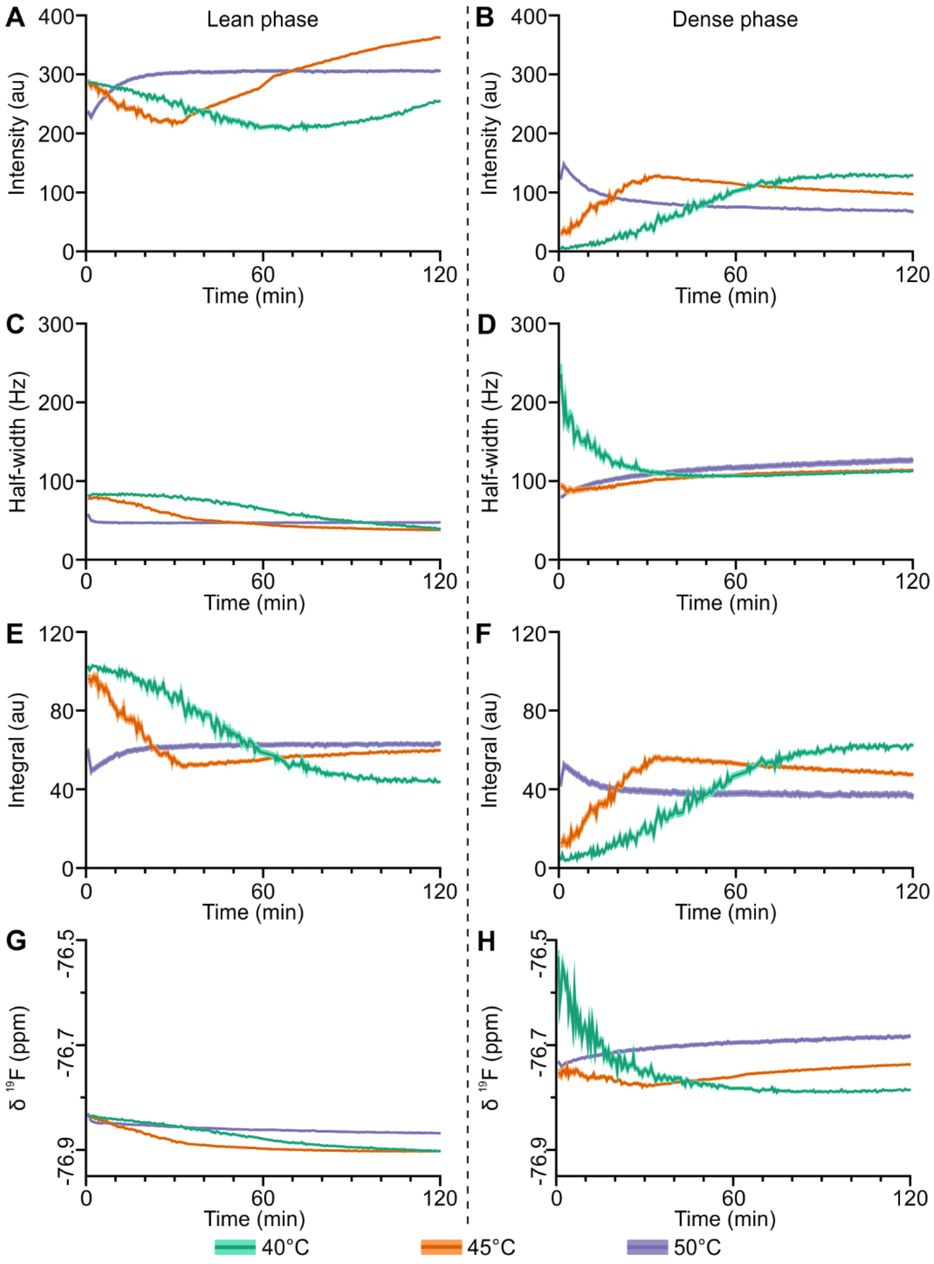

Figure S5-5. Time dependence of deconvoluted TFE signal parameters from BSA LLPS at different temperatures. Left and right columns correspond to lean and dense phases, respectively. (**A**-**B**) TFE signal intensity. (**C**-**D**) Signal half-width. (**E**-**F**) Signal integral. (**G**-**H**) Signal chemical shift. For all plots, line plots are the calculated values, while the shaded regions represent 95% confidence intervals.

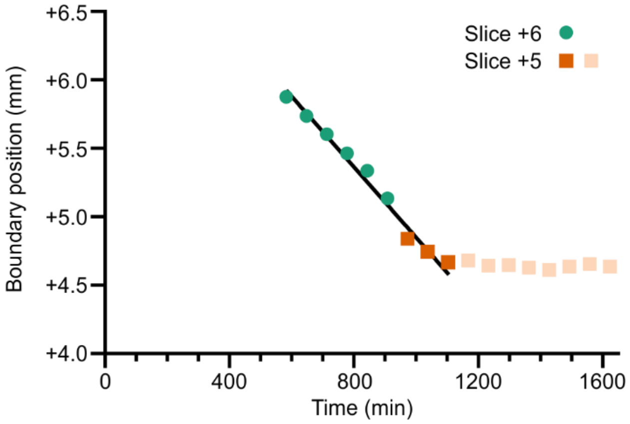

Figure S5-6. Determination of boundary position and sedimentation rate by spatially-selective NMR. Following entry of the lean layer into the spatially-selective detection volume after 500 min, the vertical position of the boundary between the two layers ($Z_{boundary}$) can be determined based on the fraction of dense phase ($Fraction_{Dense}$) in each slice: $\boldsymbol{Z_{boundary} = Z_{slice\ bottom} + (Fraction_{Dense}\ x\ 1)}$, where $Z_{slice\ bottom}$ is the position of the bottom of each slice, and 1 is the height of each slice (in mm). Linear fit to time dependence of the boundary position within slices #+6 and #+5 (solid line fitted to dark-coloured points) gives a sedimentation rate of 0.154 mm/hr, with light orange points representing the settled boundary position at +4.6 mm in slice #+5.

6 Characterisation of liquid-liquid phase separation in an antibody biopharmaceutical by ^{19}F NMR spectroscopy

This chapter was prepared for submission as a research paper:

Jack E. Bramham[1], Adrian Podmore[2], Stephanie A. Davies[2], and Alexander P. Golovanov[1]

[1] Manchester Institute of Biotechnology and School of Chemistry, Faculty of Science and Engineering, The University of Manchester, Manchester, M1 7DN, UK
[2] Dosage Form Design & Development, BioPharmaceuticals Development, R&D, AstraZeneca, Cambridge, CB21 6GH, UK

Author contributions:

J.E.B. performed experiments, analysed the data, and drafted the manuscript. A.P. and S.A.D. supplied the mAb and provided guidance and supervision from an industrial perspective. A.P.G. conceived and supervised the project and provided input regarding data analysis.

6.1 Abstract

Liquid-liquid phase separation (LLPS) is an increasingly observed phenomenon in antibody biopharmaceuticals. Biopharmaceutical LLPS may be an unwanted instability or present an alternative means to concentrate protein solutions. We have recently demonstrated a novel approach to study protein LLPS using a fluorinated probe molecule in combination with spatially-selective and conventional bulk detection NMR. Here, we show that this approach is also applicable to characterising the process of LLPS in a biopharmaceutical monoclonal antibody (mAb). Adaptation of the experimental process enables bulk-detection NMR to capture the rapid mAb LLPS, while diffusion and relaxation measurements report on the properties of the isolated lean and dense fractions. Antibody LLPS displays particularly complex behaviour, with the appearance of a transient intermediate species during the initial phase separation. Further characterising the pathway of mAb LLPS may provide insights into how to control mAb phase separation behaviour.

6.2 Introduction

The advancement of high concentration biopharmaceutical formulations (>100 mg/mL) for subcutaneous injection has resulted in increased observations of instabilities arising from protein self-association, including increased viscosity and liquid-liquid phase separation (LLPS) [76, 136, 140]. During LLPS, a medium concentration solutions separates into two distinct phases, a high concentration dense phase and a low concentration lean phase. This may occur as dense droplets suspended throughout a lean phase (microscopic phase separation) [141, 143, 155], or proceed to macroscopic phase separation with a dense layer beneath a lean layer [140, 143, 144, 146]. LLPS is also an increasingly recognised phenomenon in cell biology, where it is associated with both regular and aberrant cellular processes [183, 323, 350].

In biopharmaceuticals, LLPS is typically considered as an unwanted physical instability, with a number of strategies in development to prevent its occurrence, including addition of excipients to formulations [59, 147, 155, 351] and protein engineering approaches [157, 194, 352]. However, LLPS may also represent an alternative method to concentrate protein solutions and achieve the required higher concentrations (i.e. for subcutaneous administration of a reduced volume) [136].

Therefore, a deeper understanding of the process and behaviour of antibody phase separation is needed.

We have recently demonstrated a new approach to characterise the process of LLPS in proteins using a fluorinated probe molecule, trifluoroethanol (TFE), and ^{19}F nuclear magnetic resonance (NMR) spectroscopy. The probe molecule is sensitive to local protein concentration and its ^{19}F NMR signal reports on the evolution of the lean and dense phases during LLPS. Meanwhile, a coaxial insert with trifluorotoluene (TFT) in deuterated solvent acts as an external reference and field frequency lock, without adulteration of the protein solution.

Here, we demonstrate that this NMR approach is applicable to a model biopharmaceutical mAb, and can be used to characterise its LLPS in detail. We show that TFE is sensitive to the local protein concentration of the mAb, COE-13, which undergoes LLPS at refrigerated temperatures in the presence of NaCl at pH 5.5 [147]. Tracking of the kinetics of mAb LLPS at different temperatures reveals complex solution behaviour, with the presence of transient intermediate states during LLPS at 8 and 4°C. Additionally, we show that our approach can be optimised for cases when LLPS occurs rapidly upon a temperature jump, with the TFT external reference enabling correction for these temperature changes. This greater understanding of the behaviour of mAb LLPS may benefit efforts to understand how to control mAb LLPS.

6.3 Materials and Methods

6.3.1 Sample preparation

A mAb, COE-13 (MW 149 kDa, pI 8.1 – 8.6), known to be prone to LLPS under specific conditions [147], was supplied by AstraZeneca. 20 mM acetate buffer (sodium acetate trihydrate (Sigma-Aldrich) and glacial acetic acid (Fisher Chemical)), pH 5.5, was prepared fresh as required. Concentrated NaCl (Fisher) was also prepared in buffer. Solutions were filtered with 0.2 µm syringe filters (Minisart SFCA, Sartorius) or 0.22 µm membrane filters (GSWP, Merck Millipore). Protein concentrations were determined by absorbance at 280 nm using a NanoDrop One (Thermo Scientific).

COE-13 was dialysed into acetate buffer using GeBAflex-Maxi dialysis tubes (3 ml, 30 kDa MWCO, Generon), and concentrated using a centrifugal concentrator (30 kDa MWCO, Amicon). For LLPS experiments, 80 mg/mL COE-13 in 20 mM acetate buffer, pH 5.5, was supplemented with 75 mM NaCl and 10 mM TFE (Sigma-Aldrich). For NMR experiments examining LLPS *in situ*, 480 µL solution was pipetted into an NMR tube, with the coaxial insert inserted prior to LLPS. For NMR experiments involving bulk assessment of the individual layers, 1 mL protein solution was pipetted into an NMR tube, with LLPS and layer separation triggered in the tube by incubation at 4°C for 48 hours. After centrifugation with a hand crank tube centrifuge, the lean layer was then transferred to another tube. Finally, the residual lean layer and a small volume of the dense layer was discarded. Coaxial inserts were then inserted into the NMR tubes.

6.3.2 NMR spectroscopy

NMR experiments were conducted using a Bruker 500 MHz (470 MHz for ^{19}F) Avance III spectrometer with a QCI-F cryoprobe with cooled ^{1}H and ^{19}F channels, sample temperature control unit, and Z-gradient coils. Solutions containing 10 mM TFE probe (Sigma-Aldrich) were placed in standard 5 mm O.D. NMR tubes (Wilmad), with coaxial inserts (50 mm stem length, Wilmad) containing deuterated methanol (methanol-d_4) (99.8%, Sigma-Aldrich) for lock and 100 mM α,α,α-trifluorotoluene (TFT) (Sigma-Aldrich) as an external reference. For all experiments, NMR tubes were positioned so that the centre of the sample volume aligned with the centre of the NMR probe coil region. Magnetic field shimming was performed on the initial homogenous sample, with no further shimming during kinetics experiments.

1D ^{19}F NMR spectra were recorded with ^{1}H decoupling, using the *zgig* Bruker pulse sequence. ^{19}F NMR kinetic experiments were acquired in a pseudo-2D fashion, with the *zg2d* Bruker pulse sequence adapted to include ^{1}H decoupling. Kinetics experiments were recorded with a single scan and no dummy scans to minimise experimental dead time. All NMR spectra were initially processed in Topspin 4.0.8 (Bruker) with spectra plotted in Prism 8 (GraphPad). When required, peak deconvolution was performed using in-house MATLAB scripts with nonlinear least-squares fitting. TFT peaks were fitted to a single Lorentzian lineshape. TFE signals were fitted to two or three mixed Gaussian-Lorentzian lineshapes (1:1 Gaussian:Lorentzian mixture).

6.3.3 Relaxation and diffusion

^{19}F transverse relaxation times (T_2) were measured with a version of the Bruker Carr-Purcell-Meiboom-Gill (CPMG) sequence with perfect echo. CPMG echo time and repeats were altered to suit individual experimental conditions. Translational diffusion coefficients (D_L) were determined by diffusion ordered spectroscopy (DOSY) using the simulated echo pulse-field gradient (PFG) pulse sequence *stebpgp1s*. DOSY delays were optimised for each experimental condition, with diffusion times of 1200 and 1700 ms, and gradient lengths of 0.8 and 0.6 ms for the lean and dense fractions, respectively. T_2 and D_L were calculated in Dynamics Center 2.5 (Bruker).

6.4 Results

6.4.1 TFE is sensitive to local mAb concentration

We have previously observed that the ^{19}F NMR signal of TFE is sensitive to local protein concentration in bovine serum albumin (BSA), displaying increased linewidth and linear chemical shift perturbations with increasing protein concentration. To determine if this is also the case for the mAb COE-13, a calibration series with increasing protein concentration was performed (Figure 6-1). TFE exhibited linear chemical shift perturbations with increasing COE-13 concentration (Figure 6-1A), although the magnitude of the perturbation was smaller than previously observed for BSA. Furthermore, TFE line width was narrow in COE-13 and constant (within experimental error) with increasing concentration. While these observations indicate that the apparent interaction between TFE and the mAb is weaker than that previously observed between TFE and BSA, TFE may still be suitable as a probe molecule for monitoring the changes in local concentrations of COE-13, and hence for studies of its LLPS.

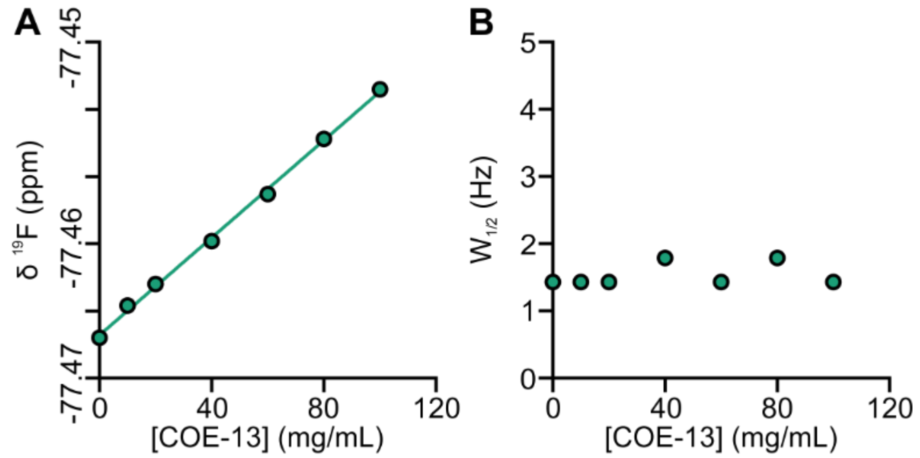

Figure 6-1. Effect of increasing mAb concentration on TFE ^{19}F NMR signal. (**A**) TFE ^{19}F NMR chemical shift, with linear fit. (**B**) TFE signal line width. Parameters recorded with ^{1}H decoupling. Acquired at 4°C in acetate buffer, pH 5.5 without NaCl.

6.4.2 TFE behaviour in isolated lean and dense fractions

To ascertain if the dense and lean fractions of COE-13 give rise to distinct TFE ^{19}F NMR signals, LLPS was triggered in 80 mg/mL COE-13 with 10 mM TFE by addition of 75 mM NaCl and incubation at 4°C for 48 hours. The resulting dense (170 mg/mL) and lean (10 mg/mL) layers were separated and each isolated fraction examined by bulk-detection NMR (Figure 6-2).

The TFE ^{19}F NMR signals in the lean and dense fractions are distinct, with the lean fraction signal appearing upfield of the dense fraction signal (Figure 6-2A). This chemical shift separation is constant at all temperatures tested (Figure 6-2B), and is consistent with the calibration curve established previously (Figure 6-1A). TFE line width is very similar in both fractions (Figure 6-2C), again in agreement with observations from the calibration curve.

The transverse relaxation rate (R_2) and translational diffusion coefficient (D_L) of the probe molecule provides insights into the solution properties of the two fractions. Here, TFE R_2 is higher in the dense fraction than in the lean fraction, although generally still relatively slow, while TFE D_L is slower in the dense fraction. This indicates that self-association and viscosity are higher in the dense fraction, as expected. Despite this increased viscosity, the probe molecule yields a sharp and easily-detected signal, enabling assessment of highly-concentrated solution even at low temperatures. The changes in R_2 and D_L with increasing temperatures are expected and are explained by decreasing water viscosity (Figure 6-2E&F).

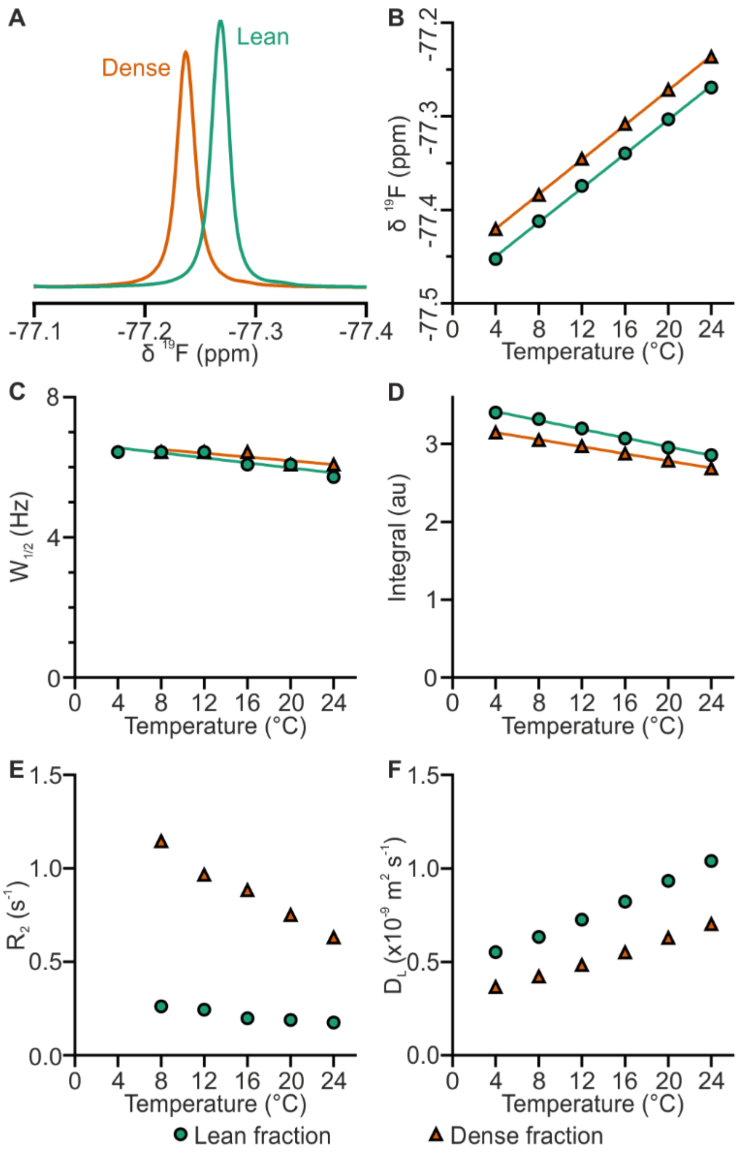

Figure 6-2. Behaviour of the isolated dense and lean fractions as a function of temperature. (**A**) ^{19}F NMR spectra of TFE in the isolated fractions at 24°C. TFE ^{19}F chemical shift (**B**), half-width (**C**) and integral (**D**) as function of temperature. TFE transverse relaxation rate (R_2) (**E**) and translational diffusion coefficient (D_L) (**F**) as a function of temperature.

In COE-13, no NMR dark-states were detected by ^{19}F Dark-state Exchange Saturation Transfer (DEST) in either fraction (data not shown), in line with the slow R_2 and apparent lack of significantly strong interaction between TFE and the mAb. However, this does not entirely preclude the existence of large NMR-invisible mAb species, which may exist in an exchange regime inaccessible to TFE and ^{19}F DEST.

6.4.3 Kinetics of COE-13 LLPS

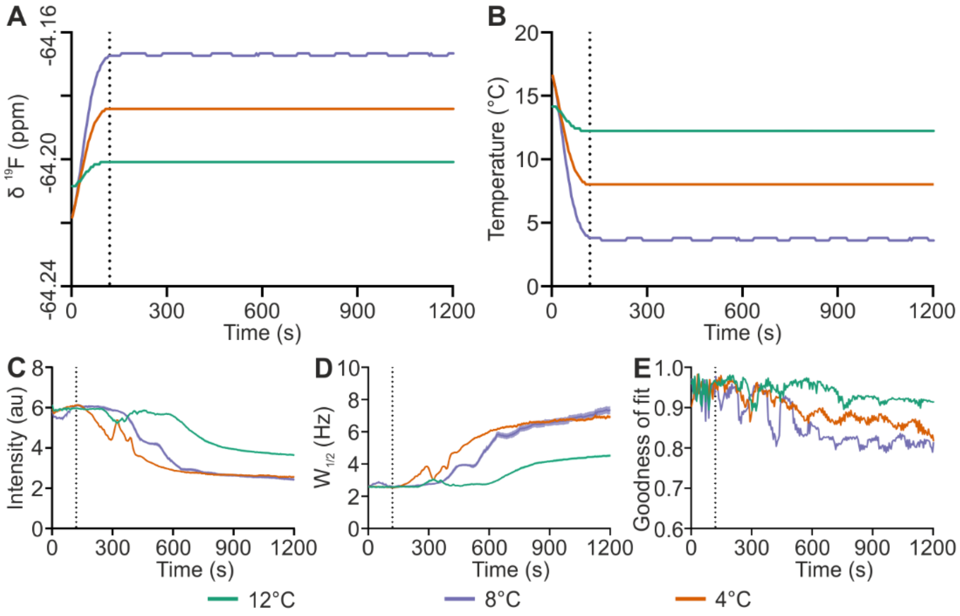

Figure 6-3. Behaviour of the TFT external reference following temperature jumps. (**A**) Chemical shift of the TFT ^{19}F NMR signal. (**B**) Actual temperature of the sample determined from the TFT ^{19}F chemical shift. Intensity (**C**) and half-width (**D**) of a single Lorentzian fitted to the TFT ^{19}F signal. (**E**) Goodness of fit (normalised root-mean-square error) for the Lorentzian fitted to the TFT signal. Dotted line at 120 s indicates point of actual temperature equilibration to the set temperatures.

Having established that the TFE probe has distinct characteristic ^{19}F NMR signals in the dense and lean fractions, we next characterised the kinetics of COE-13 phase separation by conventional bulk-detection NMR following temperature jumps from 16°C to 12, 8, and 4°C. Here, COE-13 LLPS was significantly faster than BSA LLPS studied previously, requiring an adapted experimental approach. 1D NMR spectra were collected in a single scan at 5 s intervals, with data acquisition started immediately after the initiation of the temperature jump, and with no dummy scans to minimise experimental dead time. To account for the effect of temperature on TFE chemical shift during the initial temperature equilibration, the chemical shift of the external reference molecule TFT was used to determine the actual sample temperature (Figure 6-3A&B) based on the calibration curve (Figure S6-1). At all three set temperatures, sample temperature equilibration was achieved within 120 s. The TFT ^{19}F NMR signal also acts as indicator of magnetic field homogeneity (Figure 6-3C-E). Significant inhomogeneity in the protein solution, such as the formation of two distinct layers, results in magnetic field inhomogeneity and distortion of the TFT reference signal lineshape. At all three temperatures, field homogeneity was relatively unperturbed within the first 300 s, before showing greater perturbations beyond this point, with the onset of these perturbations indicating the initiation of layer separation.

Examining the response of the TFE probe NMR signal to the temperature jumps reveals the complex behaviour of the mAb during the initial stages of LLPS (Figure 6-4). Here, TFE ^{19}F chemical shifts were corrected to account for the effect of temperature during the initial temperature equilibration based on the determined sample temperature (Figure 6-3B) and calibration curves (Figure S6-1). At 12°C, the TFE reporter signal initially evolves into two apparent distinct species, a downfield high concentration species and an upfield low concentration species. Meanwhile, at 8 and 4°C (Figure 6-4B&C), TFE signal behaviour is more complex with the appearance of two upfield signals characteristic of two distinct lower concentration species. Notably, these multiple species are present before field homogeneity deteriorates, meaning they are not artefacts of field inhomogeneity. Furthermore, at lower temperatures, the rate of the evolution of the TFE signals is faster.

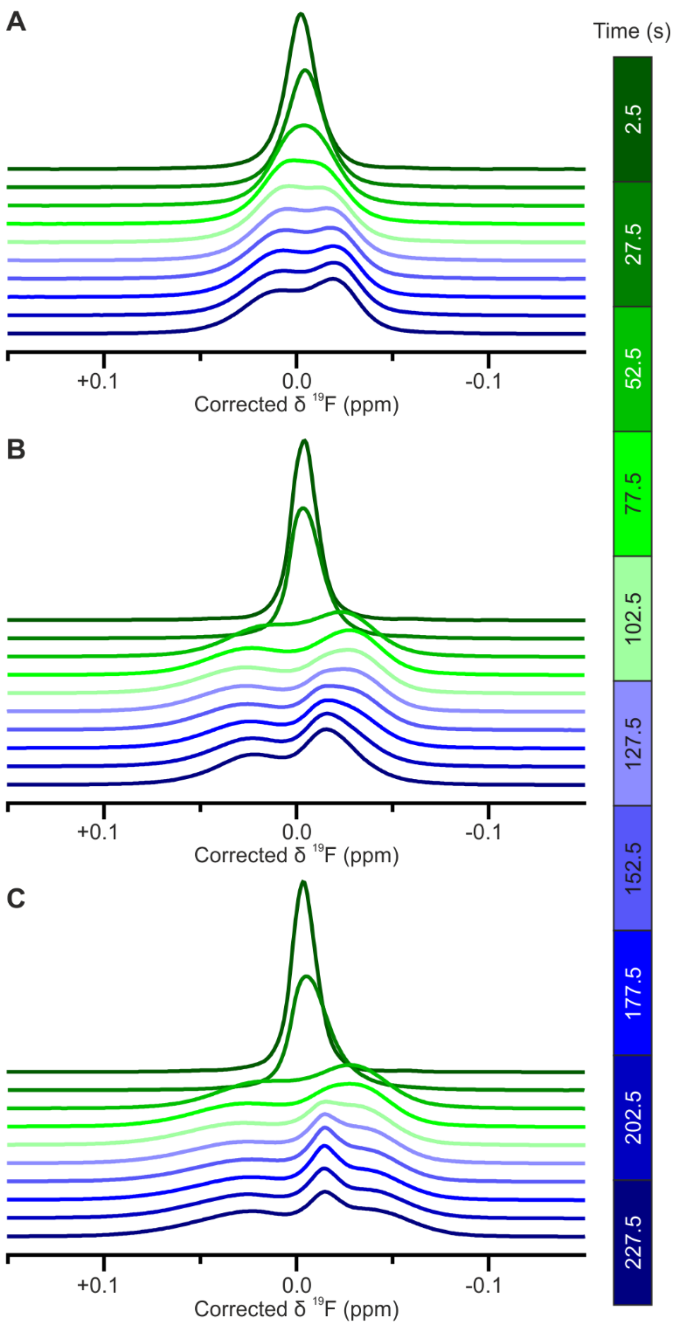

Figure 6-4. Examples of bulk-detected ^{19}F NMR spectra of TFE in COE-13 during the initial process of phase separation. Spectra at set temperatures of 12°C (**A**), 8°C (**B**) and 4°C (**C**). The representative spectra shown here are sampled at 25 s intervals from t=2.5 to 227.5 s. Chemical shifts corrected based on expected TFE chemical shift at the measured sample temperature.

To understand the behaviour of the mAb solution further, TFE signals were deconvoluted to two or three mixed Lorentzian-Gaussian lineshapes. However, given the magnitude of the magnetic field distortions observed above (Figure 6-3) and the inherently narrow TFE signal in the mAb solutions, complete deconvolution without artefacts arising from field inhomogeneity was not possible, and reliable individual signal intensities could not be obtained. Therefore, only the chemical shifts of the different TFE species are reported here. At 12°C, mAb LLPS preceded via two states, a lower concentration species which evolves into the final lean phase, and a higher concentration species which evolves into the final dense species (Figure 6-5A).

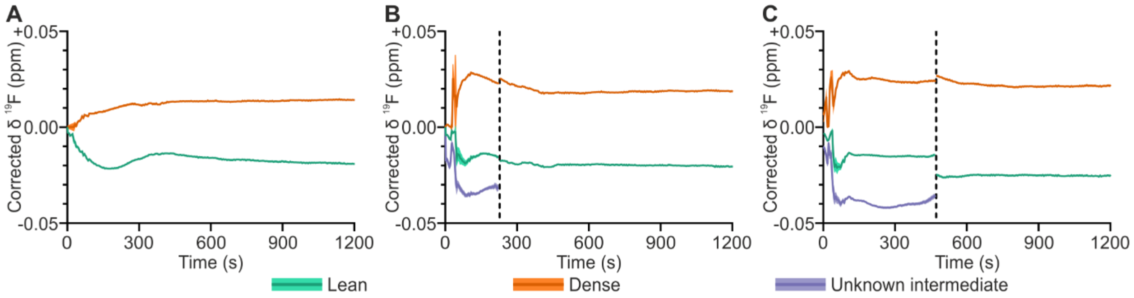

Figure 6-5. Kinetics of COE-13 phase separation as determined by bulk-detection NMR. Deconvoluted species corrected chemical shifts at 12°C (**A**), 8°C (**B**), and 4°C (**C**). At 12°C, spectra were fitted to two states. At 8°C and 4°C, spectra were initially fitted to three states (before dashed vertical line), then two states as the lean species and intermediate converged. Positive chemical shifts indicate an apparent greater mAb concentration.

Conversely at 8°C and 4°C, mAb LLPS evolved through three species, a single higher concentration species and two lower concentration species (Figure 6-5B&C). One of the lower concentration species appears similar to the evolution of the lean species at 12°C, while the other appears to be a transient intermediate species. The chemical shift and apparent signal linewidth of this transient species is not immediately explainable, but it may arise from a protein and NaCl depleted state undergoing some form of intermediate exchange. The two lower concentration species converge to the final lean species, with this occurring faster at 8°C than at 4°C. Additionally, the chemical shift difference between the final dense and lean species is greater at lower temperatures, indicating greater mAb self-association and a greater difference in concentrations between the fractions at lower temperatures.

6.5 Discussion

Characterising the process and kinetics of phase separation in protein solutions is important to understanding how and why LLPS occurs, and to develop strategies to control its occurrence [136]. In this study, we show that the fluorinated probe molecule TFE in conjunction with bulk-detected NMR spectroscopy can be used to study LLPS of a biopharmaceutical mAb.

Here, the behaviour of the TFE probe NMR signal in COE-13 was slightly different to that observed previously in BSA. While TFE displayed linear chemical shift perturbations with increasing protein concentration for both proteins, the effect was smaller in COE-13 (Figure 6-1). Additionally, the linewidth of TFE in COE-13 was fairly insensitive to protein concentration, with the isolated lean and dense fractions producing similar relatively narrow TFE signals. These observations suggest that the TFE-protein interaction is weaker for COE-13 than for BSA, and may explain the lack of dark-state detected in the dense fraction by ^{19}F DEST NMR. However, the chemical shift sensitivity is sufficient to enable spectral deconvolution and characterisation of the process of COE-13 LLPS by bulk-detection NMR. This suggests that this NMR approach may be applicable to a wide range of proteins, but highlights that the probe behaviour should be well characterised in each individual system, and concentration calibration curves obtained.

COE-13 LLPS was also significantly faster than BSA LLPS previously studied using this NMR approach. However, adaptation of the experimental procedure, such as acquiring single-scan ^{19}F NMR spectra in a series, enabled us to capture the faster kinetics of mAb LLPS on a second-time scale. The TFT reference is also critical here as it enables actual sample temperature determination during temperature equilibration (Figure 6-3), and thus enables the rapid transition of the TFE to two/three states during temperature jumps to set temperatures of 8 and 4°C to be understood (Figure 6-5). The approach may potentially be extended further through the use of reference deconvolution to reduce the effects of magnetic field inhomogeneity arising from layer separation [353].

The kinetics of biopharmaceutical mAb LLPS have previously been studied using a temperature controlled capillary tube and dark-field microscopy [354], with COE-13

LLPS here occurring on similar time scales (within 10 minutes). However, COE-13 did not display an arrested phase transition or gel state during our studies, although this may occur at lower temperatures, potentially beneath the freezing point. Additionally, the detection of the third transient intermediate state by ^{19}F NMR is unexpected, and the identity and nature of this third TFE species requires further investigation.

6.6 Conclusion

In this preliminary study, we have demonstrated that our NMR approach with a fluorinated probe molecule can be used to study mAb LLPS, with the potential to characterise the kinetics and intermediates of phase separation in great detail. Adaptation of our approach enables kinetics to be studied on a faster time scale, which may be particularly beneficial during studies of other protein systems.

6.7 Acknowledgements

J.E.B. was supported by CASE DTP PhD studentship BB/M011208/1 from the UK Biotechnology and Biological Sciences Research Council (BBSRC) in partnership with AstraZeneca UK. We are grateful to Matthew Cliff for valuable NMR spectroscopy discussions.

6.8 Supporting Information

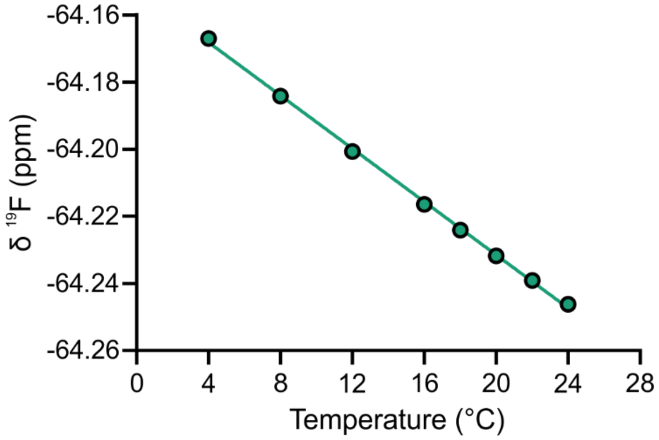

Figure S6-1. Calibration curve for temperature determination from TFT external reference chemical shift. Linear fit to experimental data.

7 General conclusions and future outlook

Self-association and particularly LLPS are generally challenging to study, especially in large unlabelled proteins such as mAbs. Therefore, the main aim of this Thesis was to develop new NMR approaches to study the stability and LLPS of antibody biopharmaceuticals by NMR spectroscopy. We initially focused on using ^{1}H NMR to assess mAbs formulations, before developing ^{19}F NMR methods to characterise self-association and LLPS in mAbs and a model protein (BSA).

In Chapter 2, we demonstrated that ^{1}H NMR spectroscopy can be used to study the degradation of both the protein and small molecule components of mAb formulations *in situ* at high concentration. Stability of both components is critical to the overall efficacy and safety of a biopharmaceutical product, but characterising protein stability typically requires sample manipulation, such as dilution or salt removal, which may perturb protein structure and behaviour. Furthermore, stability of small molecule components is an often overlooked factor during formulation studies. Here, we show that changes in NMR signal intensities and transverse relaxation rates in mAb spectral regions can be used to detect protein degradation, with T_2 particularly sensitive to mAb fragmentation. Degradation of small molecule formulation components, including sucrose and histidine, was also detected as changes in NMR spectra, including appearance of new signals, chemical shift perturbations, and changes in signal intensities. ^{1}H NMR spectroscopy is particularly well suited to studying small molecules in formulations due to their fast tumbling and generally high concentrations resulting in narrow intense NMR signals. This approach may be especially applicable to study so called ‘sacrificial’ excipients, such as antioxidants like methionine, which are believed to undergo degradation in order to prevent mAb degradation.

In Chapter 3, we investigated how LLPS can be used as an alternative method to concentrate mAb solutions. Filtration techniques with membranes are typically used to concentrate protein solutions, but achievable protein concentrations may be limited by high viscosity causing membrane fouling and reduced filtration. While LLPS has previously been suggested as a method to concentrate protein solutions, questions remained about the stability of, and self-association present in the resulting high-concentration solutions. Here, we employed a typical model formulation approach, namely addition of an excipient (Arg·Glu) to the phase separated dense fraction, as a strategy to improve the properties of a protein solution concentrated by LLPS. The protein concentration achieved in the dense fraction (170 mg/mL) was in principle sufficient for a high-concentration protein formulation, and it may be possible to reach even higher concentrations by optimisation of the LLPS conditions. Importantly, Arg·Glu reduced viscosity of the dense fraction, prevented further LLPS from occurring, and reduced mAb degradation, particularly aggregation. This suggests that a conventional formulation screening approach could be used to identify excipients to optimise the behaviour and properties of the dense fraction further.

In the second half of the thesis, we demonstrated the potential of ^{19}F NMR spectroscopy to study protein self-association and LLPS. In Chapter 4, we demonstrated the use of the Dark-state Exchange Saturation Transfer (DEST) NMR technique to study protein clustering in a mixture of mAbs covalently labelled with ^{19}F tags. When protein self-association or clustering results in an NMR invisible dark state, DEST enables detection and quantification of this state. This is particularly applicable in large proteins, such as mAbs, where slow tumbling results in rapid relaxation and broad signals even for monomeric species. Additionally, due to the different tags on each mAb in the mixture, the specific clustering of each mAb and its response to changes in solution conditions, such as the addition of excipients or salts, was observed. While it is difficult to study mixtures of proteins by conventional biophysical techniques, there is increasing interest in the co-formulation of multiple mAbs, and approaches similar to the one employed here may be used in the future to characterise such systems.

In Chapter 5, we developed a novel experimental approach to study LLPS in protein solutions using a fluorinated probe molecule (TFE) alongside bulk-detection and spatially-selective NMR. Using a small molecule as a probe which transiently interacts with the protein enabled rapid acquisition of informative signals, even from the highly viscous dense phase. Critically for our approach, TFE chemical shift and linewidth are sensitive to protein concentration, resulting in the lean and dense phases producing different NMR signals. By monitoring these different signals simultaneously, the evolution of the lean and dense phases can be observed and characterised. Here, conventional bulk-detected NMR was well suited to observing the initial faster phase transition, while spatially-selective NMR uniquely allowed NMR to study layer separation and the distribution of the different phases throughout the sample. This enabled NMR to characterise the entire process of LLPS, from the initial rapid phase transition, i.e., microscopic phase separation, to the slow settling of the layers during layer separation, i.e, macroscopic phase separation. Spatially-selective NMR may be incorporated into conventional multidimensional protein NMR experiments, allowing these approaches to be used to assess individual layers, without sample manipulation and potential perturbation of equilibrium dynamics.

In Chapter 6, we showed that our new experimental approach can also be applied to study LLPS of mAbs. Here, mAb LLPS was significantly faster than BSA LLPS observed in Chapter 5, suggesting mAb LLPS occurred by spinodal decomposition. Additionally, the faster kinetics and reduced broadening of the TFE signal by the mAb required alterations to our experimental approach, including ^{1}H decoupling and rapid acquisition of kinetic data with a single scan. Furthermore, field inhomogeneity resulting from LLPS was a larger problem for the narrow TFE signals in the mAb solutions, yet TFE chemical shift still reported on the evolution of the concentration of the phases during LLPS. The distortions arising from field inhomogeneity may potentially be alleviated in future by application of reference deconvolution of NMR signals during processing [353]. Here, the mAb exhibited complex transient phase behaviour, particularly at 4 and 8°C with the initial presence of three distinct TFE signals, reflecting three distinct mAb species with different characteristic concentration, which further evolved into two species, dense and lean. The nature of the third transient species discovered in these mAb solutions remains to be characterised, but it may reflect a kinetic intermediate present for these complex molecules. Understanding the nature of this intermediate may enable better control of LLPS, to either prevent LLPS to achieve enhanced formulation stability, or to promote LLPS as means to concentrate mAbs.

In conclusion, we have detailed a number of approaches in this Thesis which enable NMR spectroscopy to investigate a range of phenomena in mAb and protein solutions. ^{1}H NMR can be used to study degradation in mAb formulations, while ^{19}F DEST can be used to characterise protein clustering and self-association. Whilst NMR is currently underutilised in the biopharmaceutical industry, these approaches, along with other NMR techniques, such as spectral fingerprinting [278] and methods to identify chemical modifications [226, 228], may encourage greater adoption of the technique in industry.

The range of further possible NMR experiments mean that it may be used to study a magnitude of common biopharmaceutical development problems, all the way from lead identification and characterisation, to manufacturing of the final product. Finally, we demonstrated that a fluorinated probe along with bulk-detection and spatially-selective NMR is uniquely suited to characterise protein phase and layer separation. In combination with conventional high-resolution protein NMR, this approach enables all aspects of LLPS to be comprehensively characterised by NMR spectroscopy, and may be employed in the flourishing field studying phase separation in cell biology.

8 References

1. Wilson, R.M. and S.J. Danishefsky, *Small molecule natural products in the discovery of therapeutic agents: the synthesis connection.* J Org Chem, 2006. **71**(22): p. 8329-51.
2. Rader, R.A., *(Re)defining biopharmaceutical.* Nat Biotechnol, 2008. **26**(7): p. 743-51.
3. Goeddel, D.V., D.G. Kleid, F. Bolivar, H.L. Heyneker, D.G. Yansura, R. Crea, T. Hirose, A. Kraszewski, K. Itakura, and A.D. Riggs, *Expression in Escherichia coli of chemically synthesized genes for human insulin.* Proc Natl Acad Sci U S A, 1979. **76**(1): p. 106-10.
4. Walsh, G., *Biopharmaceutical benchmarks 2018.* Nat Biotechnol, 2018. **36**(12): p. 1136-1145.
5. IMS. *Global Medicines Use in 2020 - Outlook and Implications*. 2015 22/11/2015]; Available from: http://www.imshealth.com/en/thought-leadership/ims-institute/reports/global-medicines-use-in-2020.
6. Oo, C. and S.S. Kalbag, *Leveraging the attributes of biologics and small molecules, and releasing the bottlenecks: a new wave of revolution in drug development.* Expert Rev Clin Pharmacol, 2016. **9**(6): p. 747-9.
7. Smith, A.J., *New horizons in therapeutic antibody discovery: opportunities and challenges versus small-molecule therapeutics.* J Biomol Screen, 2015. **20**(4): p. 437-53.
8. Gewirtz, D.A., M.L. Bristol, and J.C. Yalowich, *Toxicity issues in cancer drug development.* Curr Opin Investig Drugs, 2010. **11**(6): p. 612-4.
9. Kidane, A. and P.P. Bhatt, *Recent advances in small molecule drug delivery.* Curr Opin Chem Biol, 2005. **9**(4): p. 347-51.
10. Scherrmann, J.M., *Drug delivery to brain via the blood-brain barrier.* Vascul Pharmacol, 2002. **38**(6): p. 349-54.
11. Forthal, D.N., *Functions of Antibodies.* Microbiol Spectr, 2014. **2**(4): p. 1-17.
12. Klasse, P.J., *Neutralization of Virus Infectivity by Antibodies: Old Problems in New Perspectives.* Adv Biol, 2014. **2014**: p. 24.
13. Sarma, J.V. and P.A. Ward, *The complement system.* Cell Tissue Res, 2011. **343**(1): p. 227-35.
14. Liu, H. and K. May, *Disulfide bond structures of IgG molecules: structural variations, chemical modifications and possible impacts to stability and biological function.* MAbs, 2012. **4**(1): p. 17-23.
15. Sela-Culang, I., V. Kunik, and Y. Ofran, *The structural basis of antibody-antigen recognition.* Front Immunol, 2013. **4**: p. 302.
16. Hayes, J.M., M.R. Wormald, P.M. Rudd, and G.P. Davey, *Fc gamma receptors: glycobiology and therapeutic prospects.* J Inflamm Res, 2016. **9**: p. 209-219.
17. Ng, P.C. and Y. Osawa, *Preparation and characterization of the F (ab)2 fragments of an aromatase activity-suppressing monoclonal antibody.* Steroids, 1997. **62**(12): p. 776-81.
18. Schroeder, H.W., Jr. and L. Cavacini, *Structure and function of immunoglobulins.* J Allergy Clin Immunol, 2010. **125**(2 Suppl 2): p. S41-52.
19. Vidarsson, G., G. Dekkers, and T. Rispens, *IgG subclasses and allotypes: from structure to effector functions.* Front Immunol, 2014. **5**: p. 520.
20. Collins, A.M. and K.J. Jackson, *A Temporal Model of Human IgE and IgG Antibody Function.* Front Immunol, 2013. **4**: p. 235.

21. Ravetch, J.V. and S. Bolland, *IgG Fc receptors.* Annu Rev Immunol, 2001. **19**: p. 275-90.
22. Liu, J.K., *The history of monoclonal antibody development - Progress, remaining challenges and future innovations.* Ann Med Surg (Lond), 2014. **3**(4): p. 113-6.
23. Askonas, B.A., A.R. Williamson, and B.E. Wright, *Selection of a single antibody-forming cell clone and its propagation in syngeneic mice.* Proc Natl Acad Sci U S A, 1970. **67**(3): p. 1398-403.
24. Kohler, G. and C. Milstein, *Continuous cultures of fused cells secreting antibody of predefined specificity.* Nature, 1975. **256**(5517): p. 495-7.
25. Sgro, C., *Side-effects of a monoclonal antibody, muromonab CD3/orthoclone OKT3: bibliographic review.* Toxicology, 1995. **105**(1): p. 23-9.
26. Winter, G. and W.J. Harris, *Humanized antibodies.* Trends Pharmacol Sci, 1993. **14**(5): p. 139-43.
27. Houdebine, L.M., *Production of pharmaceutical proteins by transgenic animals.* Comp Immunol Microbiol Infect Dis, 2009. **32**(2): p. 107-21.
28. Clementi, N., N. Mancini, L. Solforosi, M. Castelli, M. Clementi, and R. Burioni, *Phage display-based strategies for cloning and optimization of monoclonal antibodies directed against human pathogens.* Int J Mol Sci, 2012. **13**(7): p. 8273-92.
29. Leavy, O., *Therapeutic antibodies: past, present and future.* Nat Rev Immunol, 2010. **10**(5): p. 297.
30. Lazar, G.A., W. Dang, S. Karki, O. Vafa, J.S. Peng, L. Hyun, C. Chan, H.S. Chung, A. Eivazi, S.C. Yoder, J. Vielmetter, D.F. Carmichael, R.J. Hayes, and B.I. Dahiyat, *Engineered antibody Fc variants with enhanced effector function.* Proc Natl Acad Sci U S A, 2006. **103**(11): p. 4005-10.
31. Dall'Acqua, W.F., P.A. Kiener, and H. Wu, *Properties of human IgG1s engineered for enhanced binding to the neonatal Fc receptor (FcRn).* J Biol Chem, 2006. **281**(33): p. 23514-24.
32. Igawa, T., H. Tsunoda, T. Tachibana, A. Maeda, F. Mimoto, C. Moriyama, M. Nanami, Y. Sekimori, Y. Nabuchi, Y. Aso, and K. Hattori, *Reduced elimination of IgG antibodies by engineering the variable region.* Protein Eng Des Sel, 2010. **23**(5): p. 385-92.
33. Goletz, C., T. Lischke, U. Harnack, P. Schiele, A. Danielczyk, J. Ruhmann, and S. Goletz, *Glyco-Engineered Anti-Human Programmed Death-Ligand 1 Antibody Mediates Stronger CD8 T Cell Activation Than Its Normal Glycosylated and Non-Glycosylated Counterparts.* Front Immunol, 2018. **9**: p. 1614.
34. Mossner, E., P. Brunker, S. Moser, U. Puntener, C. Schmidt, S. Herter, R. Grau, C. Gerdes, A. Nopora, E. van Puijenbroek, C. Ferrara, P. Sondermann, C. Jager, P. Strein, G. Fertig, T. Friess, C. Schull, S. Bauer, J. Dal Porto, C. Del Nagro, K. Dabbagh, M.J. Dyer, S. Poppema, C. Klein, and P. Umana, *Increasing the efficacy of CD20 antibody therapy through the engineering of a new type II anti-CD20 antibody with enhanced direct and immune effector cell-mediated B-cell cytotoxicity.* Blood, 2010. **115**(22): p. 4393-402.
35. Nelson, A.L., *Antibody fragments: hope and hype.* MAbs, 2010. **2**(1): p. 77-83.
36. Schiele, F., J. van Ryn, K. Canada, C. Newsome, E. Sepulveda, J. Park, H. Nar, and T. Litzenburger, *A specific antidote for dabigatran: functional and structural characterization.* Blood, 2013. **121**(18): p. 3554-62.
37. Ahmad, Z.A., S.K. Yeap, A.M. Ali, W.Y. Ho, N.B. Alitheen, and M. Hamid, *scFv antibody: principles and clinical application.* Clin Dev Immunol, 2012. **2012**: p. 980250.

38. Siontorou, C.G., *Nanobodies as novel agents for disease diagnosis and therapy.* Int J Nanomedicine, 2013. **8**: p. 4215-27.
39. Czajkowsky, D.M., J. Hu, Z. Shao, and R.J. Pleass, *Fc-fusion proteins: new developments and future perspectives.* EMBO Mol Med, 2012. **4**(10): p. 1015-28.
40. Sedykh, S.E., V.V. Prinz, V.N. Buneva, and G.A. Nevinsky, *Bispecific antibodies: design, therapy, perspectives.* Drug Des Devel Ther, 2018. **12**: p. 195-208.
41. Ruf, P. and H. Lindhofer, *Induction of a long-lasting antitumor immunity by a trifunctional bispecific antibody.* Blood, 2001. **98**(8): p. 2526-34.
42. Steinhardt, J.J., J. Guenaga, H.L. Turner, K. McKee, M.K. Louder, S. O'Dell, C.I. Chiang, L. Lei, A. Galkin, A.K. Andrianov, A.D.-R. N, R.T. Bailer, A.B. Ward, J.R. Mascola, and Y. Li, *Rational design of a trispecific antibody targeting the HIV-1 Env with elevated anti-viral activity.* Nat Commun, 2018. **9**(1): p. 877.
43. Chau, C.H., P.S. Steeg, and W.D. Figg, *Antibody-drug conjugates for cancer.* Lancet, 2019. **394**(10200): p. 793-804.
44. Scott, A.M., J.P. Allison, and J.D. Wolchok, *Monoclonal antibodies in cancer therapy.* Cancer Immun, 2012. **12**: p. 14.
45. Vigneron, N., *Human Tumor Antigens and Cancer Immunotherapy.* Biomed Res Int, 2015. **2015**: p. 948501.
46. Dougan, M., G. Dranoff, and S.K. Dougan, *Cancer Immunotherapy: Beyond Checkpoint Blockade.* Annual Review of Cancer Biology, 2019. **3**(1): p. 55-75.
47. Chan, A.C. and P.J. Carter, *Therapeutic antibodies for autoimmunity and inflammation.* Nat Rev Immunol, 2010. **10**(5): p. 301-16.
48. Yasunaga, M., *Antibody therapeutics and immunoregulation in cancer and autoimmune disease.* Semin Cancer Biol, 2020. **64**: p. 1-12.
49. Smilek, D.E., M.R. Ehlers, and G.T. Nepom, *Restoring the balance: immunotherapeutic combinations for autoimmune disease.* Dis Model Mech, 2014. **7**(5): p. 503-13.
50. Kaplon, H. and J.M. Reichert, *Antibodies to watch in 2019.* MAbs, 2019. **11**(2): p. 219-238.
51. Kaplon, H. and J.M. Reichert, *Antibodies to watch in 2018.* MAbs, 2018. **10**(2): p. 183-203.
52. Jostock, T., *Expression of Antibody in Mammalian Cells*, in *Antibody Expression and Production*, M. Al-Rubeai, Editor. 2011, Springer Netherlands: Dordrecht. p. 1-24.
53. Dhara, V.G., H.M. Naik, N.I. Majewska, and M.J. Betenbaugh, *Recombinant Antibody Production in CHO and NS0 Cells: Differences and Similarities.* BioDrugs, 2018. **32**(6): p. 571-584.
54. Jain, E. and A. Kumar, *Upstream processes in antibody production: evaluation of critical parameters.* Biotechnol Adv, 2008. **26**(1): p. 46-72.
55. Marichal-Gallardo, P.A. and M.M. Alvarez, *State-of-the-art in downstream processing of monoclonal antibodies: process trends in design and validation.* Biotechnol Prog, 2012. **28**(4): p. 899-916.
56. Hober, S., K. Nord, and M. Linhult, *Protein A chromatography for antibody purification.* J Chromatogr B Analyt Technol Biomed Life Sci, 2007. **848**(1): p. 40-7.
57. Liu, H.F., J. Ma, C. Winter, and R. Bayer, *Recovery and purification process development for monoclonal antibody production.* MAbs, 2010. **2**(5): p. 480-99.
58. Walchli, R., M. Ressurreicao, S. Vogg, F. Feidl, J. Angelo, X. Xu, S. Ghose, Z. Jian Li, X. Le Saout, J. Souquet, H. Broly, and M. Morbidelli, *Understanding mAb*

aggregation during low pH viral inactivation and subsequent neutralization. Biotechnol Bioeng, 2020. **117**(3): p. 687-700.

59. Luo, H., N. Lee, X. Wang, Y. Li, A. Schmelzer, A.K. Hunter, T. Pabst, and W.K. Wang, *Liquid-liquid phase separation causes high turbidity and pressure during low pH elution process in Protein A chromatography.* J Chromatogr A, 2017. **1488**: p. 57-67.
60. Lopez, E., N.E. Scott, B.D. Wines, P.M. Hogarth, A.K. Wheatley, S.J. Kent, and A.W. Chung, *Low pH Exposure During Immunoglobulin G Purification Methods Results in Aggregates That Avidly Bind Fcgamma Receptors: Implications for Measuring Fc Dependent Antibody Functions.* Front Immunol, 2019. **10**(2415): p. 2415.
61. Cui, Y., P. Cui, B. Chen, S. Li, and H. Guan, *Monoclonal antibodies: formulations of marketed products and recent advances in novel delivery system.* Drug Dev Ind Pharm, 2017. **43**(4): p. 519-530.
62. Ohtake, S., Y. Kita, and T. Arakawa, *Interactions of formulation excipients with proteins in solution and in the dried state.* Adv Drug Deliv Rev, 2011. **63**(13): p. 1053-73.
63. Pinco, R.G. and T.M. Sullivan, *Regulation of Pharmaceutical Excipients*, in *Excipient Development for Pharmaceutical, Biotechnology, and Drug Delivery Systems*, A. Katdare and M. Chaubal, Editors. 2006, CRC Press: New York. p. 37 - 50.
64. van Reis, R. and A. Zydney, *Membrane separations in biotechnology.* Curr Opin Biotechnol, 2001. **12**(2): p. 208-11.
65. Garidel, P., B. Pevestorf, and S. Bahrenburg, *Stability of buffer-free freeze-dried formulations: A feasibility study of a monoclonal antibody at high protein concentrations.* Eur J Pharm Biopharm, 2015. **97**(Pt A): p. 125-39.
66. Carpenter, J.F., B.S. Chang, W. Garzon-Rodriguez, and T.W. Randolph, *Rational Design of Stable Lyophilized Protein Formulations: Theory and Practice*, in *Rational Design of Stable Protein Formulations: Theory and Practice*, J.F. Carpenter and M.C. Manning, Editors. 2002, Springer US: Boston, MA. p. 109-133.
67. Jackisch, C., V. Muller, C. Maintz, S. Hell, and B. Ataseven, *Subcutaneous Administration of Monoclonal Antibodies in Oncology.* Geburtshilfe Frauenheilkd, 2014. **74**(4): p. 343-349.
68. Tetteh, E. and S. Morris, *Systematic review of drug administration costs and implications for biopharmaceutical manufacturing.* Appl Health Econ Health Policy, 2013. **11**(5): p. 445-56.
69. Keizer, R.J., A.D. Huitema, J.H. Schellens, and J.H. Beijnen, *Clinical pharmacokinetics of therapeutic monoclonal antibodies.* Clin Pharmacokinet, 2010. **49**(8): p. 493-507.
70. Carrillo-Conde, B.R., E. Brewer, A. Lowman, and N.A. Peppas, *Complexation Hydrogels as Oral Delivery Vehicles of Therapeutic Antibodies: An in Vitro and ex Vivo Evaluation of Antibody Stability and Bioactivity.* Ind Eng Chem Res, 2015. **54**(42): p. 10197-10205.
71. Park, K., I.C. Kwon, and K. Park, *Oral protein delivery: Current status and future prospect.* Reactive and Functional Polymers, 2011. **71**(3): p. 280-287.
72. Viola, M., J. Sequeira, R. Seica, F. Veiga, J. Serra, A.C. Santos, and A.J. Ribeiro, *Subcutaneous delivery of monoclonal antibodies: How do we get there?* J Control Release, 2018. **286**: p. 301-314.

73. Shah, R.B., M. Patel, D.M. Maahs, and V.N. Shah, *Insulin delivery methods: Past, present and future.* Int J Pharm Investig, 2016. **6**(1): p. 1-9.
74. Bittner, B., W. Richter, and J. Schmidt, *Subcutaneous Administration of Biotherapeutics: An Overview of Current Challenges and Opportunities.* BioDrugs, 2018. **32**(5): p. 425-440.
75. Mathaes, R., A. Koulov, S. Joerg, and H.C. Mahler, *Subcutaneous Injection Volume of Biopharmaceuticals-Pushing the Boundaries.* J Pharm Sci, 2016. **105**(8): p. 2255-9.
76. Garidel, P., A.B. Kuhn, L.V. Schafer, A.R. Karow-Zwick, and M. Blech, *High-concentration protein formulations: How high is high?* Eur J Pharm Biopharm, 2017. **119**: p. 353-360.
77. Padala, C., F. Jameel, N. Rathore, K. Gupta, and A. Sethuraman, *Impact of Uncontrolled vs Controlled Rate Freeze-Thaw Technologies on Process Performance and Product Quality.* PDA J Pharm Sci Technol, 2010. **64**(4): p. 290-8.
78. Topp, E.M., L. Zhang, H. Zhao, R.W. Payne, G.J. Evans, and M.C. Manning, *Chemical Instability in Peptide and Protein Pharmaceuticals*, in *Formulation and Process Development Strategies for Manufacturing Biopharmaceuticals*. 2010, John Wiley & Sons, Inc. p. 41-67.
79. Li, S., C. Schoneich, and R.T. Borchardt, *Chemical instability of protein pharmaceuticals: Mechanisms of oxidation and strategies for stabilization.* Biotechnol Bioeng, 1995. **48**(5): p. 490-500.
80. Cacia, J., R. Keck, L.G. Presta, and J. Frenz, *Isomerization of an aspartic acid residue in the complementarity-determining regions of a recombinant antibody to human IgE: identification and effect on binding affinity.* Biochemistry, 1996. **35**(6): p. 1897-903.
81. Nowak, C., A. Tiwari, and H. Liu, *Asparagine Deamidation in a Complementarity Determining Region of a Recombinant Monoclonal Antibody in Complex with Antigen.* Anal Chem, 2018. **90**(11): p. 6998-7003.
82. Moritz, B. and J.O. Stracke, *Assessment of disulfide and hinge modifications in monoclonal antibodies.* Electrophoresis, 2017. **38**(6): p. 769-785.
83. Liu, D., D. Ren, H. Huang, J. Dankberg, R. Rosenfeld, M.J. Cocco, L. Li, D.N. Brems, and R.L. Remmele, Jr., *Structure and stability changes of human IgG1 Fc as a consequence of methionine oxidation.* Biochemistry, 2008. **47**(18): p. 5088-100.
84. Harris, R.J., B. Kabakoff, F.D. Macchi, F.J. Shen, M. Kwong, J.D. Andya, S.J. Shire, N. Bjork, K. Totpal, and A.B. Chen, *Identification of multiple sources of charge heterogeneity in a recombinant antibody.* J Chromatogr B Biomed Sci Appl, 2001. **752**(2): p. 233-45.
85. Alam, M.E., G.V. Barnett, T.R. Slaney, C.G. Starr, T.K. Das, and P.M. Tessier, *Deamidation Can Compromise Antibody Colloidal Stability and Enhance Aggregation in a pH-Dependent Manner.* Mol Pharm, 2019. **16**(5): p. 1939-1949.
86. Banks, D.D., D.M. Hambly, J.L. Scavezze, C.C. Siska, N.L. Stackhouse, and H.S. Gadgil, *The effect of sucrose hydrolysis on the stability of protein therapeutics during accelerated formulation studies.* J Pharm Sci, 2009. **98**(12): p. 4501-10.
87. Jacobitz, A.W., A.B. Dykstra, C. Spahr, and N.J. Agrawal, *Effects of Buffer Composition on Site-Specific Glycation of Lysine Residues in Monoclonal Antibodies.* J Pharm Sci, 2020. **109**(1): p. 293-300.

88. Mo, J., R. Jin, Q. Yan, I. Sokolowska, M.J. Lewis, and P. Hu, *Quantitative analysis of glycation and its impact on antigen binding.* MAbs, 2018. **10**(3): p. 406-415.
89. Dion, M.Z., D. Leiske, V.K. Sharma, C.L. Zuch de Zafra, and C.M. Salisbury, *Mitigation of Oxidation in Therapeutic Antibody Formulations: a Biochemical Efficacy and Safety Evaluation of N-Acetyl-Tryptophan and L-Methionine.* Pharm Res, 2018. **35**(11): p. 222.
90. Zheng, J.Y. and L.J. Janis, *Influence of pH, buffer species, and storage temperature on physicochemical stability of a humanized monoclonal antibody LA298.* Int J Pharm, 2006. **308**(1-2): p. 46-51.
91. Mahler, H.C., W. Friess, U. Grauschopf, and S. Kiese, *Protein aggregation: pathways, induction factors and analysis.* J Pharm Sci, 2009. **98**(9): p. 2909-34.
92. Fischer, S., J. Hoernschemeyer, and H.C. Mahler, *Glycation during storage and administration of monoclonal antibody formulations.* Eur J Pharm Biopharm, 2008. **70**(1): p. 42-50.
93. Qiu, H., R. Wei, J. Jaworski, E. Boudanova, H. Hughes, S. VanPatten, A. Lund, J. Day, Y. Zhou, T. McSherry, C.Q. Pan, and R. Sendak, *Engineering an anti-CD52 antibody for enhanced deamidation stability.* MAbs, 2019. **11**(7): p. 1266-1275.
94. Kayser, V., N. Chennamsetty, V. Voynov, B. Helk, and B.L. Trout, *Conformational stability and aggregation of therapeutic monoclonal antibodies studied with ANS and Thioflavin T binding.* MAbs, 2011. **3**(4): p. 408-11.
95. Garidel, P., A. Blume, and M. Wagner, *Prediction of colloidal stability of high concentration protein formulations.* Pharm Dev Technol, 2015. **20**(3): p. 367-74.
96. Caflisch, A., *Computational models for the prediction of polypeptide aggregation propensity.* Curr Opin Chem Biol, 2006. **10**(5): p. 437-44.
97. Andrews, J.M. and C.J. Roberts, *Non-native aggregation of alpha-chymotrypsinogen occurs through nucleation and growth with competing nucleus sizes and negative activation energies.* Biochemistry, 2007. **46**(25): p. 7558-71.
98. Brummitt, R.K., D.P. Nesta, L. Chang, S.F. Chase, T.M. Laue, and C.J. Roberts, *Nonnative aggregation of an IgG1 antibody in acidic conditions: part 1. Unfolding, colloidal interactions, and formation of high-molecular-weight aggregates.* J Pharm Sci, 2011. **100**(6): p. 2087-103.
99. Sakurai, K., R. Nakahata, Y.H. Lee, J. Kardos, T. Ikegami, and Y. Goto, *Effects of a reduced disulfide bond on aggregation properties of the human IgG1 CH3 domain.* Biochim Biophys Acta, 2015. **1854**(10 Pt A): p. 1526-35.
100. Brych, S.R., Y.R. Gokarn, H. Hultgen, R.J. Stevenson, R. Rajan, and M. Matsumura, *Characterization of antibody aggregation: role of buried, unpaired cysteines in particle formation.* J Pharm Sci, 2010. **99**(2): p. 764-81.
101. Harding, F.A., M.M. Stickler, J. Razo, and R.B. DuBridge, *The immunogenicity of humanized and fully human antibodies: residual immunogenicity resides in the CDR regions.* MAbs, 2010. **2**(3): p. 256-65.
102. Schellekens, H., *Bioequivalence and the immunogenicity of biopharmaceuticals.* Nat Rev Drug Discov, 2002. **1**(6): p. 457-62.
103. Moussa, E.M., J.P. Panchal, B.S. Moorthy, J.S. Blum, M.K. Joubert, L.O. Narhi, and E.M. Topp, *Immunogenicity of Therapeutic Protein Aggregates.* J Pharm Sci, 2016. **105**(2): p. 417-430.
104. Leach, M.W., J.B. Rottman, M.B. Hock, D. Finco, J.L. Rojko, and J.C. Beyer, *Immunogenicity/hypersensitivity of biologics.* Toxicol Pathol, 2014. **42**(1): p. 293-300.

105. Kheddo, P., M. Tracka, J. Armer, R.J. Dearman, S. Uddin, C.F. van der Walle, and A.P. Golovanov, *The effect of arginine glutamate on the stability of monoclonal antibodies in solution.* Int J Pharm, 2014. **473**(1-2): p. 126-33.
106. Shukla, D. and B.L. Trout, *Interaction of arginine with proteins and the mechanism by which it inhibits aggregation.* J Phys Chem B, 2010. **114**(42): p. 13426-38.
107. Svilenov, H.L., A. Kulakova, M. Zalar, A.P. Golovanov, P. Harris, and G. Winter, *Orthogonal Techniques to Study the Effect of pH, Sucrose, and Arginine Salts on Monoclonal Antibody Physical Stability and Aggregation During Long-Term Storage.* J Pharm Sci, 2020. **109**(1): p. 584-594.
108. Courtois, F., N.J. Agrawal, T.M. Lauer, and B.L. Trout, *Rational design of therapeutic mAbs against aggregation through protein engineering and incorporation of glycosylation motifs applied to bevacizumab.* MAbs, 2016. **8**(1): p. 99-112.
109. Vlasak, J. and R. Ionescu, *Fragmentation of monoclonal antibodies.* MAbs, 2011. **3**(3): p. 253-63.
110. Liu, H., G. Gaza-Bulseco, and E. Lundell, *Assessment of antibody fragmentation by reversed-phase liquid chromatography and mass spectrometry.* J Chromatogr B Analyt Technol Biomed Life Sci, 2008. **876**(1): p. 13-23.
111. Yan, B., Z. Yates, A. Balland, and G.R. Kleemann, *Human IgG1 hinge fragmentation as the result of H2O2-mediated radical cleavage.* J Biol Chem, 2009. **284**(51): p. 35390-402.
112. Yates, Z., K. Gunasekaran, H. Zhou, Z. Hu, Z. Liu, R.R. Ketchem, and B. Yan, *Histidine residue mediates radical-induced hinge cleavage of human IgG1.* J Biol Chem, 2010. **285**(24): p. 18662-71.
113. Smith, M.A., M. Easton, P. Everett, G. Lewis, M. Payne, V. Riveros-Moreno, and G. Allen, *Specific cleavage of immunoglobulin G by copper ions.* Int J Pept Protein Res, 1996. **48**(1): p. 48-55.
114. Trexler-Schmidt, M., S. Sargis, J. Chiu, S. Sze-Khoo, M. Mun, Y.H. Kao, and M.W. Laird, *Identification and prevention of antibody disulfide bond reduction during cell culture manufacturing.* Biotechnol Bioeng, 2010. **106**(3): p. 452-61.
115. Ruaudel, J., M. Bertschinger, S. Letestu, R. Giovannini, P. Wassmann, and P. Moretti, *Antibody disulfide bond reduction during process development: Insights using a scale-down model process.* BMC Proceedings, 2015. **9**(S9): p. P24-P24.
116. Chung, W.K., B. Russell, Y. Yang, M. Handlogten, S. Hudak, M. Cao, J. Wang, D. Robbins, S. Ahuja, and M. Zhu, *Effects of antibody disulfide bond reduction on purification process performance and final drug substance stability.* Biotechnology and Bioengineering, 2017. **114**(6): p. 1264-1274.
117. Arora, J., Y. Hu, R. Esfandiary, H.A. Sathish, S.M. Bishop, S.B. Joshi, C.R. Middaugh, D.B. Volkin, and D.D. Weis, *Charge-mediated Fab-Fc interactions in an IgG1 antibody induce reversible self-association, cluster formation, and elevated viscosity.* MAbs, 2016. **8**(8): p. 1561-1574.
118. Esfandiary, R., A. Parupudi, J. Casas-Finet, D. Gadre, and H. Sathish, *Mechanism of reversible self-association of a monoclonal antibody: role of electrostatic and hydrophobic interactions.* J Pharm Sci, 2015. **104**(2): p. 577-86.
119. Stradner, A., H. Sedgwick, F. Cardinaux, W.C. Poon, S.U. Egelhaaf, and P. Schurtenberger, *Equilibrium cluster formation in concentrated protein solutions and colloids.* Nature, 2004. **432**(7016): p. 492-5.

120. Liu, J., M.D. Nguyen, J.D. Andya, and S.J. Shire, *Reversible self-association increases the viscosity of a concentrated monoclonal antibody in aqueous solution.* J Pharm Sci, 2005. **94**(9): p. 1928-40.
121. Saluja, A. and D.S. Kalonia, *Nature and consequences of protein-protein interactions in high protein concentration solutions.* Int J Pharm, 2008. **358**(1-2): p. 1-15.
122. Yadav, S., T.M. Scherer, S.J. Shire, and D.S. Kalonia, *Use of dynamic light scattering to determine second virial coefficient in a semidilute concentration regime.* Anal Biochem, 2011. **411**(2): p. 292-6.
123. Yadav, S., A. Sreedhara, S. Kanai, J. Liu, S. Lien, H. Lowman, D.S. Kalonia, and S.J. Shire, *Establishing a link between amino acid sequences and self-associating and viscoelastic behavior of two closely related monoclonal antibodies.* Pharm Res, 2011. **28**(7): p. 1750-64.
124. Kanai, S., J. Liu, T.W. Patapoff, and S.J. Shire, *Reversible self-association of a concentrated monoclonal antibody solution mediated by Fab-Fab interaction that impacts solution viscosity.* J Pharm Sci, 2008. **97**(10): p. 4219-27.
125. Saito, S., J. Hasegawa, N. Kobayashi, N. Kishi, S. Uchiyama, and K. Fukui, *Behavior of monoclonal antibodies: relation between the second virial coefficient (B (2)) at low concentrations and aggregation propensity and viscosity at high concentrations.* Pharm Res, 2012. **29**(2): p. 397-410.
126. Salinas, B.A., H.A. Sathish, S.M. Bishop, N. Harn, J.F. Carpenter, and T.W. Randolph, *Understanding and modulating opalescence and viscosity in a monoclonal antibody formulation.* J Pharm Sci, 2010. **99**(1): p. 82-93.
127. Rathore, N., P. Pranay, J. Bernacki, B. Eu, W. Ji, and E. Walls, *Characterization of protein rheology and delivery forces for combination products.* J Pharm Sci, 2012. **101**(12): p. 4472-80.
128. Zhang, Z. and Y. Liu, *Recent progresses of understanding the viscosity of concentrated protein solutions.* Current Opinion in Chemical Engineering, 2017. **16**: p. 48-55.
129. Allmendinger, A., R. Mueller, J. Huwyler, H.C. Mahler, and S. Fischer, *Sterile Filtration of Highly Concentrated Protein Formulations: Impact of Protein Concentration, Formulation Composition, and Filter Material.* J Pharm Sci, 2015. **104**(10): p. 3319-29.
130. Cilurzo, F., F. Selmin, P. Minghetti, M. Adami, E. Bertoni, S. Lauria, and L. Montanari, *Injectability evaluation: an open issue.* AAPS PharmSciTech, 2011. **12**(2): p. 604-9.
131. Flory, P.J., *Thermodynamics of High Polymer Solutions.* The Journal of Chemical Physics, 1942. **10**(1): p. 51-61.
132. Dobry, A. and F. Boyer-Kawenoki, *Phase separation in polymer solution.* Journal of Polymer Science, 1947. **2**(1): p. 90-100.
133. Capdevila, C., M.K. Miller, and K.F. Russell, *Aluminum partitioning during phase separation in Fe–20%Cr–6%Al ODS alloy.* Journal of Materials Science, 2008. **43**(11): p. 3889-3893.
134. Sagui, C. and M. Grant, *Theory of nucleation and growth during phase separation.* Physical Review E, 1999. **59**(4): p. 4175-4187.
135. Kyu, T. and P. Mukherjee, *Kinetics of phase separation by spinodal decomposition in a liquid-crystalline polymer solution.* Liquid Crystals, 1988. **3**(5): p. 631-644.

136. Raut, A.S. and D.S. Kalonia, *Pharmaceutical Perspective on Opalescence and Liquid-Liquid Phase Separation in Protein Solutions.* Mol Pharm, 2016. **13**(5): p. 1431-44.
137. Debye, P., B. Chu, and H. Kaufmann, *Critical Opalescence of Binary Liquid Mixtures: Methanol—Cyclohexane; Aniline—Cyclohexane.* The Journal of Chemical Physics, 1962. **36**(12): p. 3378-3381.
138. Kiese, S., A. Papppenberger, W. Friess, and H.C. Mahler, *Shaken, not stirred: mechanical stress testing of an IgG1 antibody.* J Pharm Sci, 2008. **97**(10): p. 4347-66.
139. Mahler, H.C., R. Muller, W. Friess, A. Delille, and S. Matheus, *Induction and analysis of aggregates in a liquid IgG1-antibody formulation.* Eur J Pharm Biopharm, 2005. **59**(3): p. 407-17.
140. Nishi, H., M. Miyajima, H. Nakagami, M. Noda, S. Uchiyama, and K. Fukui, *Phase separation of an IgG1 antibody solution under a low ionic strength condition.* Pharm Res, 2010. **27**(7): p. 1348-60.
141. Mason, B.D., L. Zhang, R.L. Remmele, Jr., and J. Zhang, *Opalescence of an IgG2 monoclonal antibody solution as it relates to liquid-liquid phase separation.* J Pharm Sci, 2011. **100**(11): p. 4587-96.
142. Mason, B.D., J. Zhang-van Enk, L. Zhang, R.L. Remmele, Jr., and J. Zhang, *Liquid-liquid phase separation of a monoclonal antibody and nonmonotonic influence of Hofmeister anions.* Biophys J, 2010. **99**(11): p. 3792-800.
143. Reiche, K., J. Hartl, A. Blume, and P. Garidel, *Liquid-liquid phase separation of a monoclonal antibody at low ionic strength: Influence of anion charge and concentration.* Biophys Chem, 2017. **220**: p. 7-19.
144. Wang, Y., R.F. Latypov, A. Lomakin, J.A. Meyer, B.A. Kerwin, S. Vunnum, and G.B. Benedek, *Quantitative evaluation of colloidal stability of antibody solutions using PEG-induced liquid-liquid phase separation.* Mol Pharm, 2014. **11**(5): p. 1391-402.
145. Raut, A.S. and D.S. Kalonia, *Liquid-Liquid Phase Separation in a Dual Variable Domain Immunoglobulin Protein Solution: Effect of Formulation Factors and Protein-Protein Interactions.* Mol Pharm, 2015. **12**(9): p. 3261-71.
146. Ahamed, T., B.N. Esteban, M. Ottens, G.W. van Dedem, L.A. van der Wielen, M.A. Bisschops, A. Lee, C. Pham, and J. Thommes, *Phase behavior of an intact monoclonal antibody.* Biophys J, 2007. **93**(2): p. 610-9.
147. Kheddo, P., J.E. Bramham, R.J. Dearman, S. Uddin, C.F. van der Walle, and A.P. Golovanov, *Investigating Liquid-Liquid Phase Separation of a Monoclonal Antibody Using Solution-State NMR Spectroscopy: Effect of Arg.Glu and Arg.HCl.* Mol Pharm, 2017. **14**(8): p. 2852-2860.
148. Thompson, R.W., Jr., R.F. Latypov, Y. Wang, A. Lomakin, J.A. Meyer, S. Vunnum, and G.B. Benedek, *Evaluation of effects of pH and ionic strength on colloidal stability of IgG solutions by PEG-induced liquid-liquid phase separation.* J Chem Phys, 2016. **145**(18): p. 185101.
149. Vis, M., V.F. Peters, R.H. Tromp, and B.H. Erne, *Donnan potentials in aqueous phase-separated polymer mixtures.* Langmuir, 2014. **30**(20): p. 5755-62.
150. Goldberg, D.S., R.A. Lewus, R. Esfandiary, D.C. Farkas, N. Mody, K.J. Day, P. Mallik, M.B. Tracka, S.K. Sealey, and H.S. Samra, *Utility of High Throughput Screening Techniques to Predict Stability of Monoclonal Antibody Formulations During Early Stage Development.* J Pharm Sci, 2017. **106**(8): p. 1971-1977.

151. Raut, A.S. and D.S. Kalonia, *Effect of Excipients on Liquid-Liquid Phase Separation and Aggregation in Dual Variable Domain Immunoglobulin Protein Solutions.* Mol Pharm, 2016. **13**(3): p. 774-83.

152. Golovanov, A.P., G.M. Hautbergue, S.A. Wilson, and L.Y. Lian, *A simple method for improving protein solubility and long-term stability.* J Am Chem Soc, 2004. **126**(29): p. 8933-9.

153. Kheddo, P., J.E. Bramham, R.J. Dearman, S. Uddin, C.F. van der Walle, and A.P. Golovanov, *The effect of arginine salt form on a liquid-liquid phase separating monoclonal antibody solution revealed by ^{1}H NMR spectroscopy*. 2017: Manuscript in preparation.

154. Borwankar, A.U., B.J. Dear, A. Twu, J.J. Hung, A.K. Dinin, B.K. Wilson, J. Yue, J.A. Maynard, T.M. Truskett, and K.P. Johnston, *Viscosity Reduction of a Concentrated Monoclonal Antibody with Arginine·HCl and Arginine·Glutamate.* Industrial & Engineering Chemistry Research, 2016. **55**(43): p. 11225-11234.

155. Oki, S., S. Nishinami, and K. Shiraki, *Arginine suppresses opalescence and liquid-liquid phase separation in IgG solutions.* Int J Biol Macromol, 2018. **118**(Pt B): p. 1708-1712.

156. Wang, Y., A. Lomakin, R.F. Latypov, and G.B. Benedek, *Phase separation in solutions of monoclonal antibodies and the effect of human serum albumin.* Proc Natl Acad Sci U S A, 2011. **108**(40): p. 16606-11.

157. Du, Q., M. Damschroder, T.M. Pabst, A.K. Hunter, W.K. Wang, and H. Luo, *Process optimization and protein engineering mitigated manufacturing challenges of a monoclonal antibody with liquid-liquid phase separation issue by disrupting inter-molecule electrostatic interactions.* MAbs, 2019. **11**(4): p. 789-802.

158. Chow, C.K., B.W. Allan, Q. Chai, S. Atwell, and J. Lu, *Therapeutic Antibody Engineering To Improve Viscosity and Phase Separation Guided by Crystal Structure.* Mol Pharm, 2016. **13**(3): p. 915-23.

159. Matsuoka, T., R. Miyauchi, N. Nagaoka, and J. Hasegawa, *Mitigation of liquid-liquid phase separation of a monoclonal antibody by mutations of negative charges on the Fab surface.* PLoS One, 2020. **15**(10): p. e0240673.

160. Braun, M.K., A. Sauter, O. Matsarskaia, M. Wolf, F. Roosen-Runge, M. Sztucki, R. Roth, F. Zhang, and F. Schreiber, *Reentrant Phase Behavior in Protein Solutions Induced by Multivalent Salts: Strong Effect of Anions Cl(-) Versus NO3(.).* J Phys Chem B, 2018. **122**(50): p. 11978-11985.

161. Braun, M.K., M. Wolf, O. Matsarskaia, S. Da Vela, F. Roosen-Runge, M. Sztucki, R. Roth, F. Zhang, and F. Schreiber, *Strong Isotope Effects on Effective Interactions and Phase Behavior in Protein Solutions in the Presence of Multivalent Ions.* J Phys Chem B, 2017. **121**(7): p. 1731-1739.

162. Matsarskaia, O., M.K. Braun, F. Roosen-Runge, M. Wolf, F. Zhang, R. Roth, and F. Schreiber, *Cation-Induced Hydration Effects Cause Lower Critical Solution Temperature Behavior in Protein Solutions.* J Phys Chem B, 2016. **120**(31): p. 7731-6.

163. Liu, C., N. Asherie, A. Lomakin, J. Pande, O. Ogun, and G.B. Benedek, *Phase separation in aqueous solutions of lens gamma-crystallins: special role of gamma s.* Proc Natl Acad Sci U S A, 1996. **93**(1): p. 377-82.

164. Siezen, R.J., M.R. Fisch, C. Slingsby, and G.B. Benedek, *Opacification of gamma-crystallin solutions from calf lens in relation to cold cataract formation.* Proc Natl Acad Sci U S A, 1985. **82**(6): p. 1701-5.

165. Thomson, J.A., P. Schurtenberger, G.M. Thurston, and G.B. Benedek, *Binary liquid phase separation and critical phenomena in a protein/water solution.* Proc Natl Acad Sci U S A, 1987. **84**(20): p. 7079-83.

166. Monkos, K., *Concentration and temperature dependence of viscosity in lysozyme aqueous solutions.* Biochim Biophys Acta, 1997. **1339**(2): p. 304-10.

167. Taratuta, V.G., A. Holschbach, G.M. Thurston, D. Blankschtein, and G.B. Benedek, *Liquid-liquid phase separation of aqueous lysozyme solutions: effects of pH and salt identity.* The Journal of Physical Chemistry, 1990. **94**(5): p. 2140-2144.

168. Berry, J., C.P. Brangwynne, and M. Haataja, *Physical principles of intracellular organization via active and passive phase transitions.* Rep Prog Phys, 2018. **81**(4): p. 046601.

169. Comert, F. and P.L. Dubin, *Liquid-liquid and liquid-solid phase separation in protein-polyelectrolyte systems.* Adv Colloid Interface Sci, 2017. **239**: p. 213-217.

170. Da Vela, S., M.K. Braun, A. Dorr, A. Greco, J. Moller, Z. Fu, F. Zhang, and F. Schreiber, *Kinetics of liquid-liquid phase separation in protein solutions exhibiting LCST phase behavior studied by time-resolved USAXS and VSANS.* Soft Matter, 2016. **12**(46): p. 9334-9341.

171. Dumetz, A.C., R.A. Lewus, A.M. Lenhoff, and E.W. Kaler, *Effects of ammonium sulfate and sodium chloride concentration on PEG/protein liquid-liquid phase separation.* Langmuir, 2008. **24**(18): p. 10345-51.

172. Tanaka, S., M. Yamamoto, K. Ito, R. Hayakawa, and M. Ataka, *Relation between the phase separation and the crystallization in protein solutions.* Physical Review E, 1997. **56**(1): p. R67-R69.

173. ten Wolde, P.R. and D. Frenkel, *Enhancement of protein crystal nucleation by critical density fluctuations.* Science, 1997. **277**(5334): p. 1975-8.

174. Matsarskaia, O., F. Roosen-Runge, G. Lotze, J. Moller, A. Mariani, F. Zhang, and F. Schreiber, *Tuning phase transitions of aqueous protein solutions by multivalent cations.* Phys Chem Chem Phys, 2018. **20**(42): p. 27214-27225.

175. Roosen-Runge, F., B.S. Heck, F. Zhang, O. Kohlbacher, and F. Schreiber, *Interplay of pH and binding of multivalent metal ions: charge inversion and reentrant condensation in protein solutions.* J Phys Chem B, 2013. **117**(18): p. 5777-87.

176. Kurinomaru, T., T. Maruyama, S. Izaki, K. Handa, T. Kimoto, and K. Shiraki, *Protein-poly(amino acid) complex precipitation for high-concentration protein formulation.* J Pharm Sci, 2014. **103**(8): p. 2248-54.

177. Kurinomaru, T. and K. Shiraki, *Aggregative protein-polyelectrolyte complex for high-concentration formulation of protein drugs.* Int J Biol Macromol, 2017. **100**: p. 11-17.

178. Matsuda, A., M. Mimura, T. Maruyama, T. Kurinomaru, M. Shiuhei, and K. Shiraki, *Liquid Droplet of Protein-Polyelectrolyte Complex for High-Concentration Formulations.* J Pharm Sci, 2018. **107**(10): p. 2713-2719.

179. Zang, Y., B. Kammerer, M. Eisenkolb, K. Lohr, and H. Kiefer, *Towards protein crystallization as a process step in downstream processing of therapeutic antibodies: screening and optimization at microbatch scale.* PLoS One, 2011. **6**(9): p. e25282.

180. Lieu, R., S. Antonysamy, Z. Druzina, C. Ho, N.R. Kang, A. Pustilnik, J. Wang, and S. Atwell, *Rapid and robust antibody Fab fragment crystallization utilizing edge-to-edge beta-sheet packing.* PLoS One, 2020. **15**(9): p. e0232311.

181. Boeynaems, S., S. Alberti, N.L. Fawzi, T. Mittag, M. Polymenidou, F. Rousseau, J. Schymkowitz, J. Shorter, B. Wolozin, L. Van Den Bosch, P. Tompa, and M. Fuxreiter, *Protein Phase Separation: A New Phase in Cell Biology.* Trends Cell Biol, 2018. **28**(6): p. 420-435.
182. Hyman, A.A., C.A. Weber, and F. Julicher, *Liquid-liquid phase separation in biology.* Annu Rev Cell Dev Biol, 2014. **30**: p. 39-58.
183. Yoshizawa, T., R.S. Nozawa, T.Z. Jia, T. Saio, and E. Mori, *Biological phase separation: cell biology meets biophysics.* Biophys Rev, 2020. **12**(2): p. 519-539.
184. Brangwynne, C.P., T.J. Mitchison, and A.A. Hyman, *Active liquid-like behavior of nucleoli determines their size and shape in Xenopus laevis oocytes.* Proc Natl Acad Sci U S A, 2011. **108**(11): p. 4334-9.
185. Strzelecka, M., S. Trowitzsch, G. Weber, R. Luhrmann, A.C. Oates, and K.M. Neugebauer, *Coilin-dependent snRNP assembly is essential for zebrafish embryogenesis.* Nat Struct Mol Biol, 2010. **17**(4): p. 403-9.
186. Brangwynne, C.P., C.R. Eckmann, D.S. Courson, A. Rybarska, C. Hoege, J. Gharakhani, F. Julicher, and A.A. Hyman, *Germline P granules are liquid droplets that localize by controlled dissolution/condensation.* Science, 2009. **324**(5935): p. 1729-32.
187. Garcia Quiroz, F., N.K. Li, S. Roberts, P. Weber, M. Dzuricky, I. Weitzhandler, Y.G. Yingling, and A. Chilkoti, *Intrinsically disordered proteins access a range of hysteretic phase separation behaviors.* Sci Adv, 2019. **5**(10): p. eaax5177.
188. Ramaswami, M., J.P. Taylor, and R. Parker, *Altered ribostasis: RNA-protein granules in degenerative disorders.* Cell, 2013. **154**(4): p. 727-36.
189. Elbaum-Garfinkle, S., *Matter over mind: Liquid phase separation and neurodegeneration.* J Biol Chem, 2019. **294**(18): p. 7160-7168.
190. Patel, A., H.O. Lee, L. Jawerth, S. Maharana, M. Jahnel, M.Y. Hein, S. Stoynov, J. Mahamid, S. Saha, T.M. Franzmann, A. Pozniakovski, I. Poser, N. Maghelli, L.A. Royer, M. Weigert, E.W. Myers, S. Grill, D. Drechsel, A.A. Hyman, and S. Alberti, *A Liquid-to-Solid Phase Transition of the ALS Protein FUS Accelerated by Disease Mutation.* Cell, 2015. **162**(5): p. 1066-77.
191. Molliex, A., J. Temirov, J. Lee, M. Coughlin, A.P. Kanagaraj, H.J. Kim, T. Mittag, and J.P. Taylor, *Phase separation by low complexity domains promotes stress granule assembly and drives pathological fibrillization.* Cell, 2015. **163**(1): p. 123-33.
192. Pande, A., N. Mokhor, and J. Pande, *Deamidation of Human gammaS-Crystallin Increases Attractive Protein Interactions: Implications for Cataract.* Biochemistry, 2015. **54**(31): p. 4890-9.
193. Charles, E.D. and L.B. Dustin, *Hepatitis C virus-induced cryoglobulinemia.* Kidney Int, 2009. **76**(8): p. 818-24.
194. Chaturvedi, S.K., J. Ma, P.H. Brown, H. Zhao, and P. Schuck, *Measuring macromolecular size distributions and interactions at high concentrations by sedimentation velocity.* Nat Commun, 2018. **9**(1): p. 4415.
195. Roberts, D., R. Keeling, M. Tracka, C.F. van der Walle, S. Uddin, J. Warwicker, and R. Curtis, *Specific ion and buffer effects on protein-protein interactions of a monoclonal antibody.* Mol Pharm, 2015. **12**(1): p. 179-93.
196. Roberts, D., R. Keeling, M. Tracka, C.F. van der Walle, S. Uddin, J. Warwicker, and R. Curtis, *The role of electrostatics in protein-protein interactions of a monoclonal antibody.* Mol Pharm, 2014. **11**(7): p. 2475-89.
197. Yearley, E.J., P.D. Godfrin, T. Perevozchikova, H. Zhang, P. Falus, L. Porcar, M. Nagao, J.E. Curtis, P. Gawande, R. Taing, I.E. Zarraga, N.J. Wagner, and Y. Liu,

Observation of small cluster formation in concentrated monoclonal antibody solutions and its implications to solution viscosity. Biophys J, 2014. **106**(8): p. 1763-70.

198. Duus, J., C.H. Gotfredsen, and K. Bock, *Carbohydrate structural determination by NMR spectroscopy: modern methods and limitations.* Chem Rev, 2000. **100**(12): p. 4589-614.
199. Kleckner, I.R. and M.P. Foster, *An introduction to NMR-based approaches for measuring protein dynamics.* Biochim Biophys Acta, 2011. **1814**(8): p. 942-68.
200. Hirasaki, G.J., S.W. Lo, and Y. Zhang, *NMR properties of petroleum reservoir fluids.* Magn Reson Imaging, 2003. **21**(3-4): p. 269-77.
201. Grover, V.P., J.M. Tognarelli, M.M. Crossey, I.J. Cox, S.D. Taylor-Robinson, and M.J. McPhail, *Magnetic Resonance Imaging: Principles and Techniques: Lessons for Clinicians.* J Clin Exp Hepatol, 2015. **5**(3): p. 246-55.
202. Crespi, H.L. and J.J. Katz, *High resolution proton magnetic resonance studies of fully deuterated and isotope hybrid proteins.* Nature, 1969. **224**(5219): p. 560-2.
203. Cavalli, A., X. Salvatella, C.M. Dobson, and M. Vendruscolo, *Protein structure determination from NMR chemical shifts.* Proc Natl Acad Sci U S A, 2007. **104**(23): p. 9615-20.
204. Palmer, A.G., 3rd, *Enzyme dynamics from NMR spectroscopy.* Acc Chem Res, 2015. **48**(2): p. 457-65.
205. Zalar, M., S. Indrakumar, C.W. Levy, R.B. Tunnicliffe, G.H.J. Peters, and A.P. Golovanov, *Studies of the oligomerisation mechanism of a cystatin-based engineered protein scaffold.* Sci Rep, 2019. **9**(1): p. 9067.
206. Ishima, R. and D.A. Torchia, *Protein dynamics from NMR.* Nat Struct Biol, 2000. **7**(9): p. 740-3.
207. Dutta, A., K. Saxena, H. Schwalbe, and J. Klein-Seetharaman, *Isotope labeling in mammalian cells.* Methods Mol Biol, 2012. **831**: p. 55-69.
208. Reddy, P.T., R.G. Brinson, J.T. Hoopes, C. McClung, N. Ke, L. Kashi, M. Berkmen, and Z. Kelman, *Platform development for expression and purification of stable isotope labeled monoclonal antibodies in Escherichia coli.* MAbs, 2018. **10**(7): p. 992-1002.
209. Frueh, D.P., A.C. Goodrich, S.H. Mishra, and S.R. Nichols, *NMR methods for structural studies of large monomeric and multimeric proteins.* Curr Opin Struct Biol, 2013. **23**(5): p. 734-9.
210. Xu, Y. and S. Matthews, *TROSY NMR Spectroscopy of Large Soluble Proteins*, in *Modern NMR Methodology*, H. Heise and S. Matthews, Editors. 2013, Springer Berlin Heidelberg. p. 97-119.
211. Brovč, E.V., S. Pajk, R. Šink, and J. Mravljak, *Comparison of the NMR and the Acid Value Determination Methods for Quality Control of Input Polysorbates.* Acta Chimica Slovenica, 2019. **66**(4): p. 934-943.
212. Magarian, N., K. Lee, K. Nagpal, K. Skidmore, and E. Mahajan, *Clearance of extractables and leachables from single-use technologies via ultrafiltration/diafiltration operations.* Biotechnol Prog, 2016. **32**(3): p. 718-24.
213. Lei, M., J. Sugahara, D. Hewitt, D. Beane, R. Jayakar, C. Cornell, K. Skidmore, Y.H. Kao, and J. Ji, *The effects of membrane filters used in biopharmaceutical processes on the concentration and composition of polysorbate 20.* Biotechnol Prog, 2013. **29**(6): p. 1503-11.
214. Skidmore, K., D. Hewitt, and Y.H. Kao, *Quantitation and characterization of process impurities and extractables in protein-containing solutions using proton NMR as a general tool.* Biotechnol Prog, 2012. **28**(6): p. 1526-33.

215. Martinez Morales, M., M. Zalar, S. Sonzini, A.P. Golovanov, C.F. van der Walle, and J.P. Derrick, *Interaction of a Macrocycle with an Aggregation-Prone Region of a Monoclonal Antibody.* Mol Pharm, 2019. **16**(7): p. 3100-3108.
216. Zalar, M., H.L. Svilenov, and A.P. Golovanov, *Binding of excipients is a poor predictor for aggregation kinetics of biopharmaceutical proteins.* Eur J Pharm Biopharm, 2020. **151**: p. 127-136.
217. Mensink, M.A., M.J. Nethercott, W.L.J. Hinrichs, K. van der Voort Maarschalk, H.W. Frijlink, E.J. Munson, and M.J. Pikal, *Influence of Miscibility of Protein-Sugar Lyophilizates on Their Storage Stability.* AAPS J, 2016. **18**(5): p. 1225-1232.
218. Poppe, L., J.B. Jordan, K. Lawson, M. Jerums, I. Apostol, and P.D. Schnier, *Profiling formulated monoclonal antibodies by (1)H NMR spectroscopy.* Anal Chem, 2013. **85**(20): p. 9623-9.
219. Poppe, L., J.B. Jordan, G. Rogers, and P.D. Schnier, *On the Analytical Superiority of 1D NMR for Fingerprinting the Higher Order Structure of Protein Therapeutics Compared to Multidimensional NMR Methods.* Anal Chem, 2015. **87**(11): p. 5539-45.
220. Franks, J., J.N. Glushka, M.T. Jones, D.H. Live, Q. Zou, and J.H. Prestegard, *Spin Diffusion Editing for Structural Fingerprints of Therapeutic Antibodies.* Anal Chem, 2016. **88**(2): p. 1320-7.
221. Arbogast, L.W., R.G. Brinson, T. Formolo, J.T. Hoopes, and J.P. Marino, *2D (1)H(N), (15)N Correlated NMR Methods at Natural Abundance for Obtaining Structural Maps and Statistical Comparability of Monoclonal Antibodies.* Pharm Res, 2016. **33**(2): p. 462-75.
222. Arbogast, L.W., R.G. Brinson, and J.P. Marino, *Mapping monoclonal antibody structure by 2D 13C NMR at natural abundance.* Anal Chem, 2015. **87**(7): p. 3556-61.
223. Singh, S.M., S. Bandi, D.N.M. Jones, and K.M.G. Mallela, *Effect of Polysorbate 20 and Polysorbate 80 on the Higher-Order Structure of a Monoclonal Antibody and Its Fab and Fc Fragments Probed Using 2D Nuclear Magnetic Resonance Spectroscopy.* J Pharm Sci, 2017. **106**(12): p. 3486-3498.
224. Castiglia, F., F. Zevolini, G. Riolo, J. Brunetti, A. De Lazzari, A. Moretto, G. Manetto, M. Fragai, J. Algotsson, J. Evenas, L. Bracci, A. Pini, and C. Falciani, *NMR Study of the Secondary Structure and Biopharmaceutical Formulation of an Active Branched Antimicrobial Peptide.* Molecules, 2019. **24**(23): p. 13.
225. Cha, S., W.S. Lee, J. Choi, J.G. Jeong, J.R. Nam, J. Kim, H.N. Kim, J.H. Lee, J.S. Yoo, and K.S. Ryu, *NMR mapping of the highly flexible regions of (13)C/(15)N-labeled antibody TTAC-0001-Fab.* J Biomol NMR, 2020. **74**(6-7): p. 311-319.
226. Hinterholzer, A., V. Stanojlovic, C. Cabrele, and M. Schubert, *Unambiguous Identification of Pyroglutamate in Full-Length Biopharmaceutical Monoclonal Antibodies by NMR Spectroscopy.* Anal Chem, 2019. **91**(22): p. 14299-14305.
227. Hinterholzer, A., V. Stanojlovic, C. Regl, C.G. Huber, C. Cabrele, and M. Schubert, *Identification and Quantification of Oxidation Products in Full-Length Biotherapeutic Antibodies by NMR Spectroscopy.* Anal Chem, 2020. **92**(14): p. 9666-9673.
228. Majumder, S., A. Saati, S. Philip, L.L. Liu, E. Stephens, J.C. Rouse, and A. Alphonse Ignatius, *Utility of High Resolution NMR Methods to Probe the Impact of Chemical Modifications on Higher Order Structure of Monoclonal Antibodies in Relation to Antigen Binding.* Pharm Res, 2019. **36**(9): p. 130.

229. Tokunaga, Y., K. Takeuchi, J. Okude, K. Ori, T. Torizawa, and I. Shimada, *Structural Fingerprints of an Intact Monoclonal Antibody Acquired under Formulated Storage Conditions via (15)N Direct Detection Nuclear Magnetic Resonance.* J Med Chem, 2020. **63**(10): p. 5360-5366.
230. Patil, S.M., D.A. Keire, and K. Chen, *Comparison of NMR and Dynamic Light Scattering for Measuring Diffusion Coefficients of Formulated Insulin: Implications for Particle Size Distribution Measurements in Drug Products.* AAPS J, 2017. **19**(6): p. 1760-1766.
231. Falk, B.T., Y. Liang, and M.A. McCoy, *Profiling Insulin Oligomeric States by (1)H NMR Spectroscopy for Formulation Development of Ultra-Rapid-Acting Insulin.* J Pharm Sci, 2020. **109**(1): p. 922-926.
232. Falk, B.T., Y. Liang, and M.A. McCoy, *Diffusion Profiling of Therapeutic Proteins by Using Solution NMR Spectroscopy.* Chembiochem, 2019. **20**(7): p. 896-899.
233. Kheddo, P., M.J. Cliff, S. Uddin, C.F. van der Walle, and A.P. Golovanov, *Characterizing monoclonal antibody formulations in arginine glutamate solutions using (1)H NMR spectroscopy.* MAbs, 2016. **8**(7): p. 1245-1258.
234. Edwards, J.M., J.P. Derrick, C.F. van der Walle, and A.P. Golovanov, *(19)F NMR as a Tool for Monitoring Individual Differentially Labeled Proteins in Complex Mixtures.* Mol Pharm, 2018. **15**(7): p. 2785-2796.
235. Edwards, J.M., P. Harris, J.T. Bukrinski, and A.P. Golovanov, *Use of (19) F Differential Labelling for the Simultaneous Detection and Monitoring of Three Individual Proteins in a Serum Environment.* Chempluschem, 2019. **84**(5): p. 443-446.
236. Taraban, M.B., K.T. Briggs, P. Merkel, and Y.B. Yu, *Flow Water Proton NMR: In-Line Process Analytical Technology for Continuous Biomanufacturing.* Anal Chem, 2019. **91**(21): p. 13538-13546.
237. Abraham, A., O. Elkassabany, M.E. Krause, and A. Ott, *A nondestructive and noninvasive method to determine water content in lyophilized proteins using low-field time-domain NMR.* Magn Reson Chem, 2019. **57**(10): p. 873-877.
238. Murthy, A.C., G.L. Dignon, Y. Kan, G.H. Zerze, S.H. Parekh, J. Mittal, and N.L. Fawzi, *Molecular interactions underlying liquid-liquid phase separation of the FUS low-complexity domain.* Nat Struct Mol Biol, 2019. **26**(7): p. 637-648.
239. Conicella, A.E., G.L. Dignon, G.H. Zerze, H.B. Schmidt, A.M. D'Ordine, Y.C. Kim, R. Rohatgi, Y.M. Ayala, J. Mittal, and N.L. Fawzi, *TDP-43 alpha-helical structure tunes liquid-liquid phase separation and function.* Proc Natl Acad Sci U S A, 2020. **117**(11): p. 5883-5894.
240. Chiu, Y.P., Y.C. Sun, D.C. Qiu, Y.H. Lin, Y.Q. Chen, J.C. Kuo, and J.R. Huang, *Liquid-liquid phase separation and extracellular multivalent interactions in the tale of galectin-3.* Nat Commun, 2020. **11**(1): p. 1229.
241. Ryan, V.H., S. Watters, J. Amaya, B. Khatiwada, V. Venditti, M.T. Naik, and N.L. Fawzi, *Weak binding to the A2RE RNA rigidifies hnRNPA2 RRMs and reduces liquid-liquid phase separation and aggregation.* Nucleic Acids Res, 2020. **48**(18): p. 10542-10554.
242. Wong, L.E., T.H. Kim, D.R. Muhandiram, J.D. Forman-Kay, and L.E. Kay, *NMR Experiments for Studies of Dilute and Condensed Protein Phases: Application to the Phase-Separating Protein CAPRIN1.* J Am Chem Soc, 2020. **142**(5): p. 2471-2489.
243. Brady, J.P., P.J. Farber, A. Sekhar, Y.H. Lin, R. Huang, A. Bah, T.J. Nott, H.S. Chan, A.J. Baldwin, J.D. Forman-Kay, and L.E. Kay, *Structural and*

hydrodynamic properties of an intrinsically disordered region of a germ cell-specific protein on phase separation. Proc Natl Acad Sci U S A, 2017. **114**(39): p. E8194-E8203.

244. Burke, K.A., A.M. Janke, C.L. Rhine, and N.L. Fawzi, *Residue-by-Residue View of In Vitro FUS Granules that Bind the C-Terminal Domain of RNA Polymerase II.* Mol Cell, 2015. **60**(2): p. 231-41.
245. Ackermann, B.E. and G.T. Debelouchina, *Heterochromatin Protein HP1alpha Gelation Dynamics Revealed by Solid-State NMR Spectroscopy.* Angew Chem Int Ed Engl, 2019. **58**(19): p. 6300-6305.
246. Gibbs, E., B. Perrone, A. Hassan, R. Kummerle, and R. Kriwacki, *NPM1 exhibits structural and dynamic heterogeneity upon phase separation with the p14ARF tumor suppressor.* J Magn Reson, 2020. **310**: p. 106646.
247. Reichheld, S.E., L.D. Muiznieks, F.W. Keeley, and S. Sharpe, *Direct observation of structure and dynamics during phase separation of an elastomeric protein.* Proc Natl Acad Sci U S A, 2017. **114**(22): p. E4408-E4415.
248. Murthy, A.C. and N.L. Fawzi, *The (un)structural biology of biomolecular liquid-liquid phase separation using NMR spectroscopy.* J Biol Chem, 2020. **295**(8): p. 2375-2384.
249. Martin, B.T., G.C. Chingas, and O.M. McDougal, *Origin and correction of magnetic field inhomogeneity at the interface in biphasic NMR samples.* J Magn Reson, 2012. **218**: p. 147-52.
250. Savastano, A., D. Flores, H. Kadavath, J. Biernat, E. Mandelkow, and M. Zweckstetter, *Disease-Associated Tau Phosphorylation Hinders Tubulin Assembly within Tau Condensates.* Angew Chem Int Ed Engl, 2021. **60**(2): p. 726-730.
251. Fawzi, N.L., J. Ying, D.A. Torchia, and G.M. Clore, *Kinetics of amyloid beta monomer-to-oligomer exchange by NMR relaxation.* J Am Chem Soc, 2010. **132**(29): p. 9948-51.
252. Fawzi, N.L., J. Ying, D.A. Torchia, and G.M. Clore, *Probing exchange kinetics and atomic resolution dynamics in high-molecular-weight complexes using dark-state exchange saturation transfer NMR spectroscopy.* Nat Protoc, 2012. **7**(8): p. 1523-33.
253. Helgstrand, M., T. Hard, and P. Allard, *Simulations of NMR pulse sequences during equilibrium and non-equilibrium chemical exchange.* J Biomol NMR, 2000. **18**(1): p. 49-63.
254. Egner, T.K., P. Naik, N.C. Nelson, Slowing, II, and V. Venditti, *Mechanistic Insight into Nanoparticle Surface Adsorption by Solution NMR Spectroscopy in an Aqueous Gel.* Angew Chem Int Ed Engl, 2017. **56**(33): p. 9802-9806.
255. Xue, M., J. Sampath, R.N. Gebhart, H.J. Haugen, S.P. Lyngstadaas, J. Pfaendtner, and G. Drobny, *Studies of Dynamic Binding of Amino Acids to TiO2 Nanoparticle Surfaces by Solution NMR and Molecular Dynamics Simulations.* Langmuir, 2020. **36**(35): p. 10341-10350.
256. Johnson, C.S., *Diffusion ordered nuclear magnetic resonance spectroscopy: principles and applications.* Progress in Nuclear Magnetic Resonance Spectroscopy, 1999. **34**(3-4): p. 203-256.
257. Petersen, B.O., M. Nilsson, M. Bojstrup, O. Hindsgaul, and S. Meier, *(1)H NMR spectroscopy for profiling complex carbohydrate mixtures in non-fractionated beer.* Food Chem, 2014. **150**: p. 65-72.
258. Dumez, J.N., *Spatial encoding and spatial selection methods in high-resolution NMR spectroscopy.* Prog Nucl Magn Reson Spectrosc, 2018. **109**: p. 101-134.

259. Kozminski, W., *Application of spatially resolved NMR spectroscopy for high resolution spectra of heterogeneous samples.* Polish Journal of Chemistry, 2000. **74**(8): p. 1185-1189.
260. Emsley, L. and G. Bodenhausen, *Optimization of shaped selective pulses for NMR using a quaternion description of their overall propagators.* Journal of Magnetic Resonance (1969), 1992. **97**(1): p. 135-148.
261. Evans, R., A. Sandhu, T. Bridgwater, and K. Chong, *Slice-Selective NMR: A Noninvasive Method for the Analysis of Separated Pyrolysis Fuel Samples.* Energy & Fuels, 2017. **31**(4): p. 4135-4142.
262. Wisniewska, M.A. and J.G. Seland, *Investigating structure-dependent diffusion in hydrogels using spatially resolved NMR spectroscopy.* J Colloid Interface Sci, 2019. **533**: p. 671-677.
263. Wagner, G.E., P. Sakhaii, W. Bermel, and K. Zangger, *Monitoring fast reactions by spatially-selective and frequency-shifted continuous NMR spectroscopy: application to rapid-injection protein unfolding.* Chem Commun (Camb), 2013. **49**(30): p. 3155-7.
264. Mitrev, Y., S. Simova, and D. Jeannerat, *NMR analysis of weak molecular interactions using slice-selective experiments via study of concentration gradients in agar gels.* Chem Commun (Camb), 2016. **52**(31): p. 5418-20.
265. Stoner, K.L., H. Harder, L.J. Fallowfield, and V.A. Jenkins, *Intravenous versus Subcutaneous Drug Administration. Which Do Patients Prefer? A Systematic Review.* Patient, 2014. **8**(2): p. 145-153.
266. Scherer, T., W. Lilyestrom, S. Yadav, and S.J. Shire, *Monoclonal Antibody Self-Association, Cluster Formation, and Rheology at High Concentrations.* Biophysical Journal, 2014. **106**(2): p. 58a-58a.
267. Joubert, M.K., Q. Luo, Y. Nashed-Samuel, J. Wypych, and L.O. Narhi, *Classification and characterization of therapeutic antibody aggregates.* J Biol Chem, 2011. **286**(28): p. 25118-33.
268. Cohen, S.L., C. Price, and J. Vlasak, *Beta-elimination and peptide bond hydrolysis: two distinct mechanisms of human IgG1 hinge fragmentation upon storage.* J Am Chem Soc, 2007. **129**(22): p. 6976-7.
269. Bye, J.W., L. Platts, and R.J. Falconer, *Biopharmaceutical liquid formulation: a review of the science of protein stability and solubility in aqueous environments.* Biotechnol Lett, 2014. **36**(5): p. 869-75.
270. Shire, S.J., *Formulation and manufacturability of biologics.* Curr Opin Biotechnol, 2009. **20**(6): p. 708-14.
271. Wu, Y., J. Levons, A.S. Narang, K. Raghavan, and V.M. Rao, *Reactive impurities in excipients: profiling, identification and mitigation of drug-excipient incompatibility.* AAPS PharmSciTech, 2011. **12**(4): p. 1248-63.
272. Martos, A., W. Koch, W. Jiskoot, K. Wuchner, G. Winter, W. Friess, and A. Hawe, *Trends on Analytical Characterization of Polysorbates and Their Degradation Products in Biopharmaceutical Formulations.* J Pharm Sci, 2017. **106**(7): p. 1722-1735.
273. Berkowitz, S.A., J.R. Engen, J.R. Mazzeo, and G.B. Jones, *Analytical tools for characterizing biopharmaceuticals and the implications for biosimilars.* Nat Rev Drug Discov, 2012. **11**(7): p. 527-40.
274. Thiagarajan, G., A. Semple, J.K. James, J.K. Cheung, and M. Shameem, *A comparison of biophysical characterization techniques in predicting monoclonal antibody stability.* MAbs, 2016. **8**(6): p. 1088-97.

275. Keire, D.A., *Analytical Tools for Physicochemical Characterization and Fingerprinting*, in *The Science and Regulations of Naturally Derived Complex Drugs*, R. Sasisekharan, et al., Editors. 2019, Springer International Publishing: Cham. p. 91-113.
276. Falk, B.T., Y. Liang, M. Bailly, F. Raoufi, A. Kekec, D. Pissarnitski, D. Feng, L. Yan, S. Lin, L. Fayadat-Dilman, and M.A. McCoy, *NMR Assessment of Therapeutic Peptides and Proteins: Correlations That Reveal Interactions and Motions.* Chembiochem, 2020. **21**(3): p. 315-319.
277. Arbogast, L.W., R.G. Brinson, and J.P. Marino, *Application of Natural Isotopic Abundance 1H–13C- and 1H–15N-Correlated Two-Dimensional NMR for Evaluation of the Structure of Protein Therapeutics*, in *Methods in Enzymology*. 2015, Academic Press.
278. Brinson, R.G., J.P. Marino, F. Delaglio, L.W. Arbogast, R.M. Evans, A. Kearsley, G. Gingras, H. Ghasriani, Y. Aubin, G.K. Pierens, X. Jia, M. Mobli, H.G. Grant, D.W. Keizer, K. Schweimer, J. Stahle, G. Widmalm, E.R. Zartler, C.W. Lawrence, P.N. Reardon, J.R. Cort, P. Xu, F. Ni, S. Yanaka, K. Kato, S.R. Parnham, D. Tsao, A. Blomgren, T. Rundlof, N. Trieloff, P. Schmieder, A. Ross, K. Skidmore, K. Chen, D. Keire, D.I. Freedberg, T. Suter-Stahel, G. Wider, G. Ilc, J. Plavec, S.A. Bradley, D.M. Baldisseri, M.L. Sforca, A.C.M. Zeri, J.Y. Wei, C.M. Szabo, C.A. Amezcua, J.B. Jordan, and M. Wikstrom, *Enabling adoption of 2D-NMR for the higher order structure assessment of monoclonal antibody therapeutics.* MAbs, 2019. **11**(1): p. 94-105.
279. Poppe, L., N. Knutson, S. Cao, and M. Wikstrom, *In Situ Quantification of Polysorbate in Pharmaceutical Samples of Therapeutic Proteins by Hydrodynamic Profiling by NMR Spectroscopy.* Anal Chem, 2019. **91**(12): p. 7807-7811.
280. Briggs, K.T., M.B. Taraban, and Y.B. Yu, *Water proton NMR detection of amide hydrolysis and diglycine dimerization.* Chem Commun (Camb), 2018. **54**(51): p. 7003-7006.
281. Taraban, M.B., R.A. DePaz, B. Lobo, and Y.B. Yu, *Water Proton NMR: A Tool for Protein Aggregation Characterization.* Anal Chem, 2017. **89**(10): p. 5494-5502.
282. Edwards, J.M., J.E. Bramham, A. Podmore, S.M. Bishop, C.F. van der Walle, and A.P. Golovanov, *(19)F Dark-State Exchange Saturation Transfer NMR Reveals Reversible Formation of Protein-Specific Large Clusters in High-Concentration Protein Mixtures.* Anal Chem, 2019. **91**(7): p. 4702-4708.
283. Liu, G., X. Wu, G. Jia, X. Chen, H. Zhao, J. Wang, C. Wu, and J. Cai, *Arginine: New Insights into Growth Performance and Urinary Metabolomic Profiles of Rats.* Molecules, 2016. **21**(9).
284. Sachs, D.H., A.N. Schechter, and J.S. Cohen, *Nuclear magnetic resonance titration curves of histidine ring protons. I. Influence of neighboring charged groups.* J Biol Chem, 1971. **246**(21): p. 6576-80.
285. Taraban, M.B., H.C. Truong, Y. Feng, E.V. Jouravleva, M.A. Anisimov, and Y.B. Yu, *Water Proton NMR for In Situ Detection of Insulin Aggregates.* J Pharm Sci, 2015. **104**(12): p. 4132-4141.
286. Peng, J., S.M. Patil, D.A. Keire, and K. Chen, *Chemical Structure and Composition of Major Glycans Covalently Linked to Therapeutic Monoclonal Antibodies by Middle-Down Nuclear Magnetic Resonance.* Anal Chem, 2018. **90**(18): p. 11016-11024.

287. Lam, X.M., J.Y. Yang, and J.L. Cleland, *Antioxidants for prevention of methionine oxidation in recombinant monoclonal antibody HER2.* J Pharm Sci, 1997. **86**(11): p. 1250-5.

288. Wei, B., K. Berning, C. Quan, and Y.T. Zhang, *Glycation of antibodies: Modification, methods and potential effects on biological functions.* MAbs, 2017. **9**(4): p. 586-594.

289. Shire, S.J., Z. Shahrokh, and J. Liu, *Challenges in the Development of High Protein Concentration Formulations*, in *Current Trends in Monoclonal Antibody Development and Manufacturing*, S.J. Shire, et al., Editors. 2010, Springer New York: New York, NY. p. 131-147.

290. Arakawa, T., D. Ejima, and T. Akuta, *Protein aggregation under high concentration/density state during chromatographic and ultrafiltration processes.* Int J Biol Macromol, 2017. **95**: p. 1153-1158.

291. Cao, W., S. Krishnan, M.S. Ricci, L.Y. Shih, D. Liu, J.H. Gu, and F. Jameel, *Rational design of lyophilized high concentration protein formulations-mitigating the challenge of slow reconstitution with multidisciplinary strategies.* Eur J Pharm Biopharm, 2013. **85**(2): p. 287-93.

292. Bhatnagar, B.S., R.H. Bogner, and M.J. Pikal, *Protein stability during freezing: separation of stresses and mechanisms of protein stabilization.* Pharm Dev Technol, 2007. **12**(5): p. 505-23.

293. Johnson, H.R. and A.M. Lenhoff, *Characterization and suitability of therapeutic antibody dense phases for subcutaneous delivery.* Mol Pharm, 2013. **10**(10): p. 3582-91.

294. Asenjo, J.A. and B.A. Andrews, *Aqueous two-phase systems for protein separation: a perspective.* J Chromatogr A, 2011. **1218**(49): p. 8826-35.

295. Mao, L.N., J.K. Rogers, M. Westoby, L. Conley, and J. Pieracci, *Downstream antibody purification using aqueous two-phase extraction.* Biotechnol Prog, 2010. **26**(6): p. 1662-70.

296. Schmidt, A., M. Richter, F. Rudolph, and J. Strube, *Integration of Aqueous Two-Phase Extraction as Cell Harvest and Capture Operation in the Manufacturing Process of Monoclonal Antibodies.* Antibodies (Basel), 2017. **6**(4): p. 21.

297. Wang, Z., G. Zhang, and H. Zhang, *Protocol for analyzing protein liquid–liquid phase separation.* Biophysics Reports, 2018. **5**(1): p. 1-9.

298. He, F., C.E. Woods, E. Trilisky, K.M. Bower, J.R. Litowski, B.A. Kerwin, G.W. Becker, L.O. Narhi, and V.I. Razinkov, *Screening of monoclonal antibody formulations based on high-throughput thermostability and viscosity measurements: design of experiment and statistical analysis.* J Pharm Sci, 2011. **100**(4): p. 1330-40.

299. Inoue, N., E. Takai, T. Arakawa, and K. Shiraki, *Specific decrease in solution viscosity of antibodies by arginine for therapeutic formulations.* Mol Pharm, 2014. **11**(6): p. 1889-96.

300. Bramham, J.E., A. Podmore, S.A. Davies, and A.P. Golovanov, *Comprehensive Assessment of Protein and Excipient Stability in Biopharmaceutical Formulations Using 1H NMR Spectroscopy.* ACS Pharmacology & Translational Science, 2020. **4**(1): p. 288-295.

301. Kuznetsova, I.M., K.K. Turoverov, and V.N. Uversky, *What macromolecular crowding can do to a protein.* Int J Mol Sci, 2014. **15**(12): p. 23090-140.

302. Theillet, F.X., A. Binolfi, T. Frembgen-Kesner, K. Hingorani, M. Sarkar, C. Kyne, C. Li, P.B. Crowley, L. Gierasch, G.J. Pielak, A.H. Elcock, A. Gershenson,

and P. Selenko, *Physicochemical properties of cells and their effects on intrinsically disordered proteins (IDPs).* Chem Rev, 2014. **114**(13): p. 6661-714.

303. Ecker, D.M., S.D. Jones, and H.L. Levine, *The therapeutic monoclonal antibody market.* MAbs, 2015. **7**(1): p. 9-14.
304. Elvin, J.G., R.G. Couston, and C.F. van der Walle, *Therapeutic antibodies: market considerations, disease targets and bioprocessing.* Int J Pharm, 2013. **440**(1): p. 83-98.
305. Shpilberg, O. and C. Jackisch, *Subcutaneous administration of rituximab (MabThera) and trastuzumab (Herceptin) using hyaluronidase.* Br J Cancer, 2013. **109**(6): p. 1556-61.
306. Turner, M.R. and S.V. Balu-Iyer, *Challenges and Opportunities for the Subcutaneous Delivery of Therapeutic Proteins.* J Pharm Sci, 2018. **107**(5): p. 1247-1260.
307. Robak, T., *The emerging therapeutic role of antibody mixtures.* Expert Opin Biol Ther, 2013. **13**(7): p. 953-8.
308. Rasmussen, S.K., H. Naested, C. Muller, A.B. Tolstrup, and T.P. Frandsen, *Recombinant antibody mixtures: production strategies and cost considerations.* Arch Biochem Biophys, 2012. **526**(2): p. 139-45.
309. Rao, G., V. Iyer, M.P. Kosloski, D.S. Pisal, E. Shin, C.R. Middaugh, and S.V. Balu-Iyer, *Use of a folding model and in situ spectroscopic techniques for rational formulation development and stability testing of monoclonal antibody therapeutics.* J Pharm Sci, 2010. **99**(4): p. 1697-706.
310. Wuchner, K., J. Buchler, R. Spycher, P. Dalmonte, and D.B. Volkin, *Development of a microflow digital imaging assay to characterize protein particulates during storage of a high concentration IgG1 monoclonal antibody formulation.* J Pharm Sci, 2010. **99**(8): p. 3343-61.
311. Fischer, K. and M. Schmidt, *Pitfalls and novel applications of particle sizing by dynamic light scattering.* Biomaterials, 2016. **98**: p. 79-91.
312. Mehta, V.D., P.V. Kulkarni, R.P. Mason, A. Constantinescu, and P.P. Antich, *Fluorinated proteins as potential 19F magnetic resonance imaging and spectroscopy agents.* Bioconjug Chem, 1994. **5**(3): p. 257-61.
313. Anthis, N.J. and G.M. Clore, *Visualizing transient dark states by NMR spectroscopy.* Q Rev Biophys, 2015. **48**(1): p. 35-116.
314. Ding, Y.H., S.B. Fan, S. Li, B.Y. Feng, N. Gao, K. Ye, S.M. He, and M.Q. Dong, *Increasing the Depth of Mass-Spectrometry-Based Structural Analysis of Protein Complexes through the Use of Multiple Cross-Linkers.* Anal Chem, 2016. **88**(8): p. 4461-9.
315. Ranganathan, A., S.J. Gee, and B.D. Hammock, *An immunoassay for the detection of triclosan-O-glucuronide, a primary human urinary metabolite of triclosan.* Anal Bioanal Chem, 2015. **407**(24): p. 7263-73.
316. Aguilar, J.A., M. Nilsson, G. Bodenhausen, and G.A. Morris, *Spin echo NMR spectra without J modulation.* Chem Commun (Camb), 2012. **48**(6): p. 811-3.
317. Korson, L., W. Drost-Hansen, and F.J. Millero, *Viscosity of water at various temperatures.* The Journal of Physical Chemistry, 1969. **73**(1): p. 34-39.
318. Medina-Noyola, M., *Long-time self-diffusion in concentrated colloidal dispersions.* Phys Rev Lett, 1988. **60**(26): p. 2705-2708.
319. van Blaaderen, A., J. Peetermans, G. Maret, and J.K.G. Dhont, *Long-time self-diffusion of spherical colloidal particles measured with fluorescence recovery after photobleaching.* The Journal of Chemical Physics, 1992. **96**(6): p. 4591-4603.

320. Andersson, K.M. and S. Hovmöller, *The average atomic volume and density of proteins.* Zeitschrift für Kristallographie - Crystalline Materials, 1998. **213**(7-8): p. 369-373.
321. Barnett, G.V., V.I. Razinkov, B.A. Kerwin, T.M. Laue, A.H. Woodka, P.D. Butler, T. Perevozchikova, and C.J. Roberts, *Specific-ion effects on the aggregation mechanisms and protein-protein interactions for anti-streptavidin immunoglobulin gamma-1.* J Phys Chem B, 2015. **119**(18): p. 5793-804.
322. Raut, A.S. and D.S. Kalonia, *Opalescence in monoclonal antibody solutions and its correlation with intermolecular interactions in dilute and concentrated solutions.* J Pharm Sci, 2015. **104**(4): p. 1263-74.
323. Mitrea, D.M. and R.W. Kriwacki, *Phase separation in biology; functional organization of a higher order.* Cell Commun Signal, 2016. **14**(1): p. 1.
324. Feric, M., N. Vaidya, T.S. Harmon, D.M. Mitrea, L. Zhu, T.M. Richardson, R.W. Kriwacki, R.V. Pappu, and C.P. Brangwynne, *Coexisting Liquid Phases Underlie Nucleolar Subcompartments.* Cell, 2016. **165**(7): p. 1686-1697.
325. Wegmann, S., B. Eftekharzadeh, K. Tepper, K.M. Zoltowska, R.E. Bennett, S. Dujardin, P.R. Laskowski, D. MacKenzie, T. Kamath, C. Commins, C. Vanderburg, A.D. Roe, Z. Fan, A.M. Molliex, A. Hernandez-Vega, D. Muller, A.A. Hyman, E. Mandelkow, J.P. Taylor, and B.T. Hyman, *Tau protein liquid-liquid phase separation can initiate tau aggregation.* EMBO J, 2018. **37**(7): p. e98049.
326. Ambadipudi, S., J. Biernat, D. Riedel, E. Mandelkow, and M. Zweckstetter, *Liquid-liquid phase separation of the microtubule-binding repeats of the Alzheimer-related protein Tau.* Nat Commun, 2017. **8**(1): p. 275.
327. Galkin, O. and P.G. Vekilov, *Control of protein crystal nucleation around the metastable liquid-liquid phase boundary.* Proc Natl Acad Sci U S A, 2000. **97**(12): p. 6277-81.
328. Teixeira, A.G., R. Agarwal, K.R. Ko, J. Grant-Burt, B.M. Leung, and J.P. Frampton, *Emerging Biotechnology Applications of Aqueous Two-Phase Systems.* Adv Healthc Mater, 2018. **7**(6): p. e1701036.
329. Ruff, K.M., S. Roberts, A. Chilkoti, and R.V. Pappu, *Advances in Understanding Stimulus-Responsive Phase Behavior of Intrinsically Disordered Protein Polymers.* J Mol Biol, 2018. **430**(23): p. 4619-4635.
330. Boyko, S., X. Qi, T.H. Chen, K. Surewicz, and W.K. Surewicz, *Liquid-liquid phase separation of tau protein: The crucial role of electrostatic interactions.* J Biol Chem, 2019. **294**(29): p. 11054-11059.
331. Yuwen, T., A. Bah, J.P. Brady, F. Ferrage, G. Bouvignies, and L.E. Kay, *Measuring Solvent Hydrogen Exchange Rates by Multifrequency Excitation (15)N CEST: Application to Protein Phase Separation.* J Phys Chem B, 2018. **122**(49): p. 11206-11217.
332. Damman, R., S. Schutz, Y. Luo, M. Weingarth, R. Sprangers, and M. Baldus, *Atomic-level insight into mRNA processing bodies by combining solid and solution-state NMR spectroscopy.* Nat Commun, 2019. **10**(1): p. 4536.
333. Ambadipudi, S., J.G. Reddy, J. Biernat, E. Mandelkow, and M. Zweckstetter, *Residue-specific identification of phase separation hot spots of Alzheimer's-related protein tau.* Chem Sci, 2019. **10**(26): p. 6503-6507.
334. Bax, A. and R. Freeman, *Enhanced NMR resolution by restricting the effective sample volume.* Journal of Magnetic Resonance (1969), 1980. **37**(1): p. 177-181.

335. Lee, J.C. and S.N. Timasheff, *Partial specific volumes and interactions with solvent components of proteins in guanidine hydrochloride.* Biochemistry, 1974. **13**(2): p. 257-65.

336. Xu, Z., C. Liu, S. Zhao, S. Chen, and Y. Zhao, *Molecular Sensors for NMR-Based Detection.* Chem Rev, 2019. **119**(1): p. 195-230.

337. Fuentes-Monteverde, J.C., S. Becker, and N. Rezaei-Ghaleh, *Biomolecular phase separation through the lens of sodium-23 NMR.* Protein Sci, 2020. **1**(11).

338. Wallace, M., J.A. Iggo, and D.J. Adams, *Using solution state NMR spectroscopy to probe NMR invisible gelators.* Soft Matter, 2015. **11**(39): p. 7739-47.

339. Buck, M., *Trifluoroethanol and colleagues: cosolvents come of age. Recent studies with peptides and proteins.* Q Rev Biophys, 1998. **31**(3): p. 297-355.

340. Carrotta, R., M. Manno, F.M. Giordano, A. Longo, G. Portale, V. Martorana, and P.L. Biagio, *Protein stability modulated by a conformational effector: effects of trifluoroethanol on bovine serum albumin.* Phys Chem Chem Phys, 2009. **11**(20): p. 4007-18.

341. Henderson, T.J., *Quantitative NMR spectroscopy using coaxial inserts containing a reference standard: purity determinations for military nerve agents.* Anal Chem, 2002. **74**(1): p. 191-8.

342. Bucciarelli, S., N. Mahmoudi, L. Casal-Dujat, M. Jehannin, C. Jud, and A. Stradner, *Extended Law of Corresponding States Applied to Solvent Isotope Effect on a Globular Protein.* J Phys Chem Lett, 2016. **7**(9): p. 1610-5.

343. Allen, J. and K. Damodaran, *High-resolution slice selection NMR for the measurement of CO2 diffusion under non-equilibrium conditions.* Magn Reson Chem, 2015. **53**(3): p. 200-2.

344. Wallace, M., D.J. Adams, and J.A. Iggo, *Titrations without the Additions: The Efficient Determination of p Ka Values Using NMR Imaging Techniques.* Anal Chem, 2018. **90**(6): p. 4160-4166.

345. Mantel, C., P.A. Bayle, S. Hediger, C. Berthon, and M. Bardet, *Study of liquid-liquid interfaces by an easily implemented localized NMR sequence.* Magn Reson Chem, 2010. **48**(8): p. 600-6.

346. Lambert, J., R. Hergenroder, D. Suter, and V. Deckert, *Probing liquid-liquid interfaces with spatially resolved NMR spectroscopy.* Angew Chem Int Ed Engl, 2009. **48**(34): p. 6343-5.

347. Nose, T., *Kinetics of phase separation in polymer mixtures.* Phase Transitions, 1987. **8**(3): p. 245-260.

348. Cardinaux, F., E. Zaccarelli, A. Stradner, S. Bucciarelli, B. Farago, S.U. Egelhaaf, F. Sciortino, and P. Schurtenberger, *Cluster-driven dynamical arrest in concentrated lysozyme solutions.* J Phys Chem B, 2011. **115**(22): p. 7227-37.

349. Alberti, S., A. Gladfelter, and T. Mittag, *Considerations and Challenges in Studying Liquid-Liquid Phase Separation and Biomolecular Condensates.* Cell, 2019. **176**(3): p. 419-434.

350. Aguzzi, A. and M. Altmeyer, *Phase Separation: Linking Cellular Compartmentalization to Disease.* Trends Cell Biol, 2016. **26**(7): p. 547-558.

351. Qi, W., L. Alekseychyk, N. Nuanmanee, D.B. Temel, V. Jann, M. Treuheit, and V. Razinkov, *Resolving Liquid-Liquid Phase Separation for a Peptide Fused Monoclonal Antibody by Formulation Optimization.* J Pharm Sci, 2021. **110**(2): p. 738-745.

352. Geoghegan, J.C., R. Fleming, M. Damschroder, S.M. Bishop, H.A. Sathish, and R. Esfandiary, *Mitigation of reversible self-association and viscosity in a human*

IgG1 monoclonal antibody by rational, structure-guided Fv engineering. MAbs, 2016. **8**(5): p. 941-50.

353. Ebrahimi, P., M. Nilsson, G.A. Morris, H.M. Jensen, and S.B. Engelsen, *Cleaning up NMR spectra with reference deconvolution for improving multivariate analysis of complex mixture spectra.* Journal of Chemometrics, 2014. **28**(8): p. 656-662.

354. Rogers, B.A., K.B. Rembert, M.F. Poyton, H.I. Okur, A.R. Kale, T. Yang, J. Zhang, and P.S. Cremer, *A stepwise mechanism for aqueous two-phase system formation in concentrated antibody solutions.* Proc Natl Acad Sci U S A, 2019. **116**(32): p. 15784-15791.